University of Southampton

Faculty of Engineering and Physical Sciences

DEVELOPMENT OF A 3D FINITE ELEMENT MODEL FOR QUASI-STATIC INDENTATION OF A TYPE III PRESSURE VESSEL

Erick Montes de Oca Valle

A thesis submitted for the degree of

Doctor of Engineering

November 2020

University of Southampton

ABSTRACT

Faculty of Engineering and Physical Sciences

Thesis for the degree of Doctor of Engineering

Development of a 3D finite element model for quasi-static indentation of a Type III pressure vessel

by Erick Montes de Oca Valle

Type III cylinders are hybrid structures typically consisting of a metal liner enclosed by layers of composite material. Such structures are prone to unexpected damage during service, usually as a result of a low velocity impact. The capability of the cylinder to carry load in the presence of existing damage due to an impact event has not been fully investigated for these structures. In this project, a methodology to develop a novel 3D finite element model of a Type III cylinder under quasi-static indentation loading is presented. The aim is to investigate the structure's damage tolerance properties by predicting the residual indentation developed in the inner metal liner of the cylinder due to quasi-static load application. Previous work had indicated that this is the critical determinant of the post-indent residual fatigue life.

The project is divided into three parts. First a ring specimen investigation, consisting of a short cylindrical cross section of a complete cylinder was virtually and experimentally analysed under a 2D line quasi-static compression indentation. The structure is an intermediate building block to allow improved understanding of Type III cylinders, and to allow the modelling approach to be refined on a specimen with less complexity than a full cylinder. Using this model it was possible to predict composite damage delamination as well as metal-composite separation using an explicit finite element model containing cohesive elements. Metal-composite interface properties were obtained and calibrated through experimental testing. Validation was performed by comparing force-displacement curves, strain field measurements, and chronological visualisation of damage events. Analytical results showed good agreement with experimental values.

Then, the interface properties obtained from the ring specimen model were transferred to a full Type III cylinder model. The model was compared with experimental results from a previous study on complete cylinders and was found to predict the quasi-static indentation response well, without further calibration or fitting of the metal-composite interface properties. It was demonstrated that the methodology developed was applicable for developing Type III cylinder models with different diameter sizes and thickness ratios.

Finally, the model was used for parametric investigations in which the residual dent was evaluated under different geometric and loading conditions, including internal pressure loads. Overall, it was demonstrated that relevant damage processes associated with quasi-static indentation are reproduced. Furthermore, it was shown this model can be used to explore different design options in a virtual environment and could potentially be used in early stages of the cylinder product design cycle.

Contents

List of Figures

List of Tables

Declaration of Authorship

I, Erick Montes de Oca Valle, declare that this thesis entitled *"Development of a 3D Finite Element model for a quasi-static indentation of a Type III pressure vessel"* and the work presented in it are my own and has been generated by me as the result of my own original research.

I confirm that:

1. This work was made wholly or mainly while in the candidature for a research degree at this University;
2. Where any part of this thesis has previously been submitted for a degree or any other qualification at this University or any other institution, this has been clearly stated;
3. Where I have quoted for the work of others, the source is always given. With exceptions of such quotations, this thesis is entirely my own work;
4. I have acknowledged all main sources of help;
5. Where the thesis is based on work done by myself jointly with others, I have made clear exactly what was done by others and what I have contributed myself;
6. Part of this work have been published as detailed in the list of publications provided in this manuscript

Signed

Date: 17/11/2020

Acknowledgements

I want to acknowledge my supervisors, Professor Ian Sinclair and Professor S. Mark Spearing for their amazing support during the development of my EngD. I was lucky to have a great team of supervisors which made things easier whenever I needed and that encouraged me to keep going at every moment.
I would also like to thank Luxfer Gas Cylinders, specially Dr. Warren Hepples for the support provided throughout the development of the project, during meetings, revisions and sharing knowledge and experience to contribute to the project.
For the numerous group meetings and the great conversations and moments inside the University and/or while travelling I would like to thank Dr. Mark Mavrogordato, Dr. Sebastian Rosini, Erich Schöberl and Kieran Ball.
I want to thank the National Council for Science and Technology (CONACYT) for the financial support provided during the last four years, which made possible the achievement of this personal project.
I want to thank my friends, Berenice, Barbara, Daniela, Isaac, Ezequiel, Ana, Paty, Steph, Rafa, Joel and Mariana for being always in contact and encouraging me. Special thanks to Taine Ramirez, for her great welfare support and guidance, which has been a very important part.
I want to thank my family, particularly, Edna and Roberto. Mom & Dad: this personal project never would have started without your support. Despite the distance, it felt that you were here next to me at every single moment. Gracias.
Finally, I want to thank the love of my life, Monse. This has been the single greatest adventure of my life, and the best part has been sharing it with you. Thanks for being caring, supportive, understanding and patient, specially the last few months. I am very lucky that you have been with me throughout this whole adventure. Infinite thanks for being there always!

To Paco and Abuelito Roberto...

Acronyms

AFV Alternative Fuel Vehicles
ARALL Aramid Reinforced Aluminium Laminates

BVID Barely Visible Impact Damage

CARALL Carbon Reinforced Aluminium Laminates
CBT Classical Beam Theory
CFRP Carbon Fibre Reinforced Polymer
COPV Composite Overwrapped Pressure Vessels
CT Computer Tomography
CZM Cohesive Zone Model

DCB Double Cantilever Beam
DIC Digital Image Correlation
DoT Department of Transport

ENF End Notched Flexure

FE Finite Element
FML Fibre Metal Laminates
FoV Field of View

GFRP Glass Fibre Reinforced Polymer
GLARE Glass Rinforced Aluminium Laminates

IE Internal Energy

KE Kinetic Energy

LEFM Linear Elastic Fracture Mechanics

LGC Luxfer Gas Cylinders
LVI low velocity impact

MMB Mixed-Mode Bending

PMC Polymer Matrix Composites

SCBA self-contained breathing apparatus

VCCT Virtual Crack Closure Technique

Chapter 1

Introduction

1.1 Background

Since the 1940's applications using Polymer Matrix Composites (PMC) have been developed, initially mainly using glass fibres. Development of different PMC applications led engineers to observe that the density of Glass Fibre Reinforced Polymer (GFRP) is relatively high and their specific stiffness is low, thus new composite materials based on carbon fibres were developed [1]. The high stiffness and strength to weight ratio of Carbon Fibre Reinforced Polymer (CFRP) composites became very attractive initially for aircraft structural applications, and subsequently their use has expanded to other sectors.

Additional to high specific strength and stiffness PMCs offer the advantage of being *tailored* materials, i.e. they can be manufactured with mechanical properties specific to a certain problem. As a result, these materials are widely used in automotive, aerospace and marine industries which typically aim for weight saving in their products [1–3]. For instance, civil airframes increasingly contain significant amounts of carbon fibre composites in their construction ($\sim 50\%$ by weight) and many luxury and performance cars include carbon fibre composite components to substitute for metals. Consequently, by developing such complex structures, these industries have become the significant drivers of research related to PMCs [4].

Regarding product design, transport applications are frequently weight-reduction driven so the use of composites conveys an obvious advantage, however

there are other sectors interested in applying and developing research related to PMCs. One example is the pressure vessel industry. Initially, pure metallic pressure vessels were commonly used to contain and transport gases with working pressures up to 12 MPa. However, the pressure requirements have kept increasing due to the variety of applications and standards set by industry. Currently, such applications may require up to 10,000 l cylinder capacity and working pressures range from 20 to 70 MPa which depends on the application [5]. Such requirements can be reached by hybrid metal-composite pressure vessels, used to store hydrogen or natural gas for Alternative Fuel Vehicles (AFV). Cylinders using similar materials but smaller sizes are used in other sectors. For instance, the healthcare sector uses portable oxygen cylinders which are usually in the range of 1 to 10 l capacity [6], while the emergency services use slightly larger capacity cylinders for self-contained breathing apparatus (SCBA). As such, transport, emergency services and healthcare sectors are growing based on environmental and health standards, therefore it is expected that the production demand for a wide range of pressure vessels will continue to grow in the next few years [7].

According to the material combinations used for construction, four categories of pressure vessels have been defined: Type I, Type II, Type III and Type IV cylinders [8]. A short description of the cylinders is presented in Table 1.1. Type III and Type IV cylinders are very attractive options for automotive and transport industries because of several advantages over Type I and II cylinders. These advantages include a large overall weight reduction, increased load-carrying capacity and improved corrosion resistance. As a consequence of the use of Type III and IV cylinders in transport applications, these components are required to meet the same crash-worthiness regulations as the vehicle as a whole; this has hitherto been achieved largely by empirical approaches.

Previous research conducted at the University of Southampton studied the failure mechanisms of Type III cylinders. This initially focused on understanding and improving static burst pressure, which is one key design driver, however other factors are known to be important for cylinder development. The work of Allen [2] showed that post impact damage has an important effect on the cylinder's fatigue life. Damage to Type III cylinders can result from pressure loads or dynamic loads, such as low velocity impact (LVI) resulting from the

Table 1.1: Pressure vessel classification according to material

Type	Description
I	Pure metal (steel or aluminium)
II	Metal cylinders with composite hoop-wrapped barrel
III	Metal liner fully wrapped with multi-axial composite filaments
IV	Plastic liner fully wrapped with composite filaments

cylinder being dropped during transportation or during vehicle accidents [5]. It was observed that, as a result of LVI, permanent damage may not only occur in the composite layers of the cylinders, but also in the aluminium liner as well. Figure 1.1 shows the residual indentation developed in the liner as a consequence of a LVI. As reported by Allen [2] the depth of this *blister-like* deformation has a direct relation to the subsequent fatigue life performance of the cylinder, i.e. the deeper the indentation depth the greater the reduction in the fatigue life.

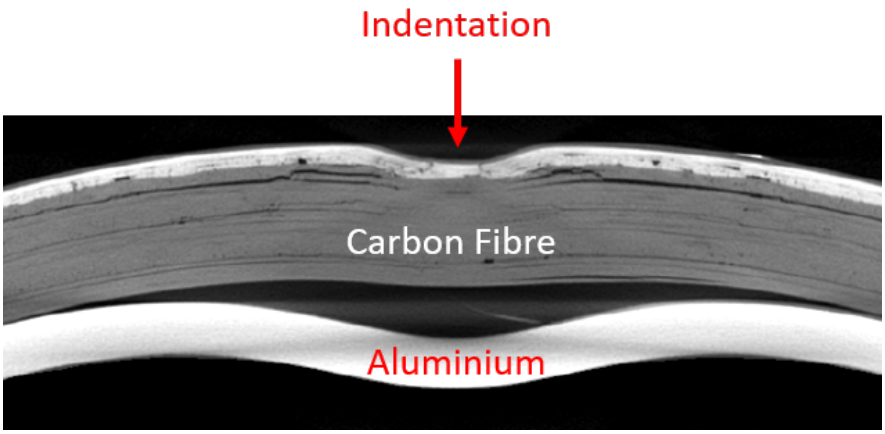

Figure 1.1: CT image of the blister formation within a Type III cylinder after a quasi-static indentation test similar to a LVI [2]

Although current designs are still nominally driven by burst pressure failure, Type III cylinders must satisfy different standards which contain post-impact behaviour tests. ISO 11119-2 and DoT CFFC:2007 [9, 10] are two different standards which include free fall cylinder drop tests followed by post-impact pressure and fatigue tests. Considering that the current standards include guidelines to test the post-impact behaviour of Type III cylinders, research is needed to develop more robust designs that can withstand higher loads in the presence of damage. Particular methods need to be developed for the design of cylinders accounting for both burst pressure and post-impact fatigue performance. This is a particular example of a more general requirement for structural designs in which initial static load requirements must be balanced against requirements for damage resistance and damage tolerance.

To achieve a robust design with a balanced burst pressure and post impact performance target, a deeper understanding of the mechanical properties governing the metal-composite interface within Type III cylinders should be developed. Furthermore, the understanding of these characteristics can be used to modify the design in order to increase its capabilities. While this could continue to be achieved by largely empirical means, it is highly desirable to develop a better predictive modelling capability in order to reduce the cost of developing new cylinder designs. This is particularly important for large cylinders where the manufacturing cost is high.

The novelty of the current project relies on the use of Finite Element (FE) analysis to predict the residual indentation developed on the metal liner of a Type III cylinder in order to gain understanding of its development during a LVI. Although this indentation has been previously reported [5], no further research has been performed to investigate the development of this dent using numerical modelling techniques. Furthermore, the model developed in this project is used to investigate the properties governing the metal-composite interface such as the interface fracture toughness and strength, which have not been reported in literature hitherto. Parameters obtained from model characterisation will be used for basic optimisation, to find design criteria that contribute to a reduction of the liner residual dent at impact sites. Experimental testing for validation activities are implemented to verify the model outputs. Finally, design modifications will

be proposed to explore the potential of the cylinder model for use as part of the design process and investigate the dent development under different loading and boundary conditions. Particular focus will be given to the role of design choices in determining the dent development, and therefore likely post-impact fatigue life, under different loading conditions.

1.2 Project Sponsor

The current project was developed as part of an Engineering Doctorate programme, which requires an industrial collaboration so that the outcomes have significant contributions to both academic and the industrial sides. This project is sponsored by Luxfer Gas Cylinders (LGC), which is one of the world's largest manufacturers of metal and composite cylinders having regional offices worldwide including U.S., England, Canada, China and India. Research collaboration between LGC and University of Southampton seeks to contribute not only to engineering product understanding and enhancement but also regarding the product standards for the cylinder market.

1.3 Project aim and objectives

The aim of this research is to develop a 3D FE model of a Type III cylinder to predict the separation and residual indentation depth occurring at the metal-composite interface as a result of a quasi-static indentation, which has been shown to be a good proxy for impact [11]. Results are initially motivated and discussed against previous experimental findings, however, new experiments are proposed to gain greater mechanistic understanding of the damage process within the indentation region. These experiments include applying quasi-static 2D line indentations on hybrid metal-composite structures similar to Type III cylinders. Additionally, Digital Image Correlation (DIC) will be included to obtain 2D full field mapping of deformation and load partitioning between composite and metallic layers during LVI-like load events.

The aim of the project will be achieved through the following objectives:

- Develop a FE model based on testing a structure similar in construction

to a Type III cylinder, identified here as a ring specimen. The aim is to obtain more detailed insight regarding deformation and damage evolution in the indentation region, including damage to the composite layers. This specimen is simpler than a full cylinder and allows modelling complexities to be understood and addressed with lower computational cost than for a full cylinder.

- Conduct experiments on ring specimens extracted from full cylinders to allow model calibration and initial verification of the analogous FE model.
- Use the model and experimental tests to investigate the properties governing the metal-composite interface within a Type III cylinder.
- Develop a full 3D FE model using the properties investigated during the ring specimen activities. Use the model for parametric investigation of the cylinder behaviour.
- Transfer the knowledge obtained during the course of this Eng.D product to the industrial sponsor to help improve their design process and also to help inform industry-wide pressure vessel standards.

1.4 Thesis structure

The overall thesis structure is written as follows:

Chapter 2 - Literature review: This chapters presents details regarding design and manufacturing of Type III cylinders. Furthermore, a review of composite materials behaviour along with low velocity impacts is presented. Finally, an overview of finite element modelling techniques and relevant models previously developed is shown in this chapter.

Chapter 3 - Experimental background and modelling methods: This chapter briefly describes the some of the experiments and results that motivated some of the objectives of the current project. Furthermore, general methods used throughout this project are presented, such as experimental imaging and numerical modelling techniques.

Chapter 4 - Model experiment comparison for transverse loading of metal-composite Ring Specimen: This chapter presents the development of a ring specimen FE model along with an analogous experiment to validate such model. This chapter has been submitted to Composites: Part B journal as a paper. For this reason some sections described in the literature review are presented in this chapter as part of the introduction.

Chapter 5 - Full Type III cylinder cohesive element implementation: Modelling methodologies obtained from the previous chapter were implemented in a full Type III cylinder model which is presented in this chapter. This chapter has been submitted to Composites: Part B.

Chapter 6 - Parametric investigation of a Type III cylinder using a Finite Element approach: Parametric investigation to explore design possibilities for Type III cylinders was performed using the full cylinder model and is presented in this chapter. Among the design variables explored using the model are material and metal-composite interface modification. Furthermore, damage within the inner layers of the cylinder was analysed under pressure loads.

Chapter 7 - Conclusions & Future work: General conclusions of the present work are drawn regarding the validity and usage of the model presented. Additionally, suggestions are given from an academic and industrial point of view towards further work relating to the cylinder model.

1.5 List of Publications

1.5.1 Conference papers

- Montes de Oca, E., Spearing S.M., Sinclair, I., Hepples, W., *Development of a 3D finite element model of a quasi-static indentation test in a Type III cylinder*, proceedings for the SAMPE European Conference, Southampton, UK, 2018.

- Montes de Oca, E., Spearing S.M., Sinclair, I., Hepples, W., *Development of a 3D finite element model of a quasi-static indentation test in a Type III cylinder*, proceedings for the 22^{nd} International Conference of Composite Materials (ICCM), Melbourne, Australia, 2019.

1.5.2 Journal papers

- Montes de Oca, E., Spearing S.M., Sinclair, I., Hepples, W., *Model-experiment comparison for transverse loading of metal-composite Ring Specimen (Part 1)*, submitted to Composites: Part B.

- Montes de Oca, E., Spearing S.M., Sinclair, I., Hepples, W., *Full Type III cylinder cohesive element implementation (Part 2)*, submitted to Composites: Part B.

Chapter 2

Literature review

2.1 Type III cylinders manufacture

Typical construction of a Type III cylinder is described in Figure 2.1. The cylinder is a hybrid structure consisting of a metal liner which main objective is to avoid any gas leaking. The metal liner is wrapped by composite layers which carry the majority of the loading. A description of the manufacturing process of each part of the cylinder is describe in the next sections.

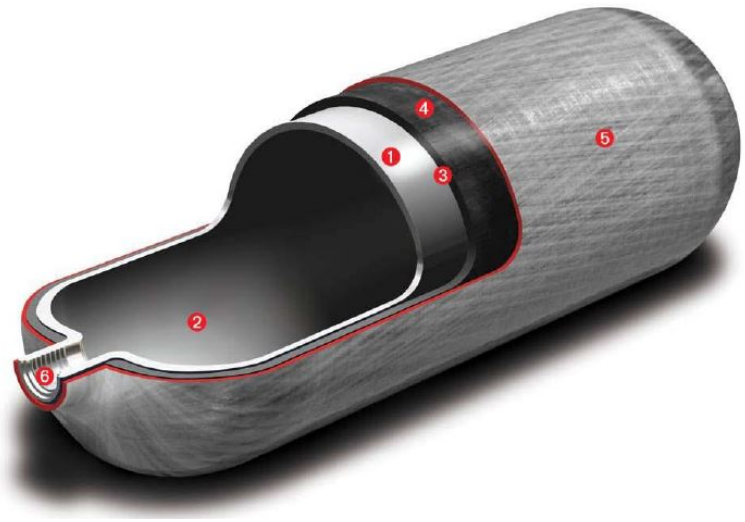

Figure 2.1: Typical Type III cylinder: 1. Aluminium liner; 2. Surface finish; 3. Insulating layer for metal-composite interface; 4. CFRP overwrap; 5. GFRP protective layer [12]

2.1.1 Aluminium liner

Typical manufacturing process of Type III cylinders, starts with the metal liner, often stainless steel, titanium or an aluminium alloy. The latter is one of the most common used in industry [13]. Manufacturing of this part is commonly performed by either deep draw and spinning or extruded tubing and spin closing. The process typically starts with a cylindrical die that is used to draw a circular metal plate, followed by a heat treatment to improve strength and durability of the resultant liner [6, 14]. The open part of the cylinder is then closed using metal spinning techniques. A further T6 heat treatment is applied to the final shaped cylinder, followed by inspections to ensure that the liner is ready for the wrapping process. A summary of the liner manufacture can be observed in Figure 2.2 [6, 15].

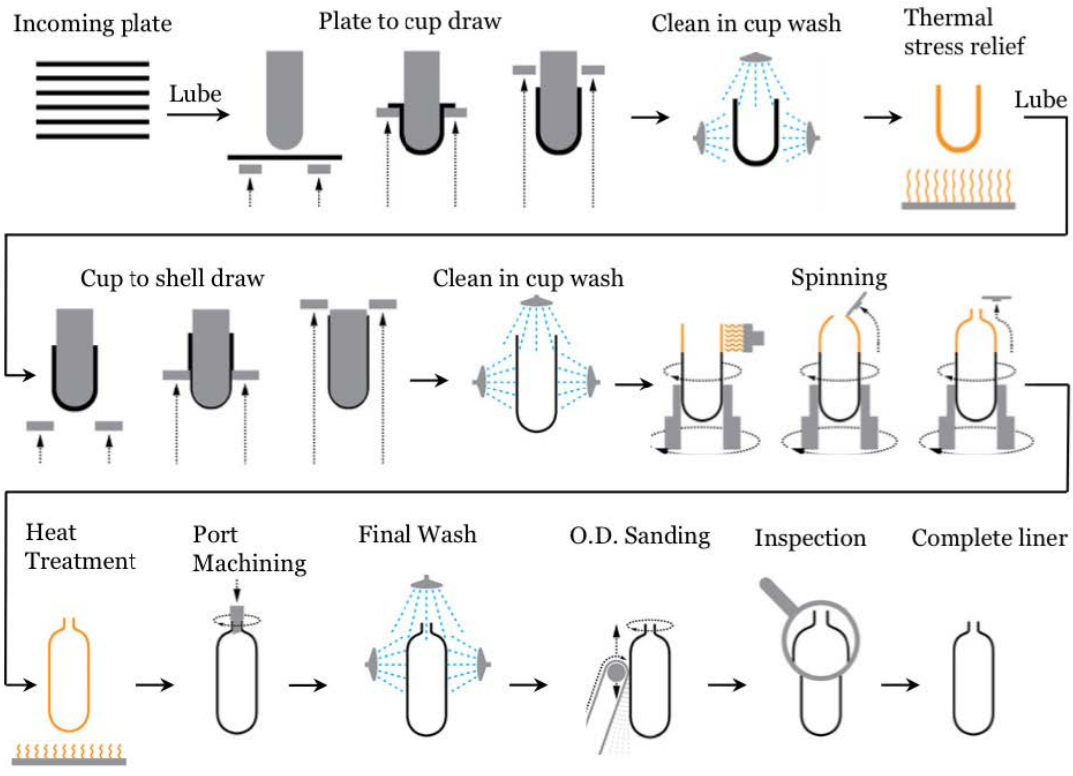

Figure 2.2: Type III cylinder aluminium liner manufacturing process [6]

2.1.2 Composite wrap

Composite reinforcement is typically manufactured by braiding, prepreg layup or filament winding. The latter is one of the most common techniques used for Type III cylinders because it is relatively simple to apply and control [5, 13, 15]. During this process fibre tows are impregnated with liquid resin and then used to wrap the cylinder which is rotating in a circular mandrel. Figure 2.3 shows a typical fibre winding process. In this step, the fibres are commonly applied in three different winding angles: polar, hoop and/or helical. Polar angle refers to fibres being aligned with the longitudinal axis of the cylinder (Figure 2.4a). Hoop winding refers to those fibres close to 90° with respect to the longitudinal axis, usually applied only in the cylindrical region of the pressure vessel (Figure 2.4b). Finally, helical winding pattern indicates fibres that are placed between 5° to 80° with respect to the longitudinal axis(Figure 2.4c) [13]. After fibre winding, the cylinder undergoes the curing cycle process, which is typically performed in an oven.

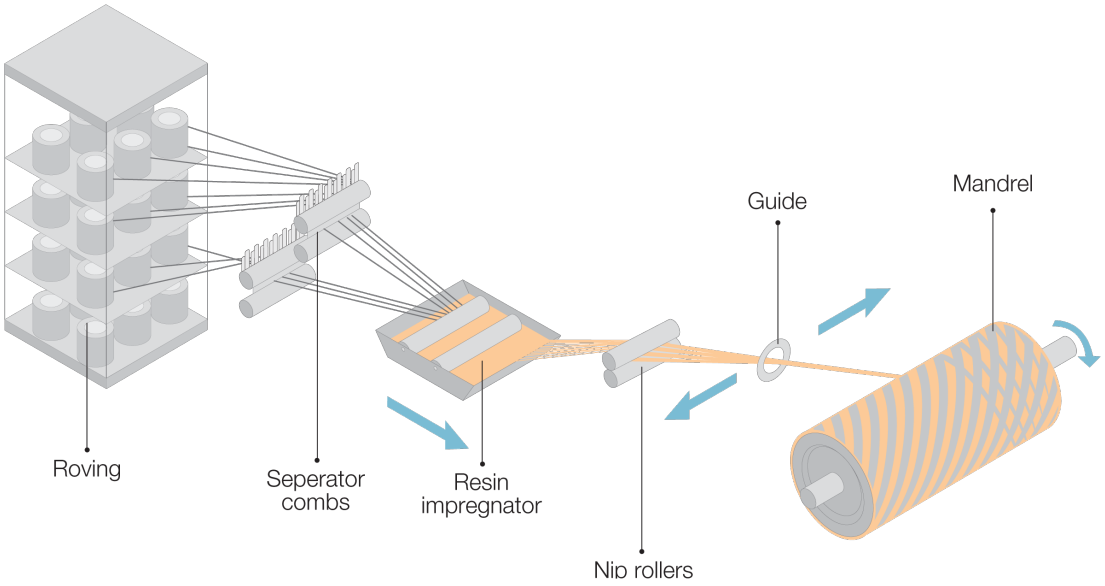

Figure 2.3: Filament winding process for tubular structures [16]

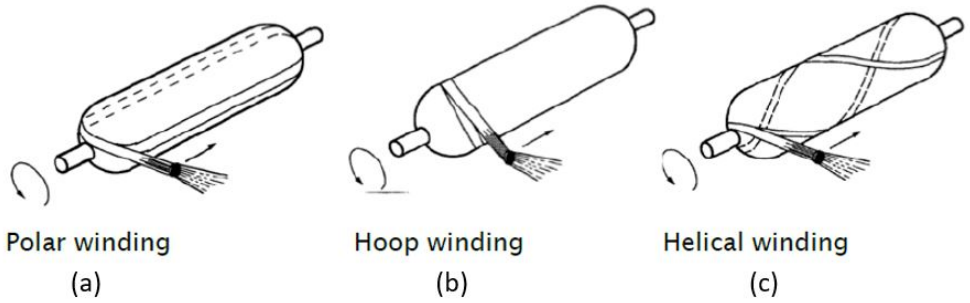

Figure 2.4: Typical filament wound patterns for COPV [13]

2.1.3 Autofrettage

Once a cylinder has been cured it typically undergoes a process called *autofrettage*. Autofrettage is the manufacturing process whereby a pressure vessel is exposed to a high proof pressure, commonly 1.8 to 1.9 times higher than its service pressure [17]. In all metal thick-walled pressure vessels, typically two different regions are formed on the inner and outer sections of the liner as a result of autofrettage: plastic region and elastic region. The former is the region where compressive residual stresses are formed, and the latter is where tensile residual stresses are formed (see Figure 2.5). This mechanism similarly occurs on hybrid metal-composite cylinders, however, in such case, the applied pressure exceeds the liner yield strength resulting in its plastic deformation [18]. As a consequence of the permanent expansion, compressive stresses are located in the metal liner and tensile stresses are induced in the composite layers. Autofrettage gives hybrid metal-composite pressure vessels some particular benefits. Hocine *et al.* [19] suggested that during the cooling stage of the curing cycle, a gap may appear within the metal-composite interface as a result of the difference in thermal expansion coefficients and the elevated curing temperature used for the composite layers. The autofrettage procedure eliminates this gap and enhances the interface between the two materials. Furthermore, due to the aluminium having a much lower yield stress value than the tensile strength of the composite, compressive residual stresses are formed in the liner. Consequently, mechanical lock between the two materials is formed. For a Composite Overwrapped Pres-

sure Vessels (COPV) this translates to the fatigue-sensitive metal liner being kept in compression, whereas the less fatigue sensitive composite layers carry an increased tensile load, which has the overall effect of increasing the fatigue life of the cylinder.

Figure 2.6 describes the autofrettage process schematically [17]. Autofrettage is developed in steps $[2 \rightarrow 4]$ where the proof pressure is applied and removed (Figure 2.6b). From $[0 \rightarrow 2]$ (proof pressure application) the liner undergoes elastic-plastic deformation, whereas the composite deforms elastically. When the proof pressure is removed, the composite moves from point A to point C elastically and remains in tension. This compresses linearly the aluminium liner in steps $[2 \rightarrow 3]$, followed by plastic compression from $[3 \rightarrow 4]$, introducing the compressive stress σ_c. When the cylinder is working in service conditions, the liner operates between 4 and 4', whereas the composite remains linear between C and B. As a consequence of the liner being pressurised under the $[4 \rightarrow 4']$ cycle, the fatigue life of the cylinder is increased.

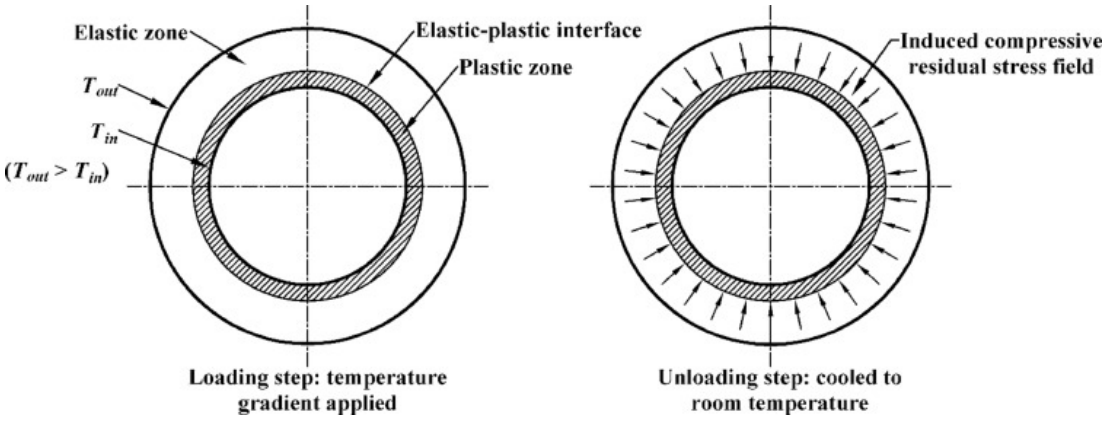

Figure 2.5: Residual stresses formed on cylinder regions as a result of thermal autofrettage process [20]

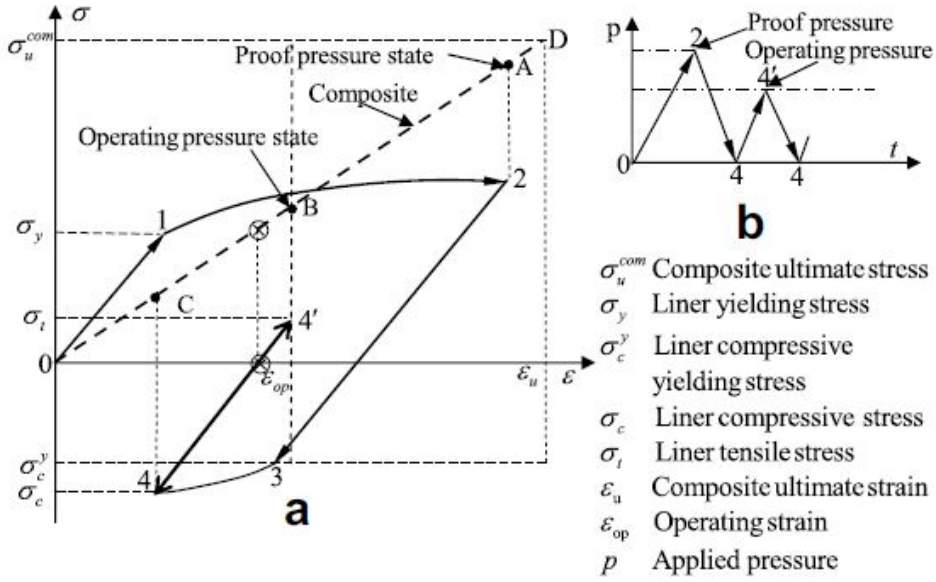

Figure 2.6: Autofrettage process on a Type III cylinder. From $[0 \rightarrow 2]$ *proof pressure application,* $[2 \rightarrow 4]$ *proof pressure removal, and* $[4 \rightarrow 4']$ *operating pressure*

2.2 Type III cylinder design standards

There are several international standards that specify the main design characteristics and inspection of cylindrical hybrid gas containers such as Type III, Type IV and toroidal vessels. One of the main requirements defined in these standards is the fatigue performance, in which is required that leak is the first failure before burst after a specified number of cycles. The requirements also specify service conditions, validation of manufacturing materials, life span, operating pressures and inspection methods [21]. Fatigue performance after induced impact events on pressure vessels is also defined on the standards. These requirements are starting to gain interest as cylinders are prone to be subjected to unexpected impact loads as a result of mishandling or a tool being dropped into them during transportation or in service. Some of the standards covering different cylinder types are listed and briefly described below [9, 21–23]:

- **ISO 11119-1: 2012**: Refillable composite gas cylinders and tubes — Design, construction and testing — Part 1: Hoop wrapped fibre reinforced

composite gas cylinders and tubes up to 450 l

- **ISO 11119-2: 2012**: Refillable composite gas cylinders and tubes — Design, construction and testing — Part 2: Fully wrapped fibre reinforced composite gas cylinders and tubes up to 450 l with load-sharing metal liners
- **ISO 11119-3: 2012**: Refillable composite gas cylinders and tubes — Design, construction and testing — Part 3: Fully wrapped fibre reinforced composite gas cylinders and tubes up to 450L with non-load-sharing metallic or non-metallic liners
- **ISO 11439: 2013**: High pressure cylinders for the on-board storage of natural gas as a fuel for automotive vehicles
- **ISO/TR 13086-1: 2011**: Guidance for design of composite cylinders — Part 1: Stress rupture of fibres and burst ratios related to test pressure
- **CSA/ANSI NGV 2-2019**: Compressed natural gas vehicle fuel containers. Defines requirements of material, design, manufacture and testing of refillable gas containers. Applicable for containers up to 1000 L capacity.
- **Dot CFFC: 2007**: Defines the requirements for design, manufacturing, construction and testing of fully wrapped carbon-fibre reinforced cylinders.

The specific cylinder types used in this research are covered by two main standards, the ISO 11119-2 and the DoT CFFC: 2007. The next sections present a deeper description of each standard.

2.2.1 ISO 11119-2

The ISO 11119-2 specifies a series of drop tests that involves impacting a single cylinder in five different locations (see Figure 2.7). The cylinder must be filled with water to half its capacity. It must be dropped from a height of 1.2 m onto a 10 mm thickness flat steel plate. Two different cylinders should be dropped, the first one must subsequently be tested for burst pressure failure and the second one for fatigue failure. For the first test, the passing criterion indicates that the

cylinder must not burst below 1.5 times the working pressure specified by the supplier. For the fatigue tests, the cylinder must accomplish 250 cycles per year of design life without a leak or burst pressure. According to the standard, one cycle is defined as a pressure/de-pressure process. Then, the cycle continues up to 500 cycles per year of design life during which only leak failure is acceptable. In any of the fatigue cases, in order to be approved, the cylinder must not burst during the specified number of pressure cycles [10].

This is currently one of the most acceptable standards for the design of hybrid pressure vessels. However, the impact tests described are not fully controlled. For instance, it is difficult to achieve an exactly 45° impact on the dome regions of the cylinder by only dropping them. Furthermore, the inspection described by the standard is not fully clear regarding the level of damage that should be acceptable in the liner/composite layers for the cylinder to be considered usable after impact, without the need of performing fatigue cycles. As a result, there is a possibility that the current design is conservative. Further internal damage inspection techniques should be included along with a better understanding of the damage development during impact, which can be achieved via numerical modelling.

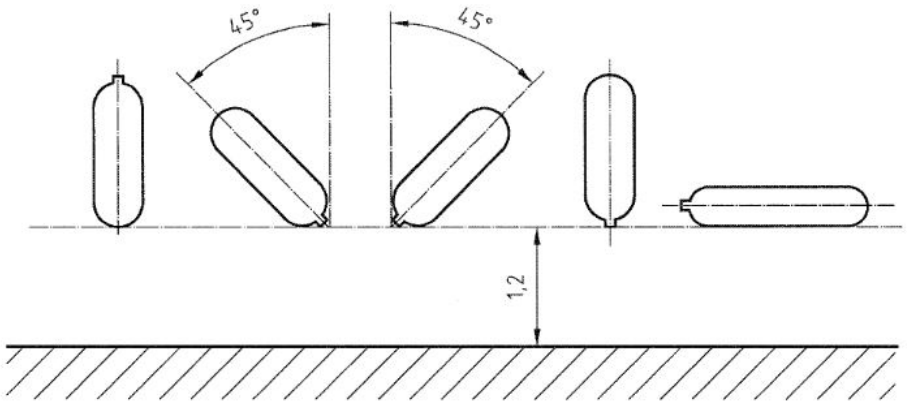

Figure 2.7: ISO 11119-2 different impact tests for a Type III cylinder

2.2.2 DoT CFFC: 2007

The USA Department of Transport (DoT) standard establishes the basic requirements to design, manufacture and define the performance of a fully-wrapped pressure vessel. This test indicates that three different drops should be performed on a single cylinder. The first two drops should be performed from 3.0 metres height using vertical and horizontal orientations respectively. The third drop must be performed at the same height in a horizontal position, however the cylinder should be impacted to a 90° angle-iron base at approximately the centre of the cylinder (see Figure 2.8). After the drop test has been performed, the cylinder must be subjected to 1000 pressure/depressure cycles at service pressure. The criteria to pass these tests indicates that the cylinder must not evidence any leakage during or after the pressure test [9]. It has been shown in [2] that the third drop test is the most critical for the Type III cylinder's fatigue performance because this kind of impact is strongly related to the permanent deformation in the liner that causes the metal-composite separation.

Similar to the ISO 11119-2, this standards has some opportunity areas that could be further explored in order to achieve a lighter more robust design. The lack of a well-described inspection technique along with a better methodology to perform the drop are also encountered in this standard. A more thorough inspection and investigation should be performed, specially with the most critical drop. With such information it would be possible to take decisions that could lead to optimal designs.

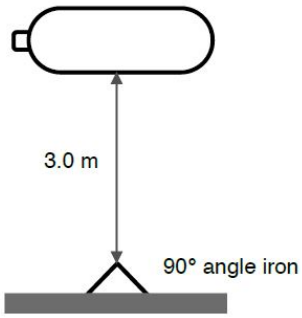

Figure 2.8: DoT CFFC 2007 drop test for a pressure vessel

2.3 Composite materials behaviour

A composite material refers to a type of material that can be made of two or more components. Typically, composite materials are manufactured using a continuous matrix in which reinforcement is embedded. The reinforcement is commonly in the form of fibres, whiskers or particles. In the current project, composite materials known as PMCs are being investigated. These type of composites are commonly made of a polymeric resin matrix reinforced with long fibres such as carbon, glass, aramid or natural fibres. During the manufacturing of composite components, unwanted defects may appear. As such, defects are usually small and difficult to detect in service, however their effect on the overall structural behaviour of the components is critical [24]. Thus, in order to gain an understanding of composites behaviour and develop safer applications, composite materials and structures have been widely studied from a multi-scale perspective. In this section, an overview of mechanical behaviour of PMCs is presented.

2.3.1 Damage in polymer matrix composites

Damage mechanisms in composite materials are commonly different from those observed in metals because composites exhibit distinct anisotropic properties. For instance, the impact energy absorption is mainly given by fracture mechanisms which reduce the strength and stiffness of the material. Conversely, metals may dissipate energy largely through plastic deformation. Typically, PMCs may undergo different failure modes such as *matrix cracking*, *delamination* and *fibre fracture*. At least one of these mechanisms usually occurs before ultimate failure (total separation of the part into two or more pieces). Figure 2.9 shows the different failure modes that can be observed in a PMC under tensile load.

2.3.1.1 Intralaminar cracking

In PMCs intralaminar cracking commonly refers to the cracks occurring in longitudinal or transverse to the fibres or within the inter-phase region. Usually, interlaminar cracking is preceded by fibre-matrix debonding. Such cracks can be challenging to detect as they can be small compared to other composite damage mechanisms, however, under specific loadings such as fatigue, these cracks can

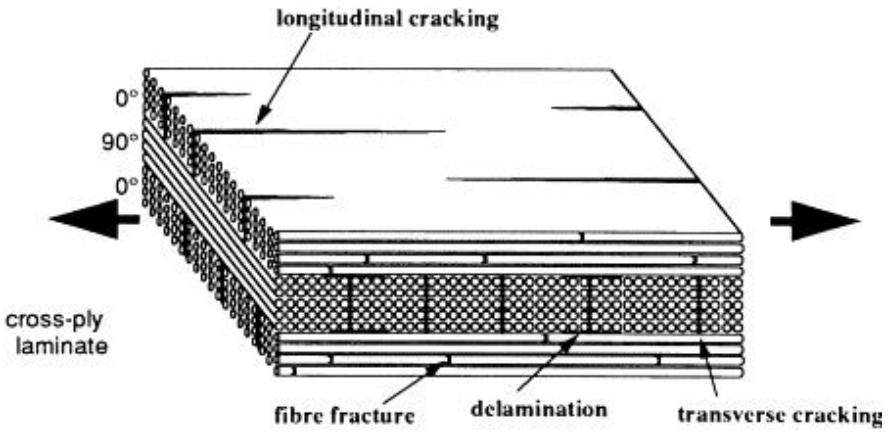

Figure 2.9: Common failure mechanisms on PMCs [25]

act as initiators for delamination, which lead to a more critical failure stage [26]. It has been reported that matrix cracking is strongly associated with the onset of other types of composite damages, such as clustering of fibre fractures or buckling [27, 28].

2.3.1.2 Delamination

Delamination is a damage mechanism that occurs as a result of interlaminar stresses created mainly by mechanical or thermal loads. Also, delamination can result from pre-existing matrix cracks, free edges, bonded joints, or joint specimens [29–31]. This mechanism has been widely studied as it is one of the most common failure modes in composite materials. It has been reported that delamination damage is more intense when a higher angle difference exists between two contiguous plies due to higher stiffness mismatch between plies, in combination with relative loading direction [27]. Based on the location within a structure, Bolotin [29] classified delamination in three different types: internal, near surface and multiple cracking (see Figure 2.10). Internal delaminations are difficult to detect during service conditions and their presence can result in a significant reduction of bending stiffness [32]. Surface delaminations are easier to detect, however, their presence can indicate a much larger internal delamination growth (multiple cracking). Investigations have been made in order to increase the fracture toughness of the interface between different plies and in this way reduce delamination within structures. The majority of the fracture toughness characterisation inves-

tigations have been developed through standard Double Cantilever Beam (DCB), Mixed-Mode Bending (MMB) and End Notched Flexure (ENF) tests and some variations based on them [33–35].

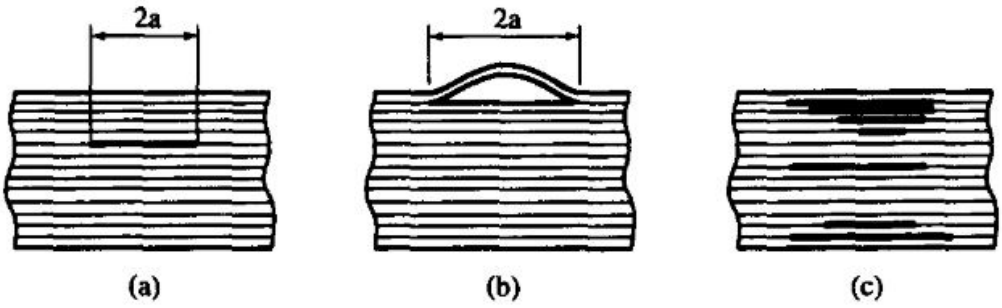

Figure 2.10: Different types of delamination on a composite structure; a) internal delamination, b) surface delamination, c) multiple cracking [29]

2.3.1.3 Fibre fracture

Under tensile loading, fibre fracture can be one of the last damage mechanisms before ultimate failure. Bishop [36] studied multiple defects on composite structures and suggested that even small numbers of fibre fractures can lead to a significant reduction of stiffness and strength of composites. In contrast to other composite damage mechanisms, fibre fracture is difficult to predict due to the nature of their construction. High strength carbon fibres are brittle, so governed by the weakest-link statistics. As a result, there will be a distribution of different fibre strengths that, as such, can be described using a Weibull distribution [28]. Due to this behaviour, it is difficult to predict the pattern in which fibre fractures will expand and produce a major composite failure. It has been reported that the energy associated to fibre fracture is greater than energy associated to matrix-dominated failure mechanisms, that is why, small regions of fibre fracture can dissipate as much energy as larger areas of matrix damage [24].

2.3.2 Low-velocity impacts on composite materials

To understand the importance of impact damage investigation on PMCs two concepts are introduced in this section: damage resistance and damage tolerance.

Damage resistance refers to the capability of a structure to *resist* initial damage formation under certain applied loads. On the other hand, damage tolerance refers to the amount of load that a structure can carry on the presence of pre-existing damage [37]. This concept is particularly important for composite structures due to the potential incidence of Barely Visible Impact Damage (BVID) occurring in the inner layers of composite materials. Hence, different methodologies are investigated to increase the damage tolerance properties of structures developed in industries with critical safety requirements, such as aerospace, aeronautical and automotive. The aim is to develop structures that can carry significant amount of load and residual lifetime after being exposed to LVI. Impact loads are of specific interest within the literature because they can produce BVID which may lead to a significant reduction of strength and lifetime, and ultimately, abrupt failure modes [24, 29, 35, 37]. LVI on composite materials has been widely studied, particularly for laminates. It has been reported that low impact energies can produce sufficient internal damage that can lead to several failure of components [38–40]. Figure 2.11 describes a particular damage pattern occurring in thick laminate composites after LVI. This damage pattern is well known in the literature and it has been studied through experimental and modelling research [41].

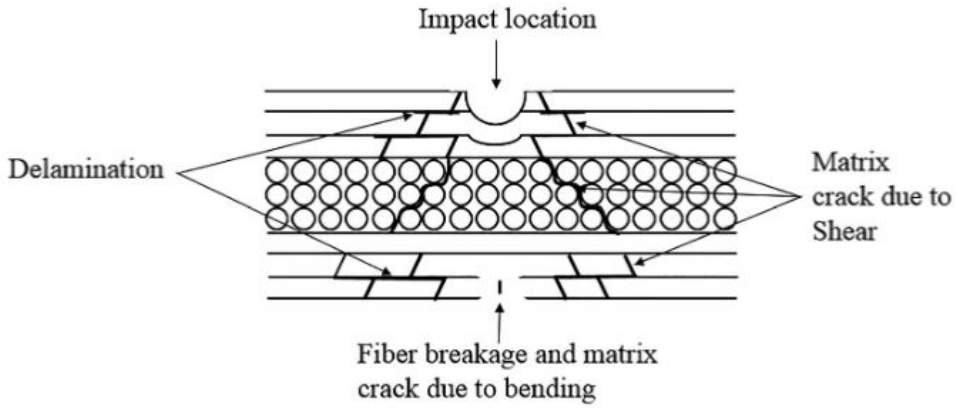

Figure 2.11: Damage mechanisms on fibre reinforced composite laminates as a result of low-velocity impacts [35]

Generally speaking, low-velocity impacts entail different failure mechanisms than high-velocity impacts, and their contribution to the overall structural

strength is different. For instance, during a high-velocity impact, damage observed typically shows a local deformation near the point where the impactor makes contact with the material. Conversely, during low-velocity impacts the contact is long enough to allow a wider area of the component to react, engaging more structure of the material and, as a consequence, more energy absorption through elastic means [37, 41, 42]. Although both mechanisms have been studied, no clear definition of a low-velocity impact has been found in the literature. Some authors define a low-velocity impact based on the velocity of the impactor itself, whereas other authors define the event based in the final damaged observed on the structure, which is related to the impact energy. Cantwell and Morton [43] indicated that impacts occurring at velocities between $1m/s$ to $10m/s$ could be defined as low velocity based on the extent of damage observed after the impact, which exhibits a global deformation. Bolotin [29] performed a series of experiments on laminated plates at different energy impacts, in which he defined low-velocity impacts as "low-energy surface impacts" (around 600J). This is, to some extent, supported by Liu and Malvern [44], who differentiate high and low-velocity impacts based on the damage generated in plate laminates. They indicated that high-velocity impacts involve major fibre breakage whereas low-velocity impacts principally cause delamination and matrix cracking. Other approaches such as the one from Robinson and Davies [45], suggest that low-velocity impacts should be considered as those in which through-thickness stress waves do not affect the stress distribution. It was indicated that using a typical failure strain of 0.5 and 1.0 % and a typical speed of sound in composites, a high-velocity impact may start at 10 m/s, which partially agrees with the values proposed by Cantwell and Morton.

Special interest is being given to post-impact behaviour in composite materials as the damage arising from these events can cause large losses in residual tensile, compressive, flexural strength and fatigue life of the material [37]. Bolotin [29] investigated the effect of delaminations arising from low-velocity impacts on graphite/epoxy, organic fibre/epoxy and glass fibre/epoxy laminates. Post-impact tensile, compressive and cyclic loads were performed together with residual strength and crack growth measurements. Results suggested that at higher impact energies more delamination occurred and the residual tensile and

compressive strength was reduced. Moreover, crack growth under fatigue loading occurred faster than in undamaged specimens. A similar study was developed by Yuanjian [46] focusing on post-impact fatigue performance of GFRP laminates with different stack configurations. Results indicated that impacted specimens have a significant reduction of fatigue lifetime compared to those without impact. Horn [47] *et al.* estimated fatigue lifetime on PMCs using thermoelastic stress analysis, and suggested similar conclusions as Yuanjian. The results presented in these investigations are in agreement with several authors in the literature [24, 48, 49].

Impact investigations on composite materials are not limited to fibre/epoxy resins. For instance, interest on Fibre Metal Laminates (FML) has been shown in different investigations because they combine the advantages of metals and fibre reinforced composites to enhance damage resistance and damage tolerance [50–52]. Similar to damage found in PMCs, damage mechanisms observed in these hybrid materials as a result of low-velocity impacts are delamination, through thickness cracks and permanent deformation in the metal layers (Figure 2.12).

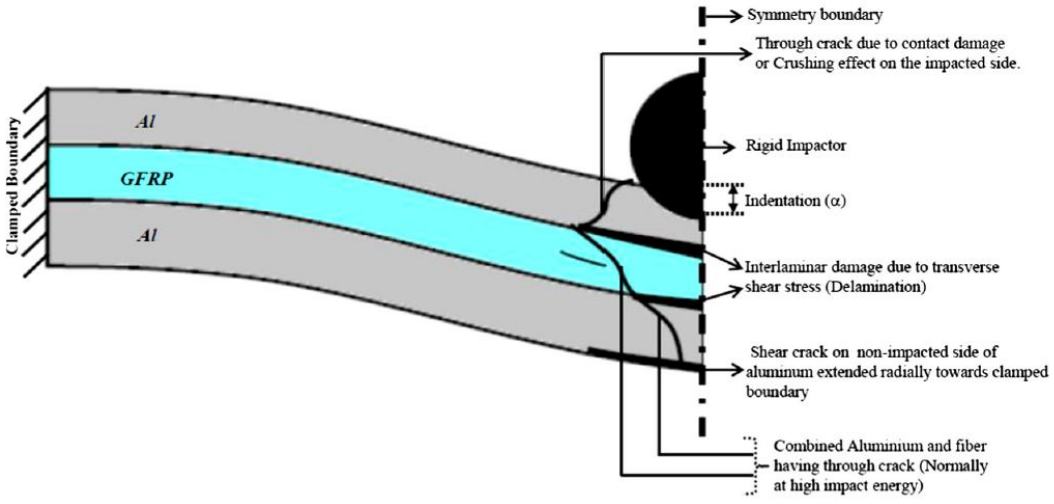

Figure 2.12: Damage mechanisms on fibre-metal laminates as a result of low-velocity impacts [50]

The most common configurations of fibre-metal laminates are aluminium plates bonded to a glass-reinforced (Glass Rinforced Aluminium Laminates (GLARE)), carbon-reinforced (Carbon Reinforced Aluminium Laminates (CARALL)) or kevlar-

reinforced (Aramid Reinforced Aluminium Laminates (ARALL)) composite laminates. Regarding impact, the main advantage of FML is that more energy can be dissipated through elastic means. Vlot [53] was one of the pioneers to investigate FML under impact loads. He performed quasi-static indentations, low-velocity and high-velocity impacts on GLAREs, CARALLs and ARALLs and compared the structural response to aluminium. The results suggested that the energies to create first fibre fracture in GLAREs is similar to that needed to develop fracture in the aluminium, whereas the energy needed to develop the same condition in CARALLs and ARALLs is significantly less. Thus, it was indicated that GLAREs show a more aluminium critical behaviour (depending on the ply layout), whereas a more brittle behaviour was exhibited by CARALLs and ARALLs. The effect shown by GLAREs is mainly due to a higher strain to failure. Data suggested that GLARE used in this experiment is more attractive for aircraft impact applications.

Laliberté *et al.* [54] investigated the impact response of GLAREs and tested three different structures, in which the inner glass fibre layer configurations were $[0^o/90^o]$, $[0^o/90^o/0^o]$ and $[0^o/90^o]_s$ respectively. These configurations are typically used for aircraft fuselages due to high energy absorption. It was reported that these structures were less susceptible to impact damage than PMC. Payeganeh *et al.* [55] showed that layer sequence, position of the aluminium layer, the mass of the projectile and the plate aspect radio have a significant influence on the final impact behaviour of FMLs. Morinière *et al.* [52] investigated the impact effect on FML using standard GLARE 5-2/1-0.3 and GLARE 5-2/1-0.4[1] through experimental testing and analytical modelling. Similarly to Payeganeh, results indicated the influence that mass of the projectile and position of the aluminium layer have. However, Morinière's analytical model was also used to evaluate the velocity, absorbed energy, contact time and maximum displacement of a low velocity impact on the test specimens. It was reported that aluminium layers have a damping effect during impact, and they dissipate 90% of the absorbed energy. In contrast, the composite layers help delaying crack propagation in the core of the specimen. This results suggested that GLAREs

[1]Composite core $[0^\circ/90^\circ]_s$ embedded between two same-thickness aluminium plates; 0.4 & 0.3 denote metal plate thicknesses in each specimen

are a suitable option for impact applications. Lawcock *et al.* [56] investigated the impact behaviour of CARALLs using specimens with different fibre/matrix adhesion. Results indicated that a weaker fibre/damage adhesion showed larger damage zones after low-velocity impacts. Furthermore, higher residual strength was shown with better initial matrix/fibre adhesion. These studies show the advantages of using FML structures, which are similar in construction to the cylinders used in this project.

Strain energy release rate and interface fracture toughness are often studied within FML as interface properties between the two different materials has a significant effect to the overall performance [57, 58]. Bieniás *et al.* [59] performed DCB and ENF experiments to determine the effect of loading mode mixity on the interface toughness in CARALLs and GLAREs. The results indicated that increasing fibre orientation near the metal interface can reduce the reduce the critical strain energy release rates. Furthermore, it was reported that GLARE laminates showed a higher critical strain energy release rate than CARALL laminates, which can be attributed to higher residual stresses after curing. Prawoto *et al.* [60] developed similar experiments on self-reinforced polypropylene (SRPP) and glass fibre reinforced polypropylene (GFPP) based FML. Compared to the investigation performed by Bieniás, surface treatments where applied to the metal laminate and it was shown that such treatment contributes to higher energy release rate values.

Investigations mentioned in this section were performed on flat plate specimens. Results reported on these experiments regarding fatigue, stiffness and strength will be modified by the geometry of a specific application or defects arising from the manufacturing process. Therefore, for design engineering purposes, it is important to perform similar studies on a component level with representative features including curvatures.

2.3.3 Damage in filament wound structures

Filament wound cylindrical components are widely used in industrial applications such as composite risers/pipes and pressure vessels. These structures were typically made from metals, however the high specific strength and stiffness, as well as the reduced density of composites, have increased the interest of indus-

tries to use these materials. Thus, research has been developed to increase the understanding of the behaviour of such components (*e.g.* impact, fatigue, effect of winding patterns etc). The present investigation is focused in damage development in COPV, however, given the geometric and construction similarities, investigations regarding impact behaviour on composite risers are also presented in further sections for reference.

2.3.4 Effect of winding pattern

The importance of an optimised filament winding angle is such that it has been widely studied in literature for different applications. Mertiny *et al.* [61] performed a series of experiments to investigate the effect of multi-angle layup configurations on the stress distribution of filament wound tubes subjected to internal pressure and biaxial tensile loads. Three different lay-up configurations were investigated in this study: $[\pm 60_3]_\mathrm{T}$ (baseline), $[\pm 45, \pm 60_2]_\mathrm{T}$, $[\pm 30, \pm 60_2]_\mathrm{T}$. It was found, that the multi-angle specimens showed a reduced extent of matrix damage, which translated in an improved strength under variable loading conditions (axial + hoop loads). Moreno *et al.* [62] studied the effect of winding angle on strength and buckling behaviour of thin and thick-walled filament wound glass/epoxy pressure vessels subjected to external pressures. It was reported that no significant influence was shown by the winding angle on strength or buckling behaviour. Nonetheless, this study only considers two winding angle configurations, which is contrasting to what was developed in studies mentioned above. Furthermore, analysis of filament winding angle effects is not restricted to cylindrical pressure vessels. For instance, it has been reported that toroidal pressure vessels are affected by modifying geodesic into non-geodesic winding patterns [63]. Studies suggest that a non-geodesic pattern provides a better stress distribution due to internal pressure, however these angles require a high slippage coefficient, which is the frictional force between the fibre tows and the mandrel surface [64]. However, it has been reported that the slippage coefficient is difficult to achieve in real practice [65–67]. Ellyin and Mertens [68] studied the effect of fibre orientation on fatigue behaviour of GFRP filament wound pipes under uniaxial and bi-axial fatigue loads. Results indicated that a better fatigue performance can be achieved using certain fibre direction combinations, however, special care should be taken

as manufacturing defects can arise from these configurations. Rousseau *et al.* [69] developed a similar approach for composite pipes, in which weaving effects were added to the components to investigate damage growth under internal pressure loads. In this study, inspection of damage led the investigators to suggest that at certain undulating regions of the pipe damage would start to grow, thus the interweaving of fibres inside the layers would act as a defect.

2.3.4.1 Damage in Composite Overwrap Pressure Vessels (COPV)

COPV are hybrid metal-composite structures usually made from a metal core wrapped with CFRP and/or GFRP. Typically, unexpected damage may arise from external objects impacting on the cylinders (*e.g.* a tool), a cylinder dropped as a result of poor handling or anything that can hit and thus induce damage during service. Low-velocity impacts on COPV have been reported by different authors [5, 70, 71]. Kobayashi & Kawahara [72] studied the effect of the composite wrap thickness on the residual structural response of an empty metal-liner pressure vessel subjected to quasi-static and impact tests. Results suggested that increasing the CFRP thickness contributes to an increased initial stiffness and a reduced aluminium liner deformation. Wakayama *et al.* [71] performed impact tests on filament-wound polymer vessels using three different types of low-modulus pitch-based carbon fibres. Using Computer Tomography (CT) to scan the specimens and observe the depth of the composite damage caused by different impactor shapes, data suggested that the depth of the damage caused by the impact had a correlation to the decrease in residual burst pressure strength. Blanc-Vannet*et al.* [73] studied the effect of increasing impact energies on empty thick polymer liner pressure vessels, and reported a reduction on residual burst pressure due to higher impact energies. Subsequent reductions in fatigue life have also been reported as a result of low-velocity impacts [74, 75]. Results indicate that a deeper composite damage, as a consequence of increasing impact energies, contributes to a greater reduction on the fatigue life of the cylinder.

Following hybrid metal-composite structures investigation, hybrid composite rings have been also used as an alternative experimental approach to investigate composite pressure vessels or tubes. Ha & Jeong [76] used rings to investigate the influence of winding angles on through-thickness properties of

thick wound filament composite tubes. Residual strain measurements were reported under various winding angle configurations. Eggers *et al.* [77] reported the structural force-displacement response and damage mechanisms of filament-wound composite rings under hoop tensile and radial compression loads. Specimens were manufactured under different winding angle, diameter-to-thickness and stacking sequence conditions. Similarly, Weerts *et al.* [78] investigated residual strains on thick-walled composite cylinders with a polymer liner subjected to compression loads. These approaches used quasi-static tests to induce damage on the specimens, which has been reported to be a valid approximation to LVI [11, 72, 79, 80].

However, either using full cylinder, pipes or rings, the research performed around hybrid metal structures mainly focus on onset of damage occurring on the composite layers of the structures. Allen *et al.* [11] performed LVI tests followed by continuous and interrupted quasi-static indentation tests on Type III cylinders. From this study, it was concluded that there is an equivalence in damage response between an LVI and quasi-static indentation tests, which corresponds to the observations made by Curtis *et al* [80]. In both tests, metal-composite de-cohesion was observed, as well as delamination and fibre breaks. Furthermore, evidence was presented by Allen [2] to conclude that the final depth of the residual dent observed after the quasi-static indentation has a significant correlation to the post-impact fatigue performance of the cylinder. Considering the impact tests required by both ISO 11119-2 and DoT standards (see Section 2.2), plus the strong correlation between the indentation depth and fatigue life of Type III cylinders, deeper investigation of the interface properties between the liner and the CFRP should be performed.

2.3.4.2 Damage in composite risers

Composite risers are a similar application with structural construction comparable to that found in metal-composite pressure vessels. As such, both pressure vessels and composite risers have similarities on impact damage and fatigue behaviour and they are both prone to similar damage modes due to internal pressure and unexpected LVI, which will have a significant effect on fatigue performance [75]. In the case of composite risers, they are exposed to loadings such as buck-

ling, tension and compression induced by the currents and surface waves, external hydrostatic pressure and fluid pressure. Furthermore, unexpected loads in form of an impact may arise from dropped tools or trawl board impacts [81]. Because of these loads, risers are widely investigated within the literature. Ellyn *et al.* [82] studied filament wound tubes under biaxial loads and developed stress-strain curves. In a further study, Ellyn and Martens [68] developed fatigue life curves and fatigue envelopes of composite pipes subjected to biaxial loads. Mustafa *et al.* [83] investigated the damage process on composite tubes by performing lateral indentations on them. They used their experimental results to develop FE models in $Abaqus^{TM}$. Force-displacement curves were reported in the results of this study along with residual shape prediction. However, the model had some discrepancies with the experimental results, particularly at larger indentation values. The reason behind these discrepancies could be the simplification of the materials, as they were only using elastic properties, as well as shell elements. Curtis *et al.* [80] further investigated by comparing the quasi-static results to lateral low-velocity impacts, and concluded that the damage in both cases was similar. These studies provide an important understanding of composite tubes behaviour, however there are some areas that have not been deeply explored such as the metal-composite interface and deeper modelling in this regards.

2.4 Finite Element Modelling

2.4.1 Modelling on Type III cylinders

Generally speaking, finite element modelling has been widely used to investigate composites from the micro, meso and macro-level point of view. Models have been developed to study fibre behaviour, individual ply behaviour and/or complete structural behaviour. The current project investigates composites behaviour from a ply-level perspective.

There are some relevant numerical models developed. Changliang *et al.* [84] developed a FE damage model on the composite layers of hybrid pressure vessels. Results for fibre and matrix fracture on the outer layers of the pressure vessel were reported from this model with good agreement to experimental results.

Kim *et al.* [75] investigated the effect that induced flaws on the outer composite layers have on the fatigue performance of metal-liner COPV. Results suggested that a deeper flaw contributes to a greater reduction of cylinder's fatigue life. No delamination or fibre/matrix damage was considered in Kim's model, however good agreement between experimental and modelling results was reported. In the same context, Sulaiman et al. [85] developed a Type III FE model to investigate the influence of the fibre angle orientation over the cylinder's burst pressure performance. Prediction of burst pressure and shell displacement were performed using the maximum stress as the failure criterion. Moreover, based on Tsai-Wu and Tsai-Hill failure criteria it was shown that a 55° winding angle (with respect to the longitudinal axis) provides a better fatigue life performance. These models were developed using a microscale approach, however further COPV modelling has been reported using ply-to-ply basis approach for more mesoscale modelling focusing on delamination between CFRP layers and liner separation resulting from impact and internal pressure loads [86, 87].

Son et al. [88] proposed different modelling approaches to model metal-composite pressure vessels subjected to internal pressure loads and validated them through experimental tests. Their model used plastically deforming aluminium liner and a perfectly elastic carbon/epoxy for the composite wrap. A simple contact was simulated between both material layers, *i.e.* no perfect bonding nor interface properties were assumed. The approaches proposed by Son were a full ply based modelling, a laminate-based modelling and a hybrid modelling technique which combines the first two. It was reported that these models were used to model the stress distribution resulting from the pressure loads. Results showed that the ply-based modelling technique exhibited the best agreement to experimental results. The other two techniques showed an overestimation of the stress distribution. This study focused on the damage developed on the outer layers as a result of pressure loads, that is, no LVI load was assessed. Nonetheless, this modelling techniques were used to determine the autofrettage pressure and assess the influence of residual stresses on the final stress distribution on the outer layers of the composite. A similar modelling approach was taken by Han *et al.* [89] which modelled a hybrid metal-composite vessel under free fall impact. This FE 3D model used Hashin's criterion to determine fibre fracture, matrix crack

and delamination in the inner layers of the cylinders and, thus, it is possible to suggest whether the cylinder can be re-used or not. This model was later used to predict damage on COPV in a car-to-car collision simulation [90]. Kobayashi *et al.* [91] used elasto-plastic FE modelling approach to evaluate residual burst pressure of hybrid metal-composite pipes. Results showed residual stresses after pressure loading and residual burst strength after low-velocity impact. Both models showed good agreement prediction results for composite damage after impact, however it is not clear at what extent of damage the cylinder would still be re-usable.

The modelling approaches mentioned above were focused on investigating damage on the composite layers of the vessels and only few studies assess damage on the liner [78, 86], however these are on polymer liner pressure vessels. It has been suggested that as a result of LVI, hybrid metal-composite pressure vessels exhibit a separation of the metal-composite interface and a residual indentation on the aluminium liner [5], similar to that shown in Figure 2.13. Allen *et al.* [2] performed quasi-static point indentation tests on hybrid COPV as a proxy for LVI. Force-displacement curves were obtained to analyse the structural response of the whole cylinder under this loading (Figure 2.14a) and study it in relation to the residual depth observed on the metal liner. Results suggest that there is a correlation between the depth of the dent and the post impact fatigue life of the specimen (Figure 2.14b). Based in the results, the effect of reducing the amount of residual plastic deformation on the liner should be investigated.

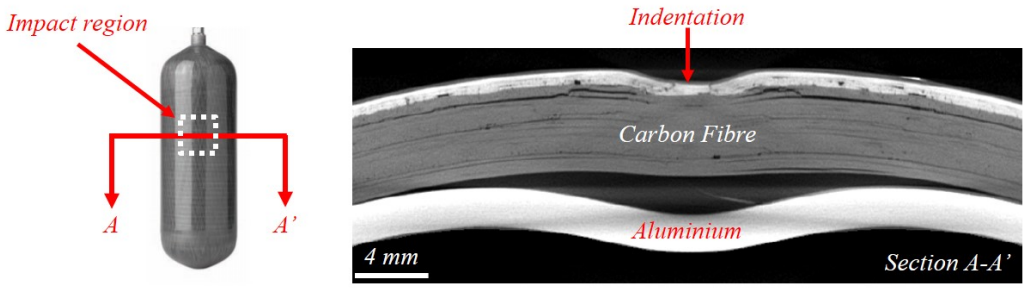

Figure 2.13: CT image of metal-composite delamination within a COPV after quasi-static loading [2]

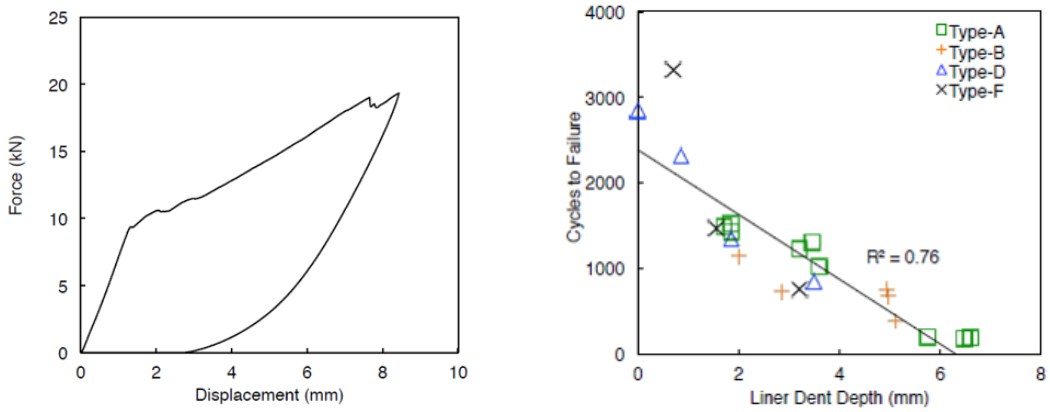

(a) *(b)*

Figure 2.14: COPV quasi-static loading behaviour: a)Force-displacement curve response after indentation loading; b)Correlation between liner dent depth and fatigue life [2]

2.4.2 Delamination modelling approaches

The de-cohesion occurring after indentation of a Type III cylinder can be treated as a delamination problem. Additionally, it has been reported that along with metal yielding, a significant amount of composite delamination occurs during the LVI event. Therefore, the main modelling activities within this project are related to the development of delamination modelling techniques in order to reproduce the permanent deformation within the liner with an appropriate parameter selection. Due to the increasing use of composite materials within industry (especially aerospace and automotive) many efforts have been developed to establish adequate criteria to analyse and predict failure in composites. Although composites develop different damage mechanisms (see Section 2.3.1), there is a particular interest in delamination [26]. Delamination failure can occur in Mode I (opening), Mode II (sliding) and Mode III (tearing) (see Figure 2.15), and current FE models can assess each type depending on the simulation requirements [92].

Current methodologies to simulate delamination numerically can be divided in *a*) direct application of fracture mechanics and *b*) applying damage mechanics or softening plasticity. Within these two groups techniques such as *J*-integral, the virtual crack extension, Virtual Crack Closure Technique (VCCT)

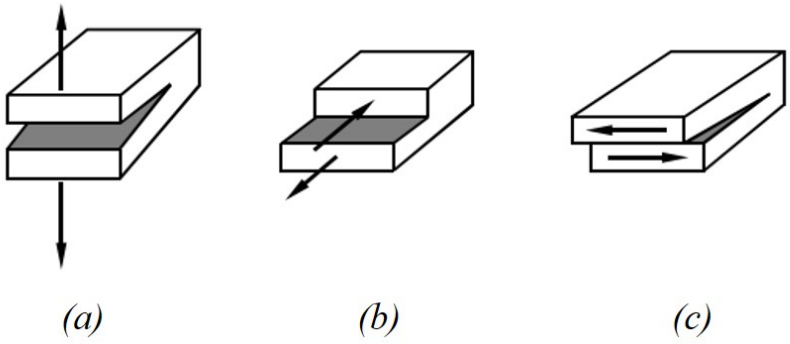

Figure 2.15: Delamination failure modes; a)opening, b)sliding, c)tearing [92]

and Cohesive Zone Model (CZM) are the most common. However, due to the ease of application to finite element codes, the last two are the most widely reported in the literature [93].

2.4.2.1 Virtual Crack Closure Technique

The VCCT is based on fracture mechanics and widely used to calculate strain energy release rate. It involves two main assumptions: *a*) the crack propagates when the required energy release rate is greater than or equal to a critical value; and *b*) a small crack extension Δa does not changes the location of the crack tip significantly [35, 93, 94]. VCCT is based on the assumption that the energy δE released by the crack extension δa, is identical to the energy required to close the same extension [94]. Considering Figure 2.16 the energy release rate in mode I and mode II, G_I and G_{II} can be calculated from equations 2.1 and 2.2.

$$G_I = -\frac{1}{2\Delta a} Fy_i(v'_l - v'^*_l) \tag{2.1}$$

$$G_{II} = -\frac{1}{2\Delta a} Fx_i(u'_l - u'^*_l) \tag{2.2}$$

where Fy_i and Fx_i are shear and opening forces at nodal point i respectively. Here, the total energy release rate would be $G_T = G_I + G_{II}$.

Similarly, for a 3D FE model (Figure 2.17) the energies in mode I, mode

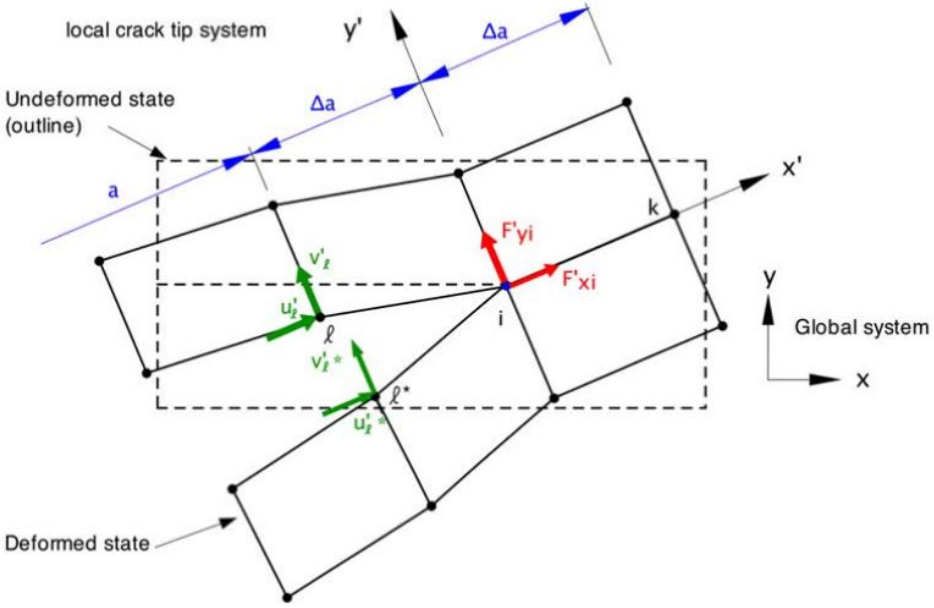

Figure 2.16: VCCT method in 2D [95]

II and mode III are calculated as:

$$G_I = -\frac{1}{2\Delta A} Fy_i(v'_l - v'^*_l) \tag{2.3}$$

$$G_{II} = -\frac{1}{2\Delta A} Fx_i(u'_l - u'^*_l) \tag{2.4}$$

$$G_{III} = -\frac{1}{2\Delta A} Fz_i(w'_l - w'^*_l) \tag{2.5}$$

where $\Delta A = \Delta a b$, Fy_i, Fx_i and Fz_i are shear, opening and tear forces at nodal point i respectively. The total energy release rate is given by: $G_T = G_I + G_{II} + G_{III}$ [94].

Although VCCT was initially used for cracks in linear elastic and isotropic materials, it is currently widely used for crack prediction within orthotropic materials [94]. Pirondi et al. [96] developed standard DCB, ENF and MMB tests to compare VCCT and CZM. Additionally, the models were used to to predict cracks under fatigue loading. Results showed good agreement between both modelling methodologies, except for the beginning of the fracture propagation where

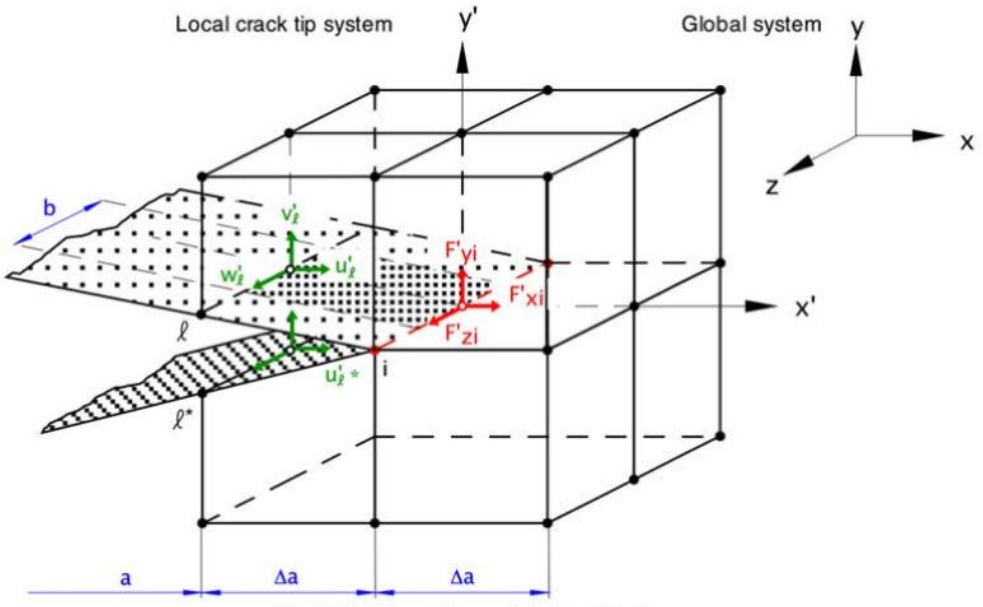

Figure 2.17: VCCT method in 3D [95]

small differences were observed. Such differences were attributed to mesh size , however no evidence was provided to support this conclusion. In a similar way, Perince et al. [97] developed a VCCT model to reproduce delamination in composites that can migrate through the thickness. Prediction of energy release rate values in their tests was critical, thus VCCT was used and it demonstrated acceptable prediction values. Good correlation behaviour to experimental results was demonstrated as well.

VCCT technique has some limitations that do not affect the accuracy of the method but increase the complexity of its application, thus making it less attractive for industrial projects [35]. One of the main disadvantages is that the method on its own is not capable of predicting crack initiation, hence it is restricted to problems where the information of the initial crack is available or where it is acceptable to assume certain initial crack size and location. This can also be solved by implementing a separate stress-based criteria, however it increases complexity when applied to a commercial code. Furthermore, as the method is based on the Linear Elastic Fracture Mechanics (LEFM) framework, problems can arise if the plasticity developed ahead of the crack tip is non-negligible.

2.4.2.2 Cohesive Zone Models

The concept of cohesive zones was first introduced by Dugdale in 1960 [98] when he analysed the effect of a small plastic zone ahead of a slit in a steel plate subjected to tension loading. However, this method was first implemented numerically around 1976 by Hilleborg [99] through a concrete beam bending model. CZM combines damage and fracture mechanics approaches, which allows prediction of damage initiation and damage propagation without the need for initial crack information. This characteristic makes the CZM technique potentially more attractive to develop industrial applications as the implementation of the method is simpler than in the VCCT scheme, and may be possible to use with a coarser mesh.

CZM is based on the premise that a softening zone exists ahead of a crack tip in a material and, within this region, the crack propagation is resisted by cohesive tractions [100]. The softening zone is defined by a traction-separation relationship which follows a cohesive law (see Figure 2.18). Delamination is described using this traction-separation relation and the parameters that defines it in pure mode I, mode II and mode III: interface strength ($\sigma_I, \sigma_{II}, \sigma_{III}$), interface fracture toughness ($G_{Ic}, G_{IIc}, G_{IIIc}$) and final surface displacements δ_f. The interface strength is the maximum stress needed to separate one surface into two new ones and promote the propagation of the crack [101]. Delamination onset occurs when the interface strength at each mode has been surpassed. Moreover, the interface fracture toughness is the property of the material to resist crack growth. As such, delamination occurs when the energy release rate G is higher than a critical value G_c, which represents the area under the traction-separation curve. For mix-mode delamination, G is related to the interface fracture toughness as $G = G_1 + G_{shear}$ where $G_{shear} = G_{II} + G_{III}$ [102].

From a traction-separation law such as the one shown in Figure 2.18, the values of σ_{max} and δ_f can be defined in such way that the energy absorbed per unit crack area is equal to the critical fracture energy of the material G_c [103]. Furthermore, G_c and σ_{max} can usually be either measured or estimated with some certainty, to allow physically realistic values to be chosen.

CZM is often applied using interface features which can be in the form of surfaces or elements. Cohesive surfaces involves defining the traction-separation

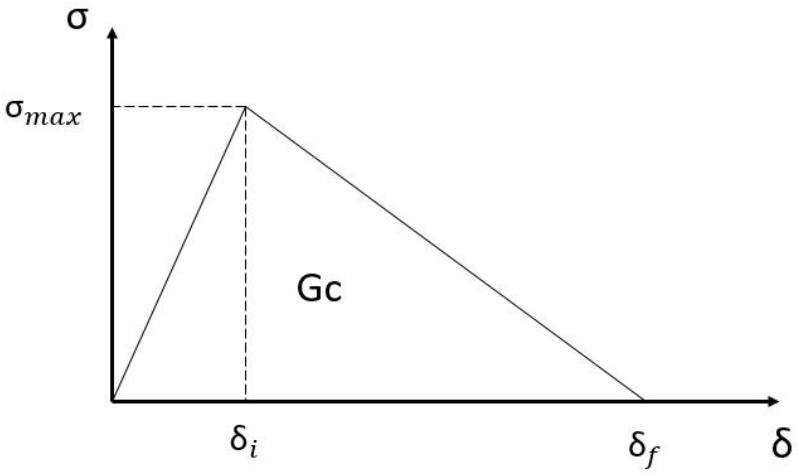

Figure 2.18: Bilinear traction-separation law; where σ_{max} is the strength at damage initiation; δ_i separation at initiation, δ_f is the displacement at failure and G_c is the energy release rate

law as a contact interaction between two surfaces. Here, the main advantage relies on the ease of the model definition, however as the cohesive formulation is constrained to each node the simulations can be more computationally expensive. On the other hand, the cohesive elements include the traction-separation law and, as elements are used, this method allows thickness control, which can be useful to model thin layers of adhesive in certain applications. Although cohesive elements demand more set up time, this methodology permits more control of the damage initiation and propagation parameters, which is useful when little information is available regarding the interface between two separating surfaces [103]. Because of the advantages that CZM offers over VCCT, this technique is widely used within composite modelling, specially for delamination problems [103].

Another important cohesive element parameter that has been widely studied in literature is the length of the cohesive zone L_{cz} [92, 104–106]. This parameter represents the cohesive region existing ahead of the crack tip. Within this region, the interface elements remain on the softening part of the traction-separation law. Figure 2.19 shows the development of the cohesive zone within a FE model. The cohesive zone starts where the elements near the crack tip (see Figure 2.19 element-1) quickly move to the softening region of the traction-

separation response; then it ends where *some* elements located ahead of the crack tip reach their maximum interfacial strength (see Figure 2.19 element-5). It is important to clarify that the definition above refers to the numerical cohesive zone length, which is different from the physical cohesive zone length defined as the length over which permanent damage has occurred. Within the literature it is recommended to use around three to five elements within the cohesive zone length to achieve accurate results [106].

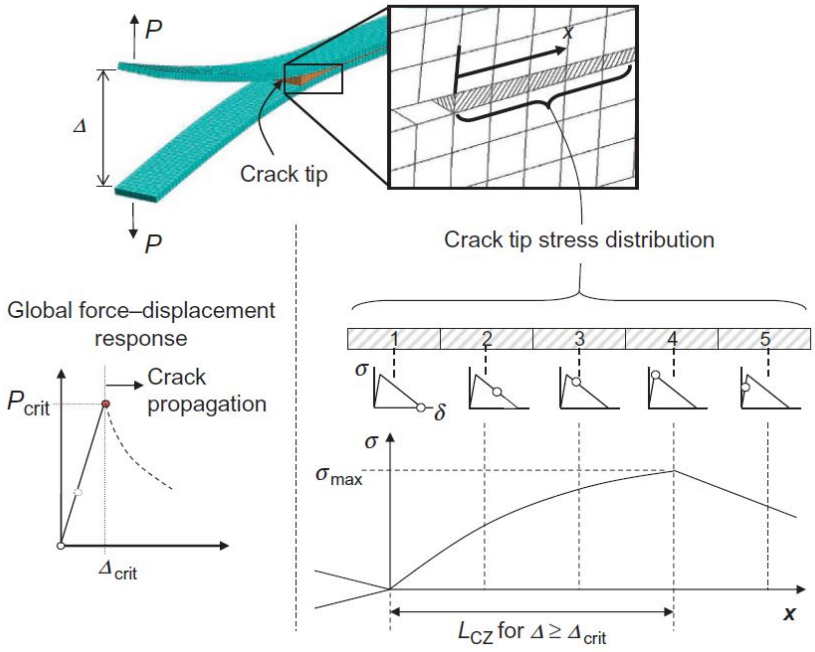

Figure 2.19: Development of cohesive zone length in a FE model [104]

As in the VCCT case, when the CZM is used on a FE model to perform certain analyses, validation is performed through standard DCB, ENF and MMB tests. One of the most cited authors in the field, Camanho et al. [107], developed 3D implicit cohesive models of these tests to validate mixed-mode progressive delamination in a composite material. He proposed a softening law based on the Benzeggagh-Kenane criterion which can be used in Modes I, II and III. Harper and Hallet [108] developed FE DCB, ENF and MMB models to investigate the optimal number of elements within a cohesive length. In a similar way, Turon [106] performed these analyses and reached the same conclusion: three to five

elements. However, the work developed by Turon not only aimed to determine the optimal number of elements in the cohesive zone, but showed that by modifying the strength of the cohesive elements a bigger element size could be used. This can be used to perform coarse-mesh analyses with a reduction of the computational cost and negligible effect on the final result.

2.5 Experimental background

This section briefly describes the experiments developed in [2] to show the main characteristics used to develop the analogous FE model within this project. The experimental test set up along with the main results is also shown.

2.5.1 Quasi-static indentation experiments

Quasi-static indentation tests on Type III cylinder were conducted to observe onset of damage and propagation resulting from a LVI. Validity of using quasi-static indentation tests as an approximation to LVI has been already discussed in Section 2.3.4.1. The tests were performed on a standard universal electromechanical test machine. Cylinders were positioned horizontally on a steel v-shaped support specifically designed for this purpose. After positioning the cylinder, a 16 mm diameter hemispherically-ended tup was used to perform the indentation on the central area of the barrel region of the pressure vessel (Figure 2.20). The indentation was developed at a loading rate of 2 mm/min for each cylinder.

In the present research only one Type III cylinder model was used to develop and validate the FE model. For more information regarding further tests of different Type III cylinder models refer to [2]. The cylinders used in this project were manufactured by Luxfer Gas Cylinders specifically for research purposes. This model was selected based on the extent of information extracted from the previous experiments and results reported by Allen. In terms of manufacturing materials, the liner was manufactured using an aluminium 6061-T6, and the composite wrap is CFRP with an outer layer of GFRP to protect the carbon layers. The cylinder should have an even number of hoop and helical layers, in which the hoop plies are $\approx 0^{\circ}$ and helical are $\pm 71^{\circ}$. Moreover, the ply stacking

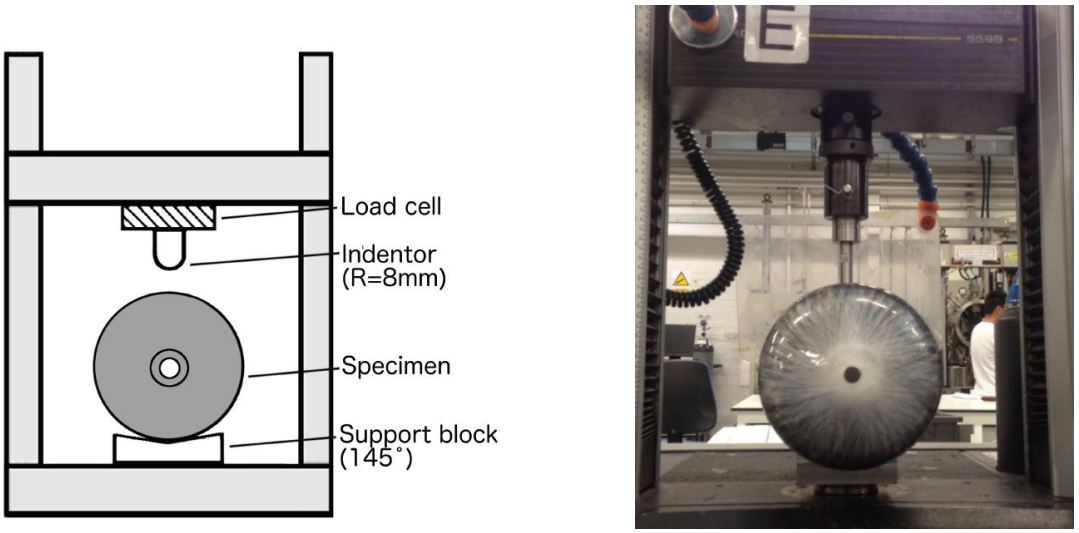

(a) (b)

Figure 2.20: Quasi-static indentation test of a Type III cylinder [2]; a) Experimental set up schematic, b) Experimental indentation on cylinder

sequence within the cylinder is $[0°/\pm 71°]_3$. For this project and hereafter the fibres aligned in direction of longitudinal axis of the cylinder will be considered as 90°, whereas the fibres in the hoop direction will be designated as 0°. Table 2.1 shows a summary of the geometrical and manufacturing characteristics of the cylinder used in this project.

Table 2.1: Type III cylinder specifications

Water volume (l)	Length (mm)	Outside diameter (mm)	Liner thickness (mm)	Thickness of CFRP (mm)	No. of CFRP plies	Thickness of GFRP (mm)
6.8	525	159	2.2	4.6	6	1.0

2.5.2 Quasi-static indentation results

A typical experimental force-displacement (F-d) curve of the quasi-static indentation test is presented in order to give an idea of the responses that are sought from the FE model. Figure 2.21 shows the F-d curve described by a Type III

cylinder subjected to a point indentation. Additionally, the curve shows a series of CT scan slices of the internal layers of the cylinder under the indentation region. The behaviour shows an initial elastic response from the structure followed by change in the slope of the curve, resulting from a reduction in the effective cylinder stiffness caused by the yielding of the material (confirmed via CT scan). The yielding of the liner leads to the next damage mechanism which is the onset of delamination of the composite layers. Towards the end of the loading phase of the curve, there is a noticeable load drop. It was reported that this load drop is related to matrix cracking and fibre fracture damage mechanisms. During the unloading phase of the curve, the undamaged composite regions recover elastically, while the metal liner exhibits a certain level of spring back, but a permanent residual deformation is now developed. The evidence presented at this point of the research suggested that this difference in material behaviour during load removal was the main cause of the material separation observed in Figure 2.21d, *i.e.* the separation mechanism is mainly driven by mode I delamination.

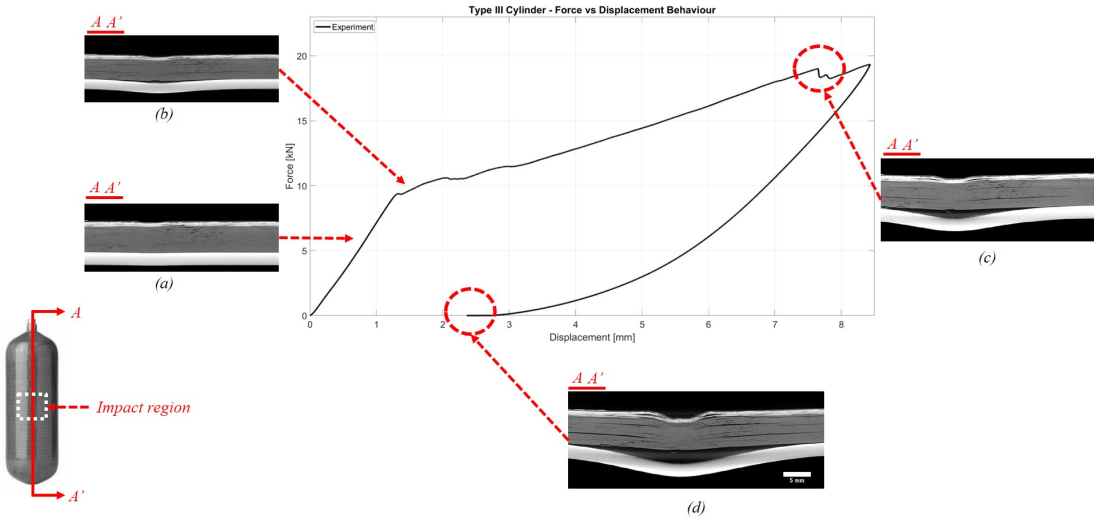

Figure 2.21: Force-displacement curve of a Type III cylinder under quasi-static indentation [2]

2.6 Conclusions from the literature review

Whilst current Type III cylinder design complies with the required standards, there is still a lack of understanding in the mechanisms governing damage propagation and damage tolerance. An example of this was observed in the work presented by Allen [2] in which de-cohesion was observed within the aluminium-composite interface after a quasi-static indentation test. It was indicated that the permanent deformation in the liner drives the post-impact fatigue performance of the cylinder, and thus, development of this particular damage mechanisms should be further investigated.

From the modelling point of view, the projects presented in [90, 109] remarked the importance of using the autofrettage residual stresses in the modelling of a Type III cylinder under impact loading. Furthermore, it was concluded that the metal-composite de-cohesion in a Type III cylinder can be investigated as a delamination problem. Two of the most cited techniques to model delamination were described along with their use in different investigations [105–107, 110]. This information was used to define the most appropriate method for this project, which is described in further chapters.

The advantages and disadvantages of using an implicit or an explicit scheme were reviewed. It was noticed that delamination damage can be modelled using either of those schemes, however each one introduces different initial conditions and modelling parameters depending on the nature of the problem. For this project, the explicit scheme was selected given the significant amount of non-linearities arising from the nature of the problem (*e.g.* plastic deformation, large displacements and composite delamination) and the potential need to model dynamic problems (drop tests, high velocity impact, whole car crash simulations) in the future.

Chapter 3

Experimental background and modelling methods

This chapter presents the experimental and modelling methodologies used throughout the project. First, an introduction to DIC is presented highlighting the main characteristics and the procedure to be used in this project. Regarding the modelling methodology, cohesive elements are presented as the key FE technique to model the interface between different materials which are part of a Type III cylinder construction. Furthermore, selection of explicit simulation parameters is presented by describing the main assumptions to perform a quasi-static simulation using an explicit solution scheme. Such parameters are validated by performing standard FE DCB and ENF tests. Results and conclusions regarding the selection of such parameters are also presented and discussed. Details of experimental techniques and computational models will be presented as they are used in Chapters 4, 5 and 6.

3.1 Digital Image Correlation (DIC)

This section presents a brief summary of the main characteristics and general steps related to the development of an experiment using DIC for strain measurements. DIC is commonly used as a full-field optical method to track deformations (strains) on a surface of a test specimen throughout a mechanical test [111, 112]. DIC can be applied to a wide variety of applications because it is a non-contact

technique, which means it is independent of the material or length-scale of interest, *e.g.* it can be applied on a small coupon or on a full assembly.

To perform this technique coordinates and displacements are obtained from time series digital images taken directly from patterns applied on a surface of a test specimen (see Figure 3.1). This is achieved by computationally dividing the field/pattern into smaller subsets and then analysing the displacement in each subset [113]. Here, the main assumption is that the pattern on the surface follows the same deformation path as the surface on the specimen. Then, the displacements obtained during the test are processed (correlated) to produce full-field displacements that reproduce the shape, deformation and motion from the pattern on the surface [111]. Figure 3.2 briefly describes the DIC process development from discretised subsets to obtaining a strain field.

Figure 3.1: Speckle pattern applied on a sphere for DIC testing [112]

DIC can be developed in 2D or 3D. A 2D (*a.k.a* 2D-DIC) configuration means that only in-plane displacements are tracked. On the other hand a 3D configuration measures the coordinates including out-of-plane displacements. This 3D method requires a minimum of two cameras in a stereo-angle configuration, known as Stereo-DIC. Although both 2D-DIC and Stereo-DIC require initial calibration, the latter becomes more complex as it is required to establish communication between the two cameras; in other words, information about the location and orientation of the cameras along with their distance to the test specimen is provided with the calibration and is critical to obtain accurate measurements. The specific details regarding the use of DIC in the current project are described in Chapter 4.

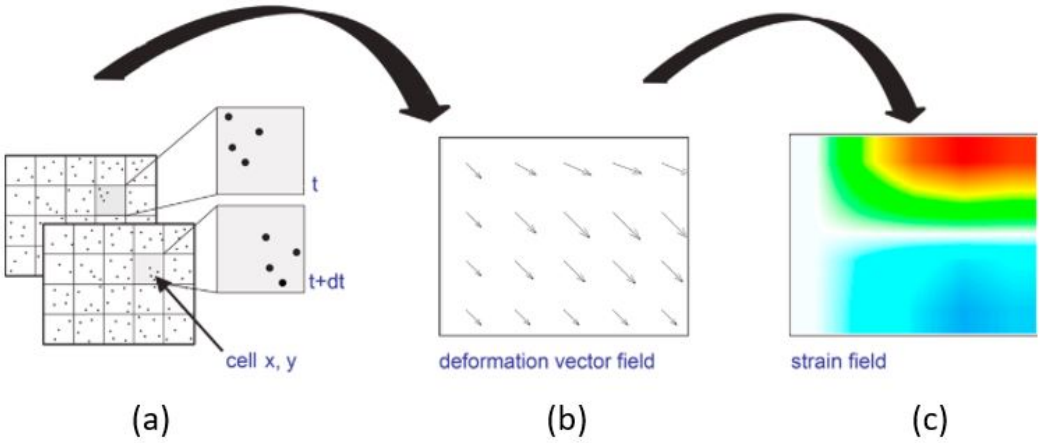

Figure 3.2: DIC process: (a) Subset discretisation; (b) Vector correlation; (c) Full strain field [113]

3.2 Interface modelling with cohesive elements

This section gives a brief description of the different processes to define a cohesive model within *Abaqus*^{TM} is presented. Generally speaking, the process to define a cohesive element involves defining different sections of a bilinear traction-separation law (see Figure 2.18); that is: elastic behaviour, damage initiation criterion and damage evolution criterion. Each process is described in further subsections.

3.2.1 Linear elastic behaviour

The first part of the bilinear traction-separation law is described by the elastic behaviour, which has a stiffness K_n. Within *Abaqus*^{TM}, K_n works as a *penalty stiffness parameter* because the actual value of the interface stiffness is not known. Although K_n is a well-defined parameter in cohesive models, the choice of a value for it, and its physical significance is less clear. There are many different values proposed for this parameter because it should be large enough to ensure an acceptable bond between two surfaces but small enough to avoid numerical issues. For instance, Zou *et al.* [114] developed 2D models to assess delamination in composite structures using a CZM. It was proposed a range of values

of $4.5\text{x}10^5 \leq K_n \leq 4.5\text{x}10^8$ N/mm^3 based on the interlaminar shear and tensile strengths. Camanho *et al.* [107] pioneered the development of 8-node de-cohesion elements for initiation and propagation of delamination modelling. During their element development, an investigation of K_n parameter was performed and results suggested that a value of $10^6 N/mm^3$ produces almost a similar result in different delamination modes without convergence problems.

Another solution to estimate K_n is proposed by Turon [115]. Here, the interface stiffness is determined based on the through-thickness stiffness of the composite laminates as well as on their thickness. This method is well accepted as it is a more mechanical approach to the stiffness within the interface. The equation developed by Turon is then:

$$K_n = \frac{\alpha E_{33}}{t} \tag{3.1}$$

where α is a parameter much larger than 1, E_{33} is the transversal sublaminate stiffness and t is the thickness of the sublaminate. Equation 3.1 has been used in different studies with good results [103, 116]. Although this approach is acceptable, it was decided to use the value proposed by Camanho to maintain simplicity.

3.2.2 Damage initiation criteria

Damage initiation refers to the stresses or strains at which damage starts to develop. Within $Abaqus^{TM}$ there are four different approaches [117]:

1. *Maximum nominal stress criterion*: Damage occurs when the maximum nominal stress ratio is equal to one. Equation 3.2 describes this criterion, where N_{max}, S_{max} and T_{max} are the nominal stresses in the normal (n), first shear (s) and second shear (t) direction respectively.

$$MAX\left\{\frac{\sigma_n}{N_{max}}, \frac{\sigma_s}{S_{max}}, \frac{\sigma_t}{T_{max}}\right\} = 1 \tag{3.2}$$

2. *Maximum nominal strain criterion*: Damage occurs when the maximum nominal strain ratio is equal to one. Equation 3.3 describes this criterion,

where ϵ_n^{max}, ϵ_s^{max} and ϵ_t^{max} are the nominal strains in the normal, first shear and second shear direction respectively.

$$MAX\left\{\frac{\epsilon_n}{\epsilon_n^{max}}, \frac{\epsilon_s}{\epsilon_s^{max}}, \frac{\epsilon_t}{\epsilon_t^{max}}\right\} = 1 \tag{3.3}$$

3. *Quadratic nominal stress criterion*: Damage occurs when a quadratic interaction function involving the nominal stress ratio is equal to one. This criterion is described in equation 3.4.

$$\left(\frac{\sigma_n}{N_{max}}\right)^2 + \left(\frac{\sigma_s}{S_{max}}\right)^2 + \left(\frac{\sigma_t}{T_{max}}\right)^2 = 1 \tag{3.4}$$

4. *Quadratic nominal strain criterion*: Damage occurs when a quadratic interaction function involving the nominal strain ratio is equal to one. This criterion is described in equation 3.5.

$$\left(\frac{\epsilon_n}{\epsilon_n^{max}}\right)^2 + \left(\frac{\epsilon_s}{\epsilon_s^{max}}\right)^2 + \left(\frac{\epsilon_t}{\epsilon_t^{max}}\right)^2 = 1 \tag{3.5}$$

The maximum nominal stress criterion was selected here to define the cohesive zone. As there is no experimental data for the aluminium-composite interface within a Type III cylinder, references were taken from studies having similar material and delamination conditions [51, 118]. Based on the literature, the initial values selected as input parameters were $N_{max} = 30MPa$ and $S_{max} = T_{max} = 60MPa$. However, these parameters will be varied as part of the subsequent investigation.

3.2.3 Damage evolution

To measure the damage evolution of the cohesive law (*i.e.* the softening region) in $Abaqus^{TM}$ it is necessary to define the parameter D, which describes the overall damage in the material and the combined effects of all other mechanisms. Based on this parameter, the damage evolution is described by the specification of either the effective displacement at complete failure δ_m^f, or the energy dissipated due to failure G_c [117]. If the evolution criterion is specified using the displacement, then

the effective displacement at failure δ_m^f relative to the effective displacement at damage initiation δ_m^0, is required. Once these values are specified, the parameter D is defined as:

$$D = \frac{\delta_m^f(\delta_m^{max} - \delta_m^0)}{\delta_m^{max}(\delta_m^f - \delta_m^0)} \tag{3.6}$$

Within this model, the damage was defined using the effective displacement at failure δ_m^f to have better control on the damage deterioration. By varying the δ_m^f parameter it is possible to draw the cohesive law and compute the area under the curve, which is the energy release rate G_c and, hence, approximate this value.

3.2.4 Defining a cohesive zone length

In order to ensure a correct prediction of delamination, it is important to confirm that there is a sufficient number of elements within the length of the cohesive zone. Different models have been proposed to approximate the cohesive zone length. Dugdale [98] developed a cohesive zone model in which it was assumed that the stress within this region is similar to the yield strength to the material. Barenblatt [119] developed a similar model for ideally brittle materials considering that the stress can vary within the plastic zone. Hillerborg [99] applied the work developed by Dugdale and Barenblatt and performed a finite element analysis on crack initiation and growth in concretes. In more recent studies, Hui *et al.* [120] estimated the cohesive length for elastic soft materials assuming the cohesive zone as a long thin strip. Falk *et al.* [121] defined the cohesive zone length within dynamic fracture events, considering the velocity of the crack growth. Although they have some differences, these models follow a similar form [115]:

$$l_{cz} = ME\frac{G_c}{(\sigma_{max})^2} \tag{3.7}$$

where E is the elastic modulus of the material, G_c is the energy release rate, σ_{max} is the maximum strength of the interface and the constant M varies with each model.

One of the most commonly used models is the one developed by Hillerborg,

where $M = 1$. Turon *et al.* [102] studied the mesh size effect on delamination simulation using Hillerborg's model, and developed a methodology to increase the mesh size within the cohesive zones for industrial applications. Harper and Hallet [104] studied the number of elements within the cohesive zone based on Turon's work but with a value of $M = 0.5$ and adding new variables to the cohesive length model definition: longitudinal modulus of the material, transverse modulus, shear modulus and plane stress or plane strain conditions. These properties are used to define an *equivalent elastic modulus* E' which is different for delamination in mode I and mode II, thus:

$$l_{cz,I} = E'_I \frac{G_{Ic}}{(\sigma_{I,max})^2} \tag{3.8}$$

$$l_{cz,II} = E'_{II} \frac{G_{IIc}}{(\sigma_{II,max})^2} \tag{3.9}$$

For E' in mode I mode II, it is necessary to calculate Voigt elastic constants which are defined by equations shown in Table 3.1.

Table 3.1: Voigt elastic constants

$b_{11} = 1/E_{11}$	$b_{12} = -\nu_{12}/E_{11}$	$b_{66} = 1/G_{12}$
$b_{22} = 1/E_{22}$	$b_{23} = -\nu_{23}/E_{22}$	$b_{55} = 1/G_{31}$
$b_{33} = 1/E_{33}$	$b_{31} = -\nu_{31}/E_{33}$	$b_{44} = 1/G_{23}$

E'_I and E'_{II} are then defined by equations 3.10 and 3.11.

$$\frac{1}{E'_1} = \sqrt{\frac{b_{11}b_{22}}{2}} \sqrt{\left(\frac{b_{33}}{b_{11}}\right)^{1/2} + \frac{2b_{31} + b_{55}}{2b_{11}}} \tag{3.10}$$

$$\frac{1}{E'_{II}} = \sqrt{b_{11}/2} \sqrt{(b_{11}b_{33})^{1/2} + (b_{31} + b_{55}/2)} \tag{3.11}$$

As part of the mode I and mode II delamination model definition, a comparison of the cohesive length obtained from the equations proposed by Turon and Harper has been performed and is presented in further sections.

3.2.5 Implicit and explicit finite element analysis

Generally, problems modelled through explicit and implicit methodologies are expressed through partial differential equations (PDEs). Both methodologies can be used to solve quasi-static and dynamic problems, although one method would be more suitable than the other depending on the problem. In all cases, the PDEs are solved within the FE environment using matrix equations. The resultant matrices can be linear or non-linear. Typically, sources of non-linearity in structural problems can be large deformations, large rotations and/or non-linear material properties. Thus, for linear problems the matrix equation to be solved is:

$$[K]\{x\} = \{f\} \tag{3.12}$$

where x is the displacement, $[K]$ is the global stiffness matrix and f are the nodal load vectors.

Similarly, for a non-linear quasi-static problem the matrix equation is:

$$[K(x)]\{x\} = \{f\} \tag{3.13}$$

Finally, for a dynamic problem the matrix equation is:

$$[M]\{x''\} + [C]\{x'\} + [K]\{x\} = \{f\} \tag{3.14}$$

where $[M]$ and $[C]$ are the mass and the damping matrices respectively.

Within an implicit analysis the displacements are solved via inversion of the stiffness matrix $[K]$. The solution is computed through various steps and the current step solution is based on the previous step. However, for large dynamic or non-linear problems, the inversion of the matrix [K] may result in convergence issues as well time-consuming. However, the main advantage of using implicit analysis is the large steps that can be used to compute the solution, because implicit methods are unconditionally stable.

In the other hand, in explicit methods the solution of the later state of the simulation is computed based on the current state. Although the implementation of these methods is more practical, one disadvantage is the small time steps

needed to perform the solution in order to comply with the Courant condition to maintain stability.

3.2.5.1 Explicit finite element modelling using cohesive elements

For this project, an explicit finite element solver has been selected due to the non-linearities resulting from large deformations, contact complexity and material properties. The use of an explicit model prevent the convergence issues more commonly encountered in implicit simulations. There are certain parameters to consider in order to assess that the solution obtained from the solver is closest to the real solution. For instance, it has been reported that the Kinetic Energy (KE) and Internal Energy (IE) must be properly controlled and, typically, it is required that the KE is less than 5% of the IE of the system [110, 117, 122].

Another parameter that needs to be properly controlled in an explicit solution is the time increment. In explicit analysis the required time increment depends mainly on the smallest element in the model. This results from consideration of the Courant condition:

$$\Delta t_{stable} \leq \frac{L_e}{c_m} \tag{3.15}$$

Here, L_e is the smallest element length and c_m is the wave speed of the material, which is defined in equation 3.16, where E_m and ρ_m are the bulk stiffness and density of the interface material, respectively [123].

$$c_m = \sqrt{\frac{E_m}{\rho_m}} \tag{3.16}$$

Equation 3.15 and 3.16 show that having a large element size within the whole model is beneficial for reducing computational cost, however this becomes difficult using CZM due to their small thickness. For industrial applications (such as the one developed in this project), this can be a disadvantage giving the large number of degrees of freedom used on their models. Thus, two different approaches can be followed to reduce the computational time: mass scaling and load rate change. The former refers to scaling artificially the density of the critical elements (*i.e.* the smallest elements) to increase the stable time step. This

method is widely used to develop static simulations using explicit formulations, for instance, Pinho *et al.* [124] and Mollon *et al.* [125] suggest using mass scaling to reduce computational time providing that the KE $\leq$ 5% IE relation is maintained. Similarly, Gonzalez *et al.* [110] reported a scaling value of approximately 1.0*e*3 to simulate transverse crack tension tests using CZM in an explicit code, and their model showed good correlation to experimental data.

Furthermore, modifying the loading speed can reduce the computational time by modifying the duration of the event. Mollon *et al.* [125] performed a comparison between different fracture mechanics modelling techniques using implicit and explicit schemes. Their results indicated that a range of load rate values from 0.5 mm/s to 200 mm/s could be used with no significant change to the results, which agrees with other publications [110, 117, 124]. The values selected to develop the model in this project are based on the relations and equations described in this section.

3.3 Application of CZM on quasi-static simulations using an explicit scheme

3.3.1 Mode I & Mode II delamination models

In this section, two standard DCB and ENF test models are developed to investigate the effects of using an explicit scheme for a quasi-static simulation using 3D cohesive elements in *Abaqus/Explicit*, and to evaluate the robustness of the method for the modelling of Type III cylinders. Mass scaling, mesh size and direct comparison to an implicit solver are assessed in this section. Additionally, these models are used to define the parameters for mode I and mode II delamination in an explicit scheme. This study is compared to other similar work reported in the literature [102, 116, 126], with the geometry used to develop the models being, based on that used by Harper and Hallet [104] (see Figure 3.3). The material used was HTA6376/C with a ply layout of $[0_{12}//(\pm 5/0_4)_s]$. Material properties are presented in Table 3.2.

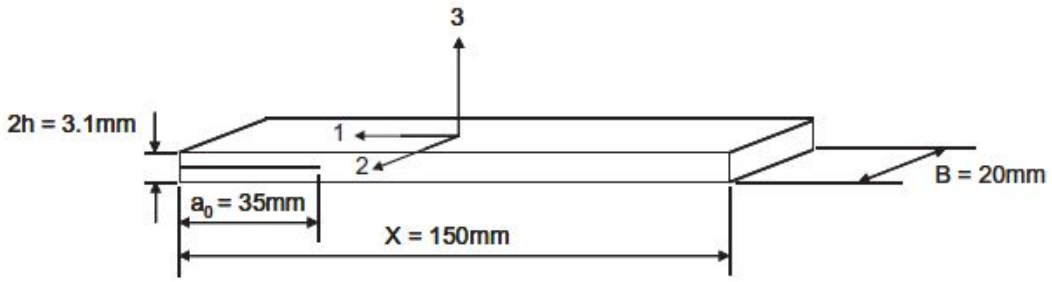

Figure 3.3: DCB and ENF base geometry

Table 3.2: HTA6376/C material properties [104]

E_{11}(MPa)	140,000
$E_{22} = E_{33}$(MPa)	10,500
$G_{12} = G_{13}$(MPa)	5,250
G_{23}(MPa)	3480
$\nu_{12} = \nu_{13}$	0.3
ν_{23}	0.51

The main objective of these models is to define the cohesive element parameters within the explicit scheme, thus, to maintain simplicity, continuum shell elements (SC8R) were selected to model the composite layers of the test specimens. Continuum shell elements have the advantages of being computationally cheaper than solid elements and allow an explicit modelling of the ply thickness, with negligible differences in results [117]. Regarding the cohesive zone, an 8-node three-dimensional element (COH3D8) has been used with an initial thickness of 0.01 mm. The interface properties are defined in Table 3.3. The value of $K_I = K_{II} = 10^6 N/mm^3$ was selected as is commonly used for this type of analysis and it agrees to what is reported by some authors ([110, 114, 127]) and is not higher than the value calculated using the equation proposed by Turon [102]. The energy release rate and maximum strength values are comparable to similar studies simulating mode I and mode II delamination [100, 127–129].

To define the cohesive zone length the methods proposed by Turon [102] and Harper [104] were compared using equations 3.7 through 3.11, with $M = 1$ and $M = 0.5$ respectively. The results of each method can be observed in

Table 3.3: Interface properties for COH3D8 elements [104]

G_{IC}(N/mm)	0.3
G_{IIC}(N/mm)	0.6
$\sigma_{I,max}$(MPa)	30
$\sigma_{II,max}$(MPa)	60
$K_I(N/mm^3)$	10^6
$K_{II}(N/mm^3)$	10^6

Table 3.4. In this context, both authors recommend a total of three elements within the cohesive length, thus the final length of the element L_e with each method is described as well. It can be noted that by using an element length of approximately 0.5 there will be sufficient elements within the cohesive region.

Table 3.4: Final cohesive zone length using methodologies proposed by different authors

	Turon	**Harper&Hallet**
$L_{cz,I}$(mm)	3.03	2.46
$L_{cz,II}$(mm)	1.75	5.31
$L_{e,I}$(mm)	1.01	0.82
$L_{e,II}$(mm)	0.58	1.77

A summary of the main characteristics of the DCB and the ENF models can be observed in Figure 3.4a and 3.4b respectively. In both tests the loading is displacement controlled. For the DCB, a 5-mm displacement in the normal direction was applied at the end of the beam (Figure 3.4a). On the other hand, a 4-mm displacement was applied in the centre of the ENF coupon(Figure 3.4b). Finally, an initial crack length $a_0 = 35$ mm was used for both models.

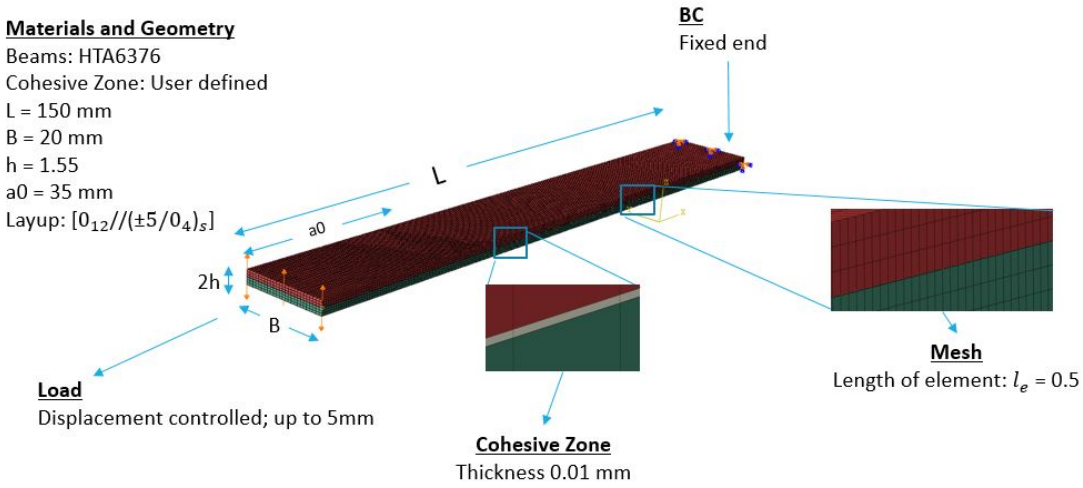

(a) DCB FE model

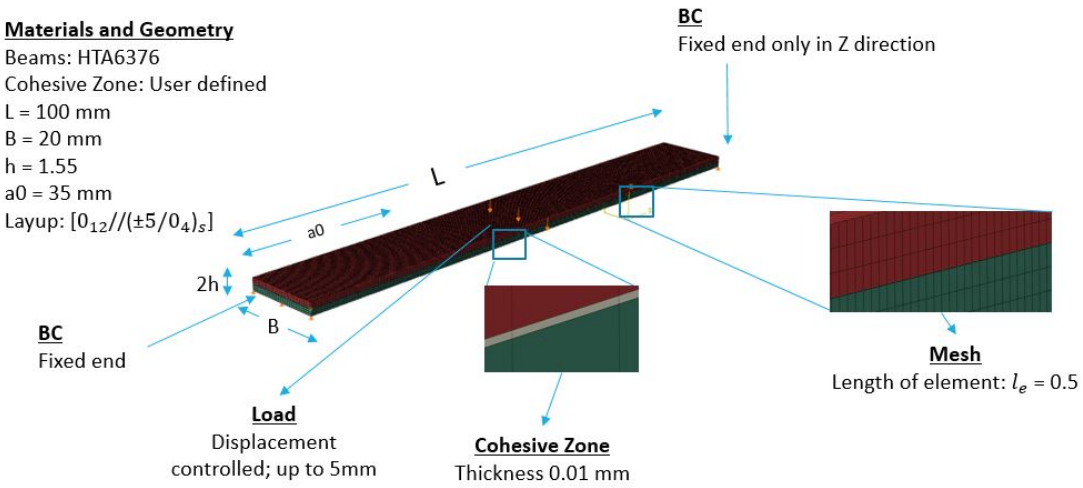

(b) ENF FE model

Figure 3.4: Final FE models

3.3.2 Mode I & Mode II delamination models results

3.3.2.1 Mode I delamination: DCB model

This section describes the results of the DCB model described in Section 3.3. The final delamination is illustrated in Figure 3.5, where a_0 is the initial crack and a_1 is the final crack length. It is noticed that the final crack front is not a simple straight line, which can be an edge effect arising from an anticlastic bending. This curved delamination front is consistent with what has reported in the literature [116, 130]. Crisfield and Davies [100] developed similar 3D models in which they observed a similar crack tunnelling behaviour. Furthermore, they discussed the development of the softening "process zone" within the cohesive zone length, which is the red-coloured region in Figure 3.5. Consistent with the recommendations of Crisfield and Davies, there are at least two elements in the softening process zone [100], see Figure 3.6.

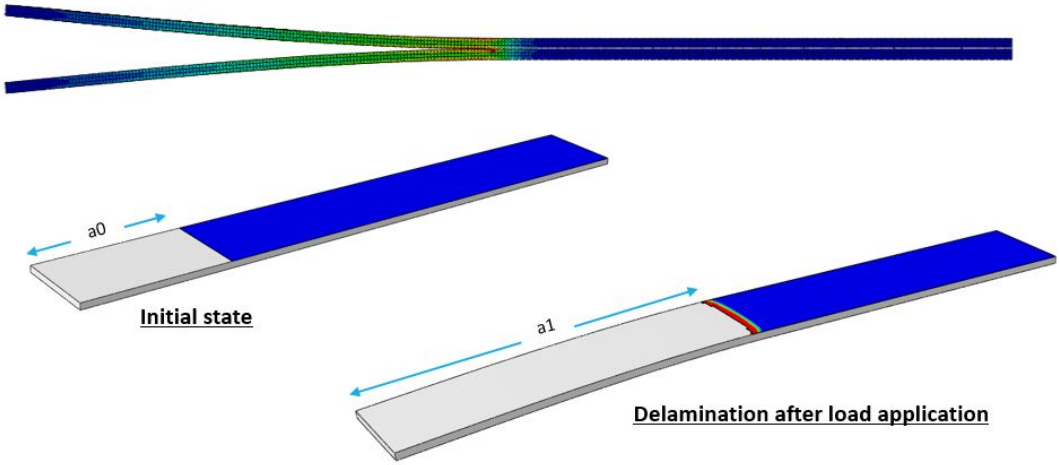

Figure 3.5: Final crack length in DCB specimen after load application

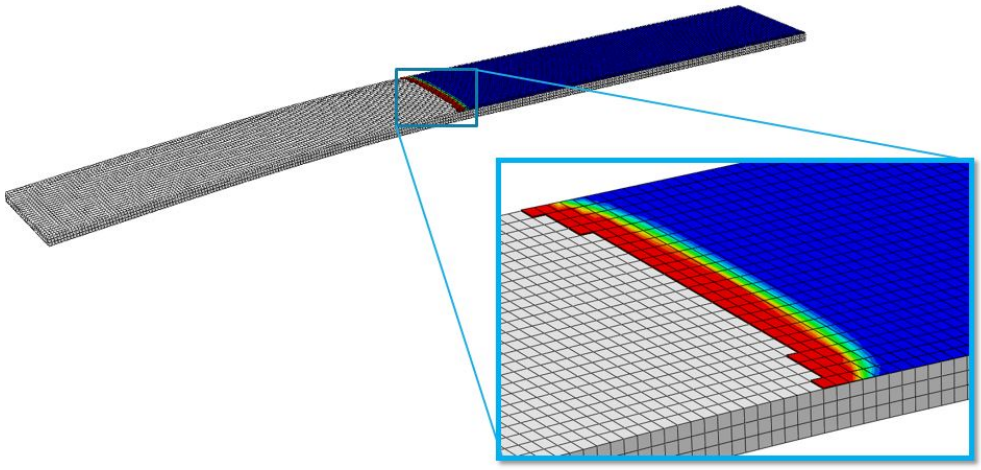

Figure 3.6: number of elements in the softening process zone

The theoretical response of the DCB was obtained using equations 3.17 and 3.18 [33] from the Classical Beam Theory (CBT).

$$\delta_I = \frac{2Pa^3}{3E_{11}I} \tag{3.17}$$

$$G_{Ic} = \frac{P^2a^2}{BE_{11}I} \tag{3.18}$$

where δ_I is the vertical separation of the beams, P is the point load applied to the free end of each beam, a is the initial crack length, E_{11} is the Young's modulus, B is the specimen width and I is the second moment of inertia of each beam. Figure 3.7 shows a comparison between the theoretical solution and the response obtained with the current FE model. Good agreement with CBT is seen in the initial stiffness region. The non-linearity seen very close to the peak of the FE response is attributable to $Abaqus^{TM}$ tool called the *butterworth filter*, which is used to filter noisy data, especially from explicit analyses [110]. Crack propagation within the FE response has some divergence from the CBT prediction, such as the anomalous *rounding* of the load displacement plot at the onset of crack propagation. However, the FE model showed G_{Ic} that is in reasonable agreement with the nominal value (see Table 3.5). The estimation of G_{Ic} was performed using equation 3.18.

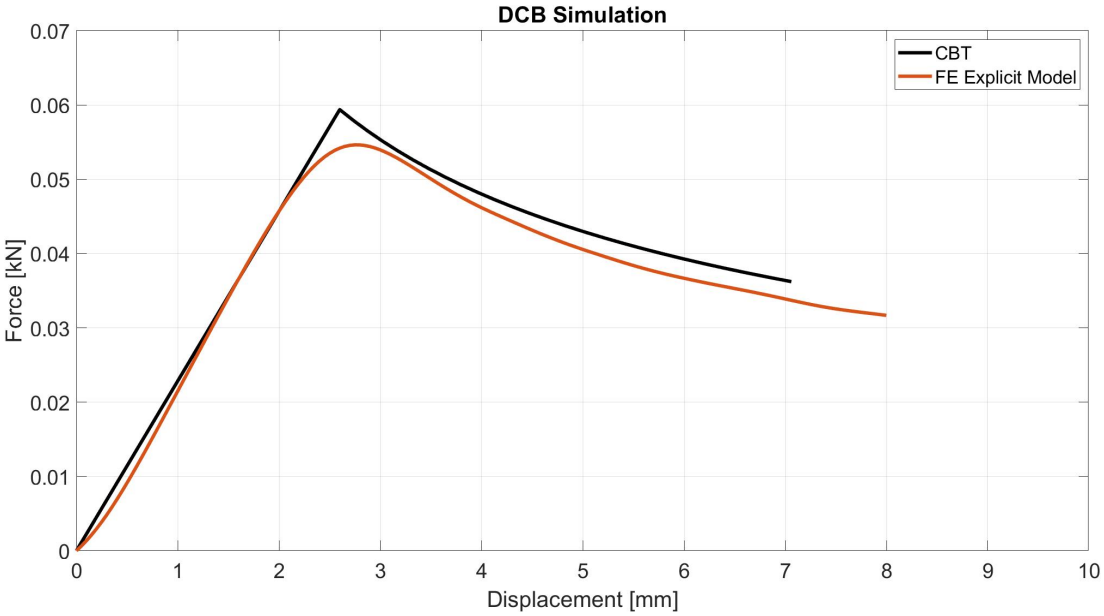

Figure 3.7: Mode I delamination force-displacement curve

Table 3.5: Energy release rate for mode I delamination

Displacement[mm]	Load[kN]	a[mm]	$G_{Ic}\frac{J}{m^2}$	% Error
2.9	54.4	38	308	2.5%
3.0	53.9	39.5	310	3.2%
3.2	52.6	41	310	3.2%
3.5	50.1	42.5	305	1.6%
3.7	48.4	44	303	1.1%

The mass scaling parameter was varied to evaluate its effect on the force-displacement behaviour. In *Abaqus*^{TM} the simplest way to scale the mass of the model is by a user-defined factor. Here, a factor of 50 was defined and compared to the model with a factor of 1 (*i.e.* no mass scaling). These values agreed with those presented by Gonzalez [110]. The results are presented in Figure 3.8.

By introducing the mass scaling factor, computational time can be saved, which is important, particularly for the larger models which will be required later in the project. Both the DCB and the ENF models were run on a local computer with an Intel(R) Xeon(R)CPU E5-1650 processor and 64 GB of RAM. Four CPUs were used to perform the analysis, and the computer was not used with

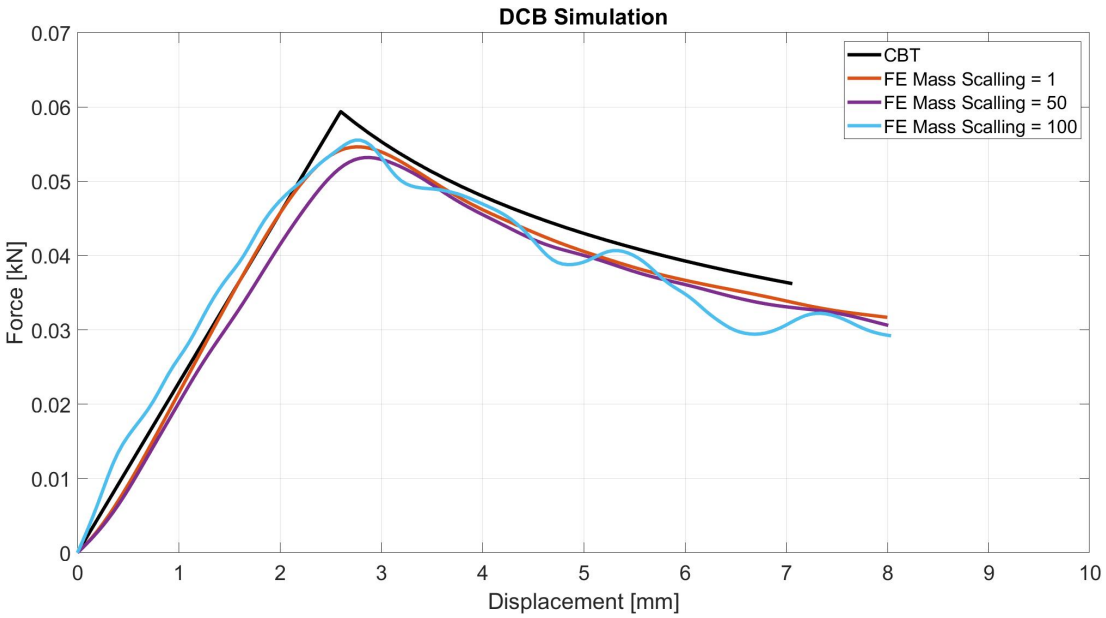

Figure 3.8: Mode I delamination force-displacement curve with different mass scaling factors

other applications during the running time. The difference in computational time spent on each analysis is shown in Table 3.6. Results show that by using a mass scaling factor of 50 and 100, the computational time can be significantly reduced for DCB test. However, for the 100 mass scaling factor, there is a significant increase in noise which affects the prediction of the initial elastic response and the later delamination behaviour.

A similar assessment for mode II is presented in the next section.

Table 3.6: Computational time using different mass scaling factors

Model	Start Time	End Time	Total
Mass scaling factor = 1	09:13:05	15:29:31	06:16:26
Mass scaling factor = 50	17:37:19	18:18:24	00:41:05
Mass scaling factor = 100	18:34:20	19:01:36	00:27:16

Although the mesh size has been calculated using different approaches (see section 3.2.4), additional simulations with different mesh sizes were performed and the resultant f-d curves are presented in Figure 3.9. It is observed that

there is no significant difference in modifying the mesh size from 0.5 to 0.25 mm. Furthermore, both mesh sizes ensure having at least 5 elements within the cohesive region. On the other hand, using a larger mesh size of 1.0 mm results in a higher difference in comparison to the experimental curve, specially in the elastic region. It is observed that a larger element size results in having less finite elements in the cohesive region, hence modifying the delamination performance of the plate. Thus, the results suggest that a mesh size of 0.5 mm is adequate for this analysis and it is still in accordance to what was calculate in previous section using the cohesive length equations.

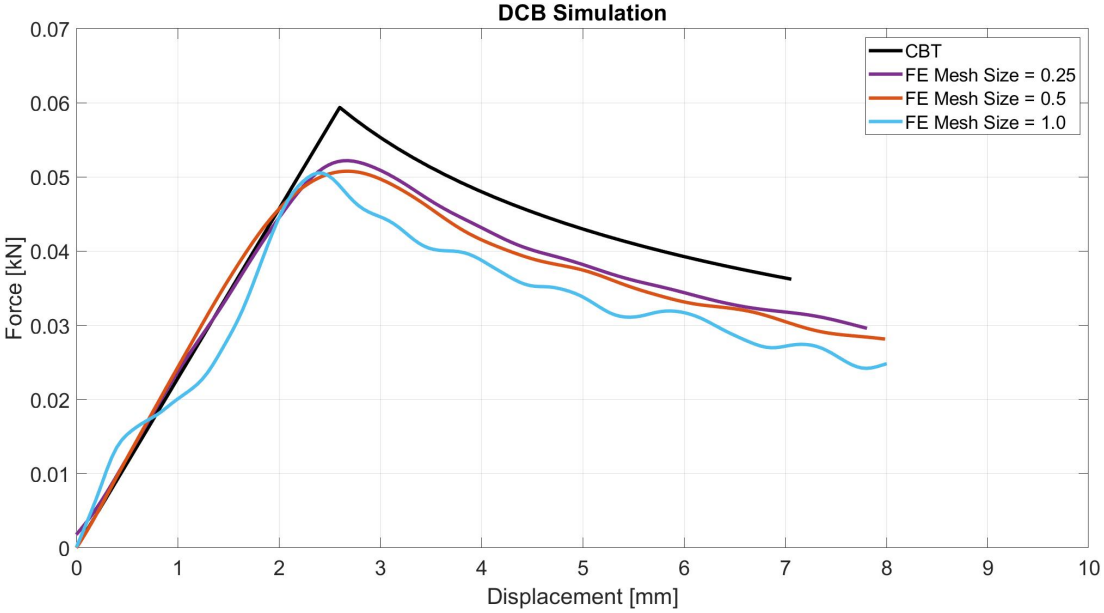

Figure 3.9: Mode I delamination force-displacement curve with different mesh sizes

Finally, to assess the quasi-static behaviour, the model has been compared to an analogous model developed within an implicit scheme. Figure 3.10 shows the comparison between the implicit and the explicit results. The CBT result is shown as well for reference. Similar to the CBT case, the initial elastic response correlates well in both models, however it would appear that the implicit scheme shows better agreement during the propagation region. Despite these differences, the result of the explicit model suggests a quasi-static behaviour. Moreover, to assess an adequate behaviour of the model, the IE and the KE have been plotted

(see Figure 3.11) and it was confirmed that the KE $\leq$ 5% IE relation is attained, even with a scaling factor of 50, which presumably would represent a worst case scenario [123].

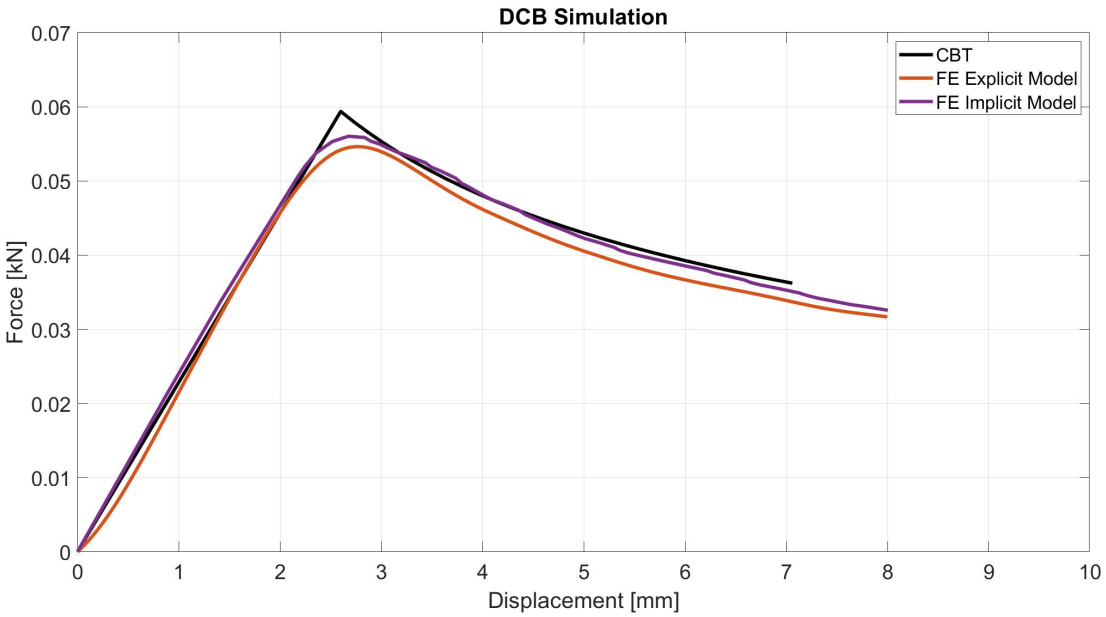

Figure 3.10: Mode I delamination force-displacement curve under different simulation schemes

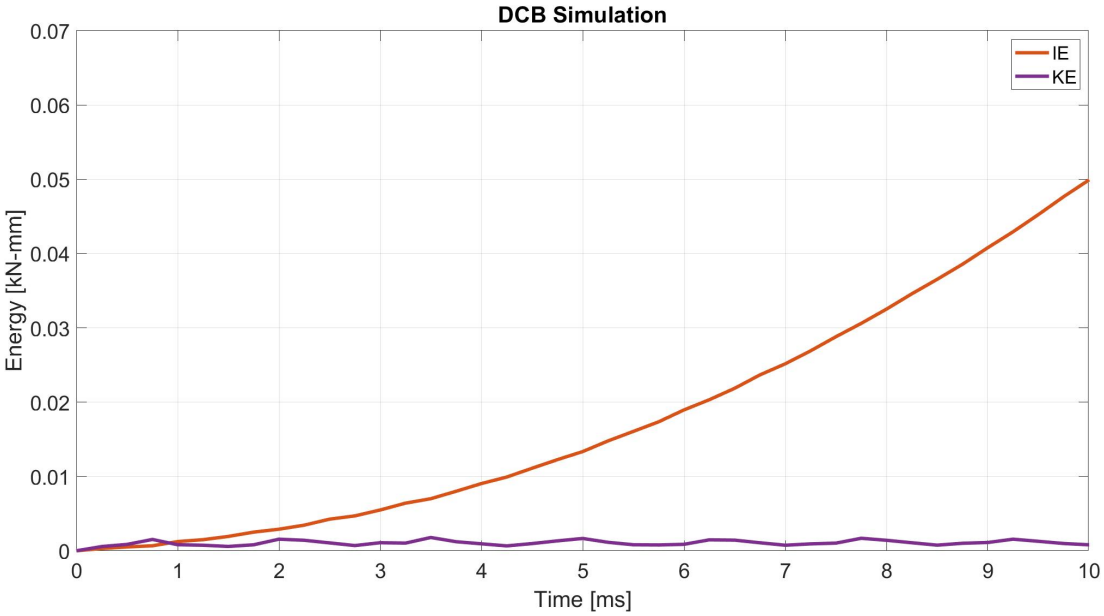

Figure 3.11: DCB model Internal Energy (IE) and Kinetic Energy (KE) comparison

3.3.2.2 Mode II delamination: ENF model

A process similar to that describe in the previous section has been followed to test the mode II delamination simulation capability based on a ENF test model. The final deformation after the load application is presented in Figure 3.12, in which the "edge effect" observed in mode I delamination can be observed again.

Correspondingly, CBT for mode II analysis was used to compare model results against theoretical data. As such, δ_{II} and G_{IIc} where computed as follows:

$$\delta_{II} = \frac{3Pa^3 + 2PL^3}{96E_{11}I} \tag{3.19}$$

$$G_{IIc} = \frac{3P^2a^2}{64BE_{11}I} \tag{3.20}$$

where P is the applied load, a is the crack length, E is the through thickness stiffness, B is the specimen width and I is the second moment of area. The comparison of load-displacement behaviour between the CBT and the FE model for mode II delamination is shown in Figure 3.13. Despite minor differences in the maximum load calculation, the initial behaviour exhibits good correlation to

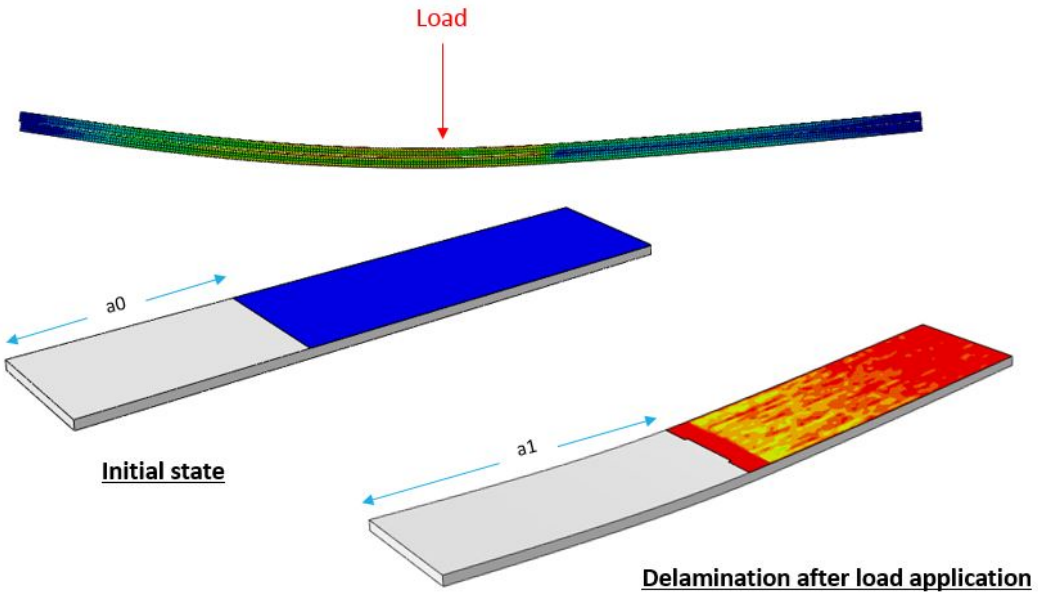

Figure 3.12: Final crack length in ENF specimen after load application

the CBT curve. This curve is consistent with the work reported by Harper and Hallet [104], although their models were developed using an implicit scheme. Furthermore, the behaviour agrees as well with other ENF models developed with different schemes and using different type of elements to represent the associated composites [115, 118, 127]. The energy release rate for mode II computed by the model at different crack lengths is presented in Table 3.7.

Table 3.7: Energy release rate for mode II delamination

Displacement[mm]	Load[kN]	a[mm]	$G_{IIc}\frac{J}{m^2}$	% Error
1.99	373	40	577	3.7%
2.11	331	44.5	561	6.5%
2.19	315	47	570	4.9%
2.25	311	48	578	6.5%

Two different techniques were adopted to reduce computational time: mass scaling and load rate changing. The mass scaling method was investigated using a similar approach as in the DCB case. Figure 3.14 shows a comparison of the simulation developed using three different mass scaling factors. The curve indi-

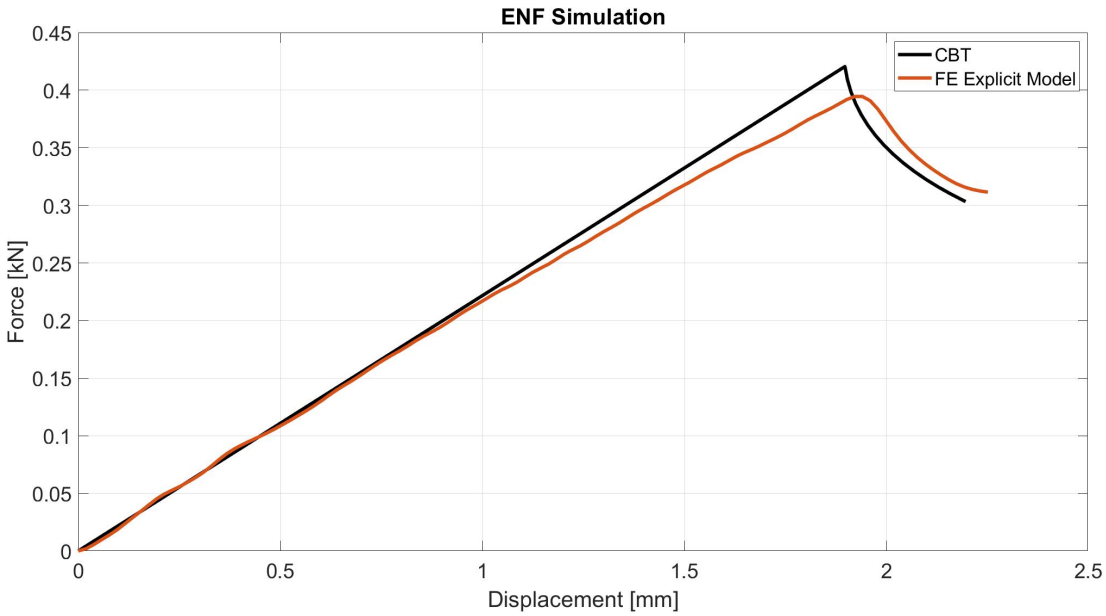

Figure 3.13: ENF Mode II delamination force-displacement curve

cates that the general behaviour is well predicted using a scaling factor of 1 and 50. However, when using a value of 100 the f-d curve shows noticeable differences on the result. The predicted elastic response shows more noise than in the two lowest levels of mass scaling, and the peak force values is being underpredicted. This results indicates the significant influence that the mass scaling factor can have over the final results, specially for Mode II delamination. This effect was expected considering that the mass scaling introduces noise and instability to the simulation as non-realistic mass is added to the simulation [123]. As performed in the DCB model, internal and kinetic energies were monitored. In this case, the energies presented in Figure 3.15 belong to the model with scaling factor of 100. It is can be observed that, although there is some noticeable noise within the KE plot, the KE $\leq$ 5% IE is maintained. This is contrasting to what can be observed from the same model in Figure 3.14 in which the correlation to the theoretical result is less compared to the other scaling factor models. Therefore although the KE $\leq$ 5% IE relation is an accepted parameter in literature, it is suggested to test other parameters to ensure that the results are reliable.

A further technique to reduce the computational time involves changing the load rate. This is controlled in $Abaqus^{TM}$ by defining the time length of

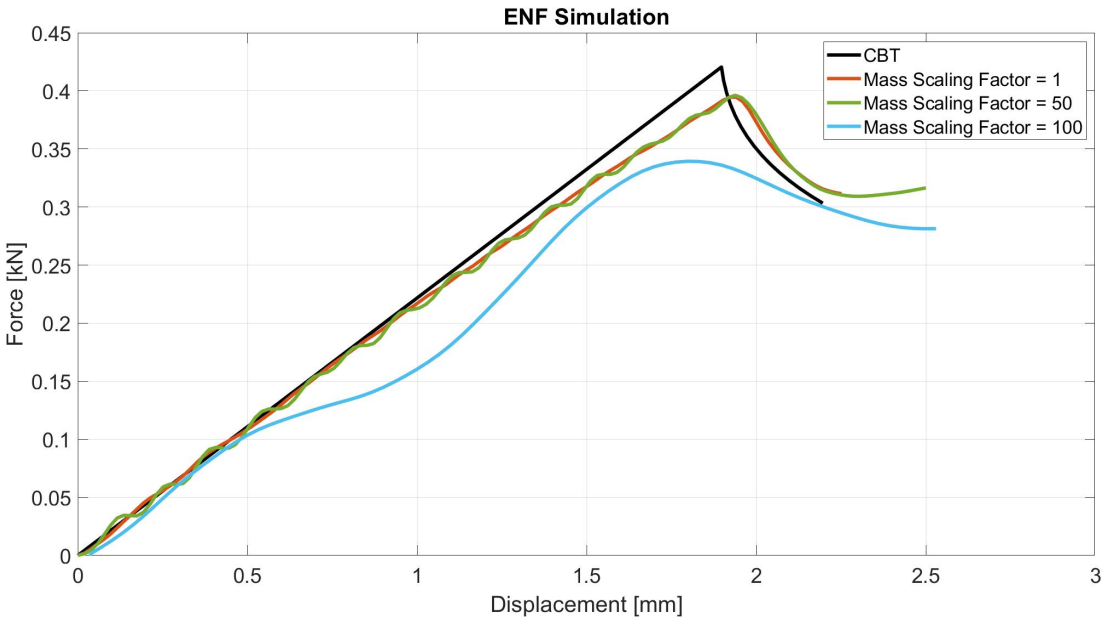

Figure 3.14: Mode II delamination force-displacement curve with different mass scaling factors

the simulation. The ENF simulation was run at 300 ms initially and then at 30 ms and 500 ms to investigate the effect on the force-displacement behaviour. Each run time corresponds to a velocity of 13.3 mm/s, 133 mm/s and 8 mm/s respectively, which are values within the parameters suggested by Mollon [125]. The results are presented in Figure 3.16, from which it can be concluded that using a 30 ms run time is not sufficient to produce a quasi-static solution. Here, the event is occurring at a speed at which the model is not able to compute the delamination and, as a consequence, the damage appears to occur faster than it should. Furthermore, results indicate that there is no significant effect on increasing the simulation time from 300 ms to 500 ms as the f-d behaviour shows negligible difference.

Following a similar procedure as that in the DCB model, the ENF explicit model was compared to the analogous implicit version. Figure 3.17 shows the comparison of both schemes to the CBT theoretical solution. No significant difference is observed between each model in relation to the theoretical response of the specimen. Thus, it can be concluded that the parameters selected to perform this simulation using an explicit scheme provide a sufficient approximation to the

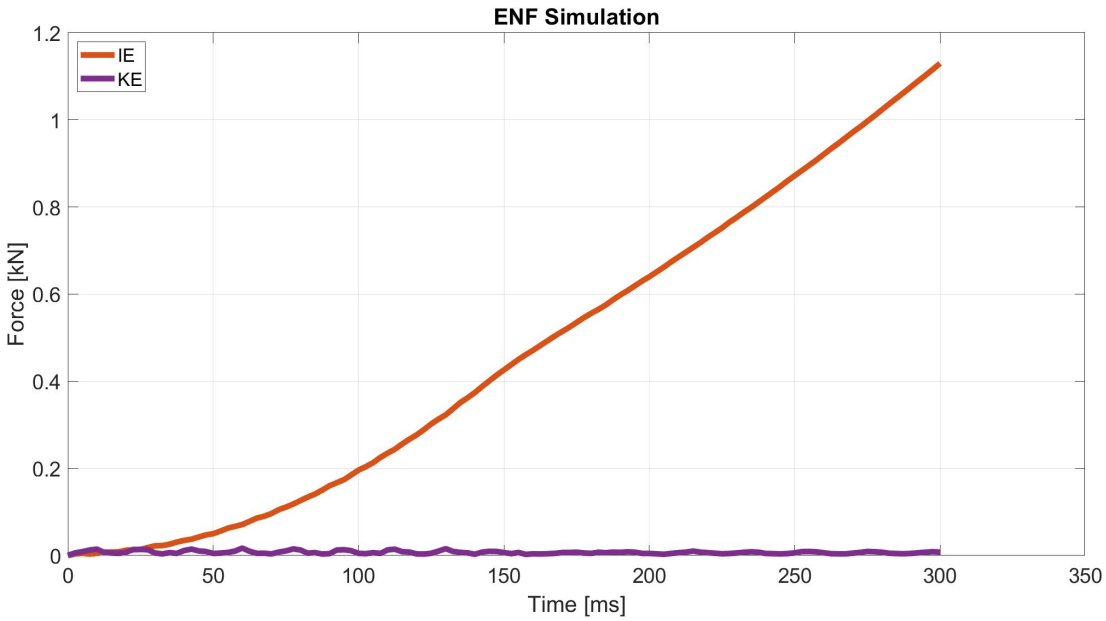

Figure 3.15: ENF model Internal Energy (IE) and Kinetic Energy (KE) comparison

quasi-static response.

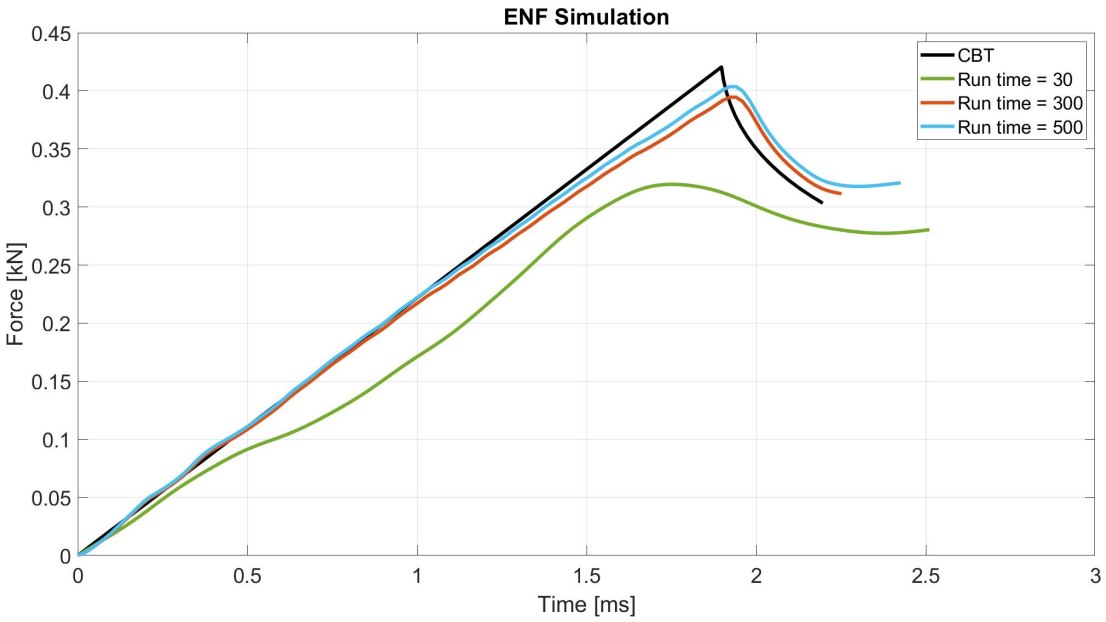

Figure 3.16: Mode II delamination force-displacement curve at different load rates

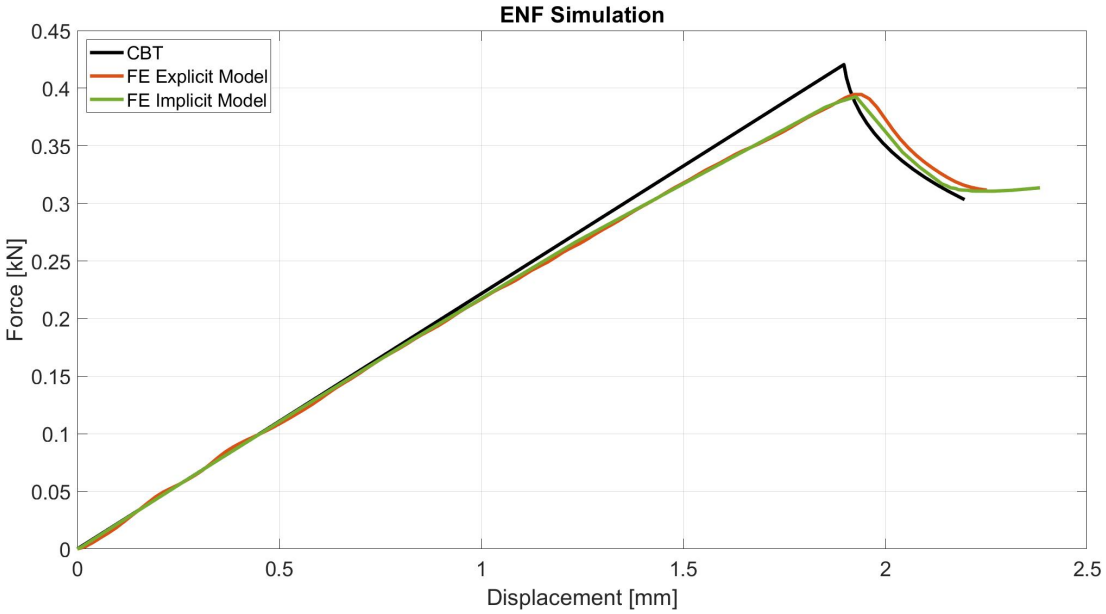

Figure 3.17: Mode II delamination force-displacement curve under different simulation schemes

3.4 Summary and conclusions

This chapter presented the general methods to be used for experiments and simulations throughout the project. Firstly, a quick summary of previous experiments performed on Type III cylinders has been provided. One of the main observations was the damage propagation and development of residual metal deformation resulting from a quasi-static indentation point load. Thus, the parameters used to develop the experiments on these cylinders constitute the boundary conditions to be used on the FE model. Moreover, to introduce some of the experimental activities to be developed in this project, a brief description on DIC was also presented. This imaging technique will be used in this project to perform strain measurements on the ring specimens described in further chapters.

Regarding the modelling, the use of cohesive elements was presented and the main parameters to define the were described in this chapter. The main characteristic to consider when modelling interfaces using cohesive elements are the damage initiation and damage evolution, which are defined based on the interface strength and interface fracture toughness within a traction-separation law. Furthermore, the definition of the cohesive zone length was described and different approaches to define it where compared to select the option that best fits the characteristics of the current project.

Finally, standard DCB and ENF tests where developed to investigate the parameters needed to perform a quasi-static simulation using an explicit solver. Force-displacement curves on comparing FE results to CBT results were presented. Moreover, the explicit glsfe results were compared to results obtained with an implicit solver. Results indicated that a mass scaling factor of 50 along with a simulation time of 300 ms on *Abaqus/Explicit* have minor differences to a simulation performed with an implicit solver (*Abaqus/Standard*). Finally, the explicit simulation was also validated by analysing the energies developed throughout the simulation. IE and KE were plotted and the results showed that both models comply with the relation KE $\leq$ 5% IE, which indicates a stable explicit simulation. Hence, it was concluded that, with the parameters selected, is possible to use cohesive elements with an explicit solver to simulate a quasi-static mechanistic event.

Chapter 4

Model-experiment comparison for transverse loading of metal-composite ring specimen

4.1 Introduction

In this chapter, a numerical model of a hybrid metal-composite ring is developed and presented. The aim of this model is to estimate CFRP and metal-composite interface properties to predict delamination and the residual indentation in the metal layer. Previous modelling investigations on hybrid pressure vessels use an ideal metal-composite bond or take reference properties from experimental tests that have been perform on plates [78, 89]. However, given the geometry and the residual stresses contained on a Type III cylinder, these properties have not been assumed. This FE model contains cohesive elements that are used to estimate interface fracture toughness and strength of the metal-composite bond. Estimated properties will be then referenced to develop a full Type III cylinder FE model described in further chapters.

4.2 Methodology

4.2.1 Ring specimen FE model

Aluminium Al-6061 was used to model the metal section of the ring and the relevant properties can be found in Table 4.1. A ply-level modelling approach was selected to model the composite wrap, having a total of six plies with hoop and helical layers modelled individually. Details regarding fibre orientations on the model are discussed in further sections. Material properties were calculated based on Toray T700s fibres and EPO912 resin using a rules of mixtures [3]. Carbon fibre wrap ply properties can be found on Table 4.2. For this model, delamination within the CFRP and the metal-composite interfaces are the damage mechanisms investigated, that is, no fibre or matrix fracture are considered.

Table 4.1: Material properties of the 6061-T6 Aluminium

Young's modulus (E)	Ultimate tensile stress (σ_{uts})	Yield stress (σ_y)	Poisson's (ν)
69 GPa	310 MPa	276 MPa	0.3

Table 4.2: Material properties of the T700s plies

E_{11}	$E_{22} = E_{33}$	G_{12}	ν_{12}
139 GPa	6.63 GPa	3.78 GPa	0.28

The FE model was developed in the commercial software $AbaqusCAE^{TM}$. Based on the known structure of the physical specimen, the ring is divided into seven different layers, one corresponds to the metal ring of the structure and the other six corresponding to the CFRP layers. The latter contains hoop (0°) and helical (71°) layers, with a layup of $[0°/\pm 71°]_3$ (Figure 4.1). Each layer consist of solid (C3D8R) elements with one element through the thickness, except for the metal ring which has three elements through its thickness. The indenter and the support used to enforce the delamination were modelled using rigid (R3D4) elements. The aluminium was modelled as an elastic-perfectly plastic material,

with the properties given in Table 4.1. The composite was modelled as being elastic, other than allowing for the possibility of delamination, as described below.

To model the metal-composite interface as well as delamination occurring within the CFRP layers, cohesive elements were used. These finite elements are typically used in delamination problems and they are defined by a traction separation law [102]. In between each section of the ring model, 0.01 mm thick cohesive elements (COH3D8) are used, except for the section between the $\pm 19°$ helical layers which are joined together using a tied contact for simplicity, as these are observed not to delaminate. A total of six cohesive element interfaces are embedded in this model and one contains unique properties for the metal-composite interface 4.1. The rest of the interfaces contain the same properties to predict the delamination within the CFRP layers. Contact was defined in-between layers to ensure no material penetration occur in case of cohesive element deletion (delamination). Geometric and meshing details of the FE ring model are shown in Figure 4.1.

Cohesive element properties were defined through parametric investigation of the parameters that define the traction-separation, *i.e.* interface strength (τ^0) and interface toughness (G_c) in modes I and II. These parameters define the traction separation law which determines the cohesive layer behaviour and ultimate interface delamination. Considering that the metal-composite interface is of high interest due to its possible effect on the residual dent development, three values where proposed for each cohesive element parameter *i.e.* three traction-separation laws for each mode. For the composite interface properties, only one interface strength value and two interface toughness were proposed (*i.e.* two different traction-separation laws). The values proposed here are based on typical values found on literature for metal-composite and CFRP interfaces in plates [57, 103]. The purpose is to identify the values that produces a result that reasonably approximate the overall structure's behaviour compared to the experimental data.

To overcome convergence difficulties it was decided to use the Abaqus/Explicit solver [110]. The solution is divided into two different steps: loading and unloading. The former refers to the compression of the ring specimen, and the latter refers to load release. Load is applied through 20-mm controlled displacement of

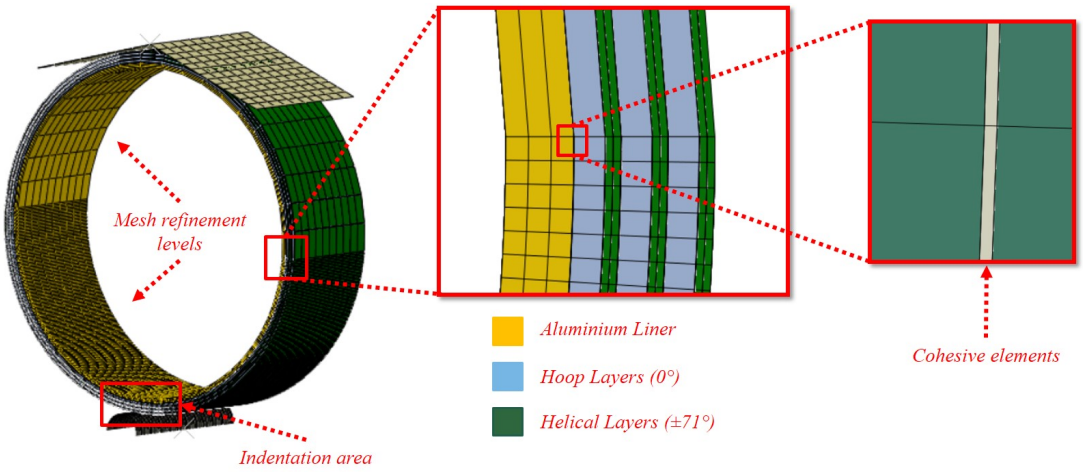

Figure 4.1: FE ring model description

Table 4.3: Interface properties for cohesive elements

τ_{11}^0 (MPa)	$\tau_{22}^0 = \tau_{33}^0$ (MPa)	G_{Ic} (J/m^2)	$G_{IIc} = G_{IIIc}$ (J/m^2)
Metal-composite interface properties			
10, 20, 30	20, 40, 60,	150, 750, 1500	300, 1500, 3000
Composite interface properties			
15	30	375, 750	750, 1500

the upper rigid support. Load rate application is 0.04 m/s and a mass scaling factor of $1e3$ is used [110]. There are two mesh refinement levels on the structure, upper and lower (Figure 4.1). The upper half of the ring has a mesh size of 10 mm and it was modelled to add an elastic stiffness response, thus, no cohesive elements were included in this region of the model and the plies are joined using a tied contact. The lower half of the ring has a mesh size of 0.6 mm, which ensures at least five elements are used to model the cohesive region [115].

4.2.2 Ring specimen indentation test

An analogous experimental test to the FE model was performed. Ring specimens were manufactured by cutting a 9-litre COPV into 50 mm length slices. Total ring diameter was 159 mm, with a 2.2 mm liner thickness and 4.6 mm CFRP

thickness (hoop and helical $\pm 71°$ layers). The specimens were loaded in compression using an electro-mechanical testing machine, a v-shaped loading support and a longitudinal bar ($r = 8mm$) that induced indentation across the specimen length, this way the delamination should remain approximately constant through the length of the specimen, *i.e.* become an essentially 2D problem (Figure 4.2). Loading rate is 2 mm/min. The loading procedure is similar to the quasi-static indentation test presented in [2] and analogous to the FE model, *i.e.*, load is applied using a loading and an unloading step.

DIC was used to measure strains that can be compared to the FE model. Furthermore, this tool was also used to indicate the onset of damage that may not be apparent by direct imaging. Two LaVision E-lite cameras in stereo configuration were used to record images [131], and each camera was equipped with a 105 mm lens. The region on which the cameras are focused, also known as Field of View (FoV), was defined based on the area where the maximum delamination and metal residual indentation are expected (Figure 4.2). The speckle pattern was defined with a white matte paint as a background. Then, black was applied using a spray at a 1 m distance from the specimen. As suggested in literature [131], each speckle covered 3-5 pixels. The final speckle pattern is showed in Figure 4.2.

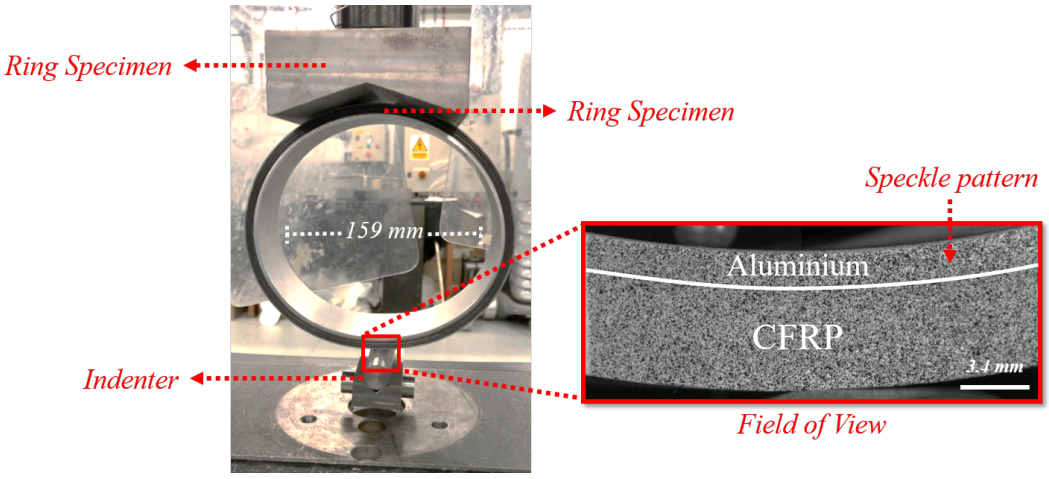

Figure 4.2: Ring specimen test setup

4.3 Results

4.3.1 Experimental results

Data collected from the experiment includes force-displacement (F-d) curves, delamination images and strain fields. Figure 4.3 shows the F-d curves response of the ring specimen which exhibits several load drops during loading (points A, B, C). Similarly, Figure 4.3 shows the nominal strain (ϵ^*_{xy}) fields obtained from DIC used to track delamination (Figure 4.3a, 4.3b and 4.3c). A yellow dotted line was added as a reference to differentiate between the aluminium and the CFRP materials. When comparing the strain values to the F-d curve, it was confirmed that the load drops correspond to significant delamination events within the ring. Points A and B, for instance, relate to delamination within the CFRP layers, whilst point C corresponds to metal-composite delamination. The curve indicates that after metal-composite delamination there is a marked loss in overall stiffness, *c.f.* the onset of composite delamination. Point D is the maximum displacement application at the end of the compression step, at which ϵ_{xx} strains were measured on the aluminium ring using DIC (Figure 4.3d). This data can be directly compared to that obtained from the FE model. Point E shows the end of the load release step and the residual indentation on the aluminium ring. At this point it was difficult to obtain an acceptable strain measurement due to the level of damage induced in the ring, particularly in the composite layer (Figure 4.3e).

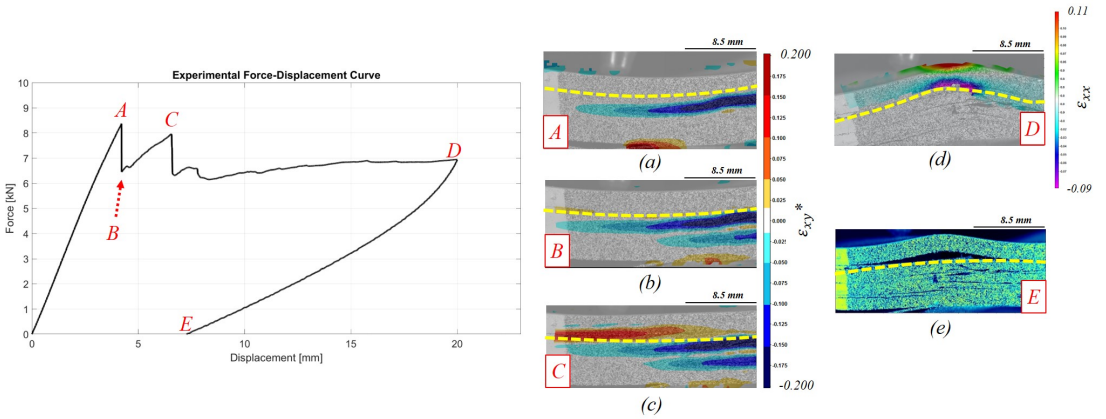

Figure 4.3: Experimental F-d curve; a) First major CFRP delamination; b) Second major CFRP delamination; c) Metal-composite interface delamination; d) Maximum compressive load application; e) Residual indentation (load removal)

4.3.2 Model calibration and validation

4.3.2.1 Force-displacement behaviour

F-d curves similar to those obtained from the experimental tests were obtained from the FE model for comparison. The virtual curves exhibit oscillations as a result of the dynamic solution used for the analysis. Figure 4.4 shows a comparison between the experimental curve and a result from the FE model. Four main characteristics are observed in the virtual result: an initial elastic response, a first and a second noticeable load drops (points X and Y) and an unloading response (point Z). The initial response exhibits good correlation with the experimental curve. From the model delamination results (Figure 4.4a), it was noticed that the first load drop (point X) is related to delamination occurring within the CFRP plies. After this damage, the reaction force remains stable until a second load drop occurs (point Y) which is a consequence of metal-composite delamination and yield of the metal layer (Figure 4.4b). Similar to the experimental curve, the FE model behaviour shows that after metal-composite delamination the ring's stiffness can no longer be recovered, although this damage mode occurs almost at the end of the compression step in the simulation. Finally, after load release, the FE curve exhibits a similar final response to that shown in the experiment (point Z) related to the development of the residual indentation (Figure 4.4c).

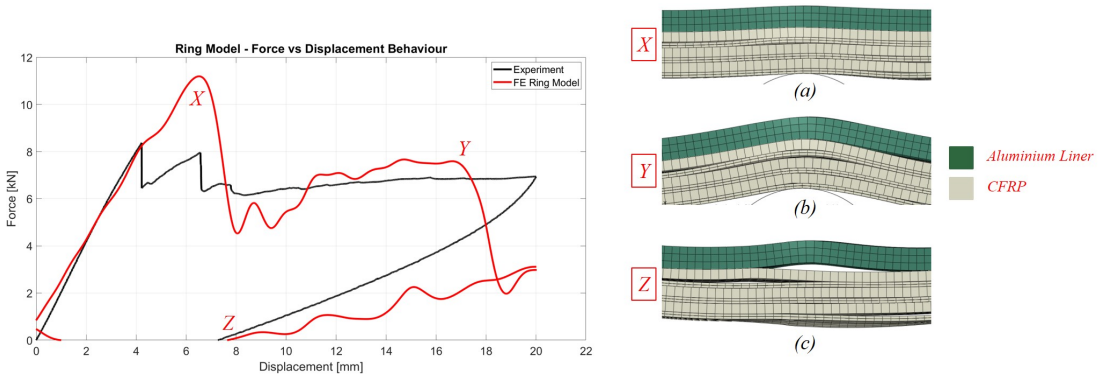

Figure 4.4: Force-displacement curve comparison FE vs. Experiment; a) Composite delamination; b) Metal-composite delamination; c) Residual indentation

As noted previously, nine different simulations were performed using combinations of parameter values shown in Table 4.3. In this work only the influence of the metal-composite interface fracture toughness variation is presented as it is a combination of interface strength and interface separation [102]. Figure 4.5 shows F-d response of the ring specimen under various interface fracture toughness values as well as ϵ_{xx} measurements performed on single nodes corresponding to the inner and outer face of the aluminium layer of the metal ring. It can be observed that, within a range of 750 J/m^2 - 1500 J/m^2 for G_{ic} and 1500 J/m^2 - 3000 J/m^2 for G_{iic} the model is relatively insensitive in terms of the resulting structural response. However, when comparing the ϵ_{xx} results, we find greatest consistency with experimental data using $G_{ic} = 1500 J/m^2$ and $G_{iic} = G_{iic} = 3000 J/m^2$.

4.3.2.2 Strain measurement results

As indicated in [2] the residual dent formed on a COPV has a strong correlation to the fatigue life of the component and, thus, it can be an indicator of the structure's post impact performance. Therefore, strain measurements were particularly carried out on the aluminium layer to investigate the residual dent development after loading. Figure 4.6 shows a comparison of the strain fields on the aluminium liner at the maximum point of compression (end of load step). Two different nodal measurements were compared at the maximum point of deflection on the lateral face of the ring. It can be observed that the tensile strain correlates well to the DIC measurement. However the compressive strain mea-

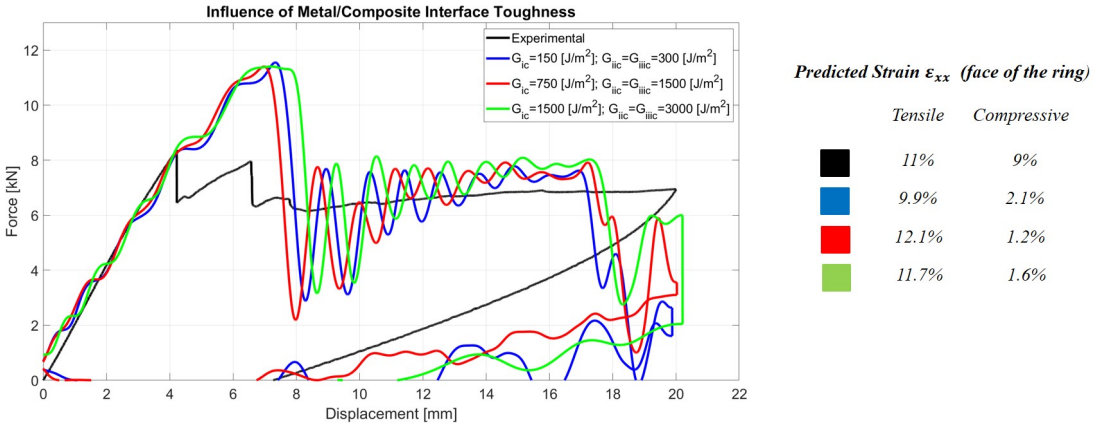

Figure 4.5: Ring specimen structural compression response under various metal-composite interface toughness values

surement indicates a large difference between the two results. It is likely that the level of delamination occurring beneath the metal is affecting the DIC measurements, hence giving a biased measure. Figure 4.7 shows the experimental and virtual residual indentation observed on the metal layer, which it is possible to observe a good correlation in terms of both shape of the metal indent, and the damage occurring in the composite.

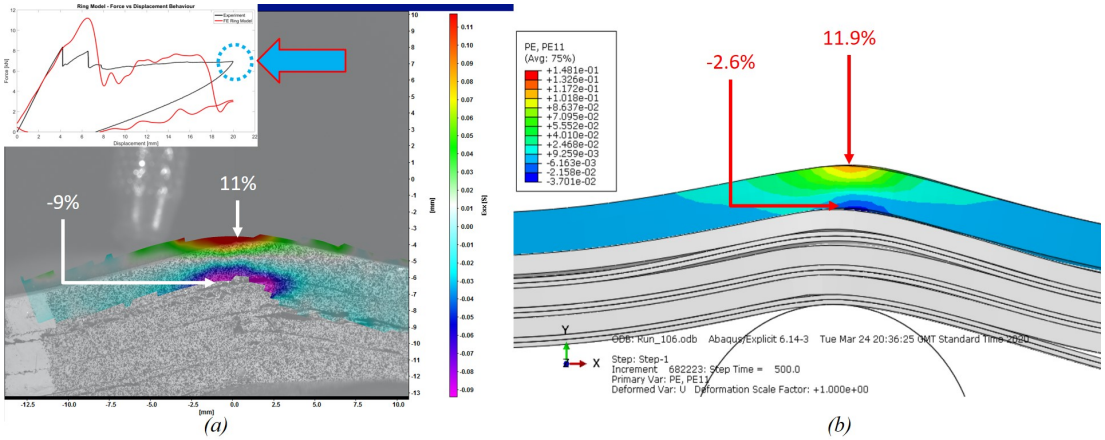

Figure 4.6: ϵ_{xx} strain measurements on aluminium ring; a)DIC; b)FE ring model

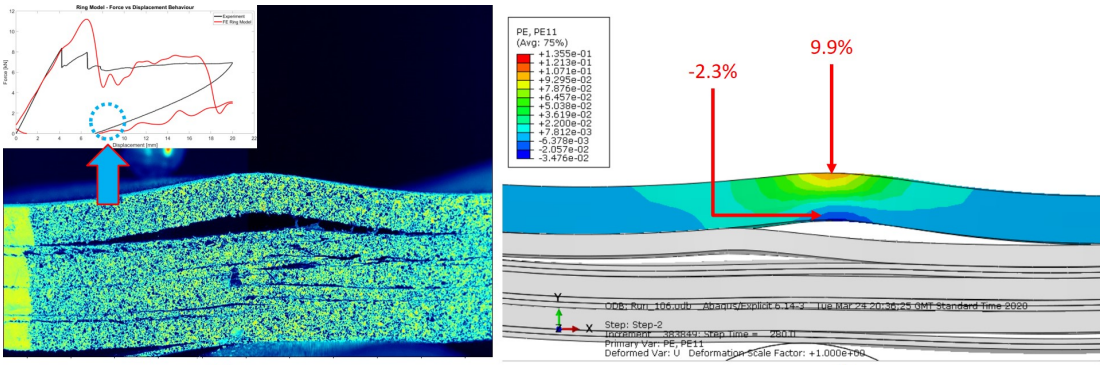

(a) *(b)*

Figure 4.7: Residual metal indentation of ring specimen; a)DIC; b)FE ring model

Following strain investigation on the metal ring, point, line and area measurements were made on the face of the FE and the experimental ring specimens for comparison. Additionally, these measurements were made at different applied displacements, *i.e.* measurements were performed at 2, 5, 7, 10, 15, and 20 *mm* during the loading phase (see Figure 4.8).

In order to investigate details regarding the dent formation, similar strain measurements were performed at different load application levels during the experiment and the simulation. The points at which the measurements were performed are shown in Figure 4.8. The first comparison was performed on specific nodal locations.

To perform point measurements using DIC, a specific coordinate was selected in the tensile strain region located two sub-regions lengths from the edge to avoid edge effect (Figure 4.9a). The images used throughout the loading and unloading steps of the experiment to perform the measurements can be found in Appendix A. The analogous node was selected in the FE model to compare strain measurements through the load application(Figure 4.9b). The point/node comparison though different loads during the experiment/simulation is shown in Figure 4.10. It can be observed that there is a good agreement between the two curves, although the FE curve is predicting a slightly higher strain value towards the end. Additionally, strain measurements were performed over a line of points that is placed along the thickness of the metal ring (Figure 4.11). Similar to the point measurements, DIC results were compared to an analogous line of nodes in

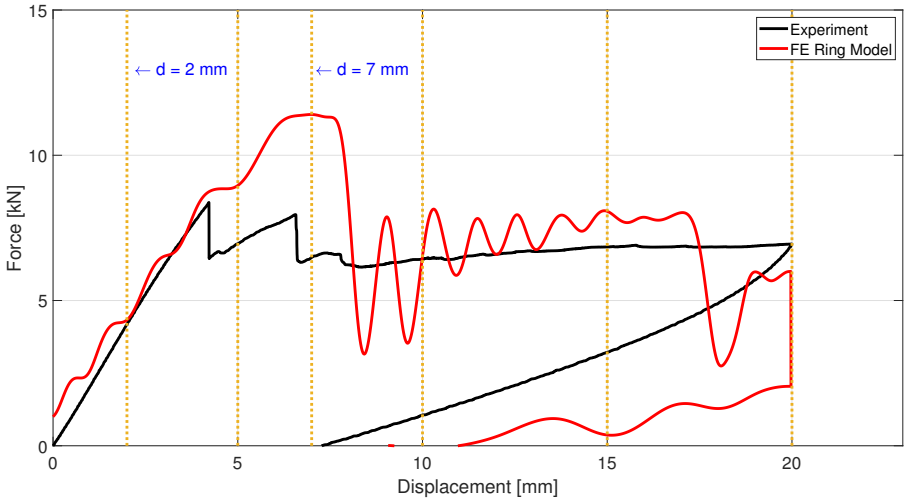

Figure 4.8: Reference points for point, line and area strain measurements comparison: DIC vs FE ring model

the FE model through the same applied displacement points. Figure 4.12 shows the FE vs DIC measurement comparison at different displacement application levels of the support on the ring. It can be observed that as the support displacement increases (*i.e.* increased ring compression) the agreement between the two measurements improves, especially at the end of the loading step (maximum ring compression). The measurement at 15 *mm* displacement shows the least agreement between DIC and FE attributable to large oscillations during the simulation as a result of metal-composite delamination.

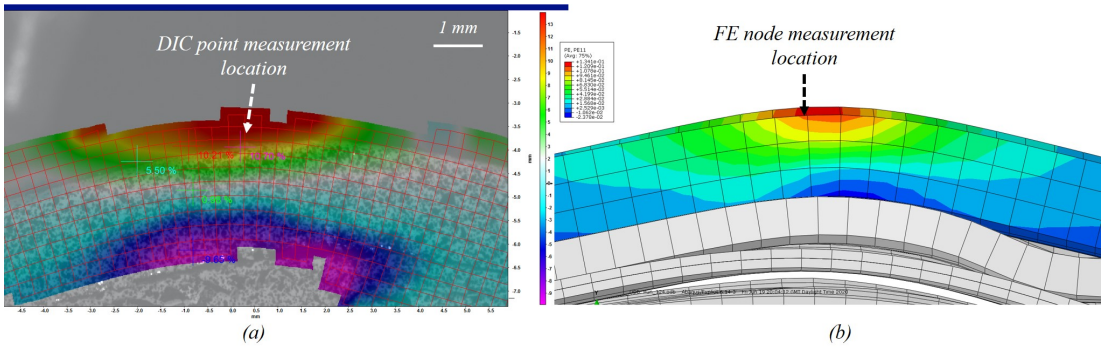

Figure 4.9: FE vs DIC ring measurement points

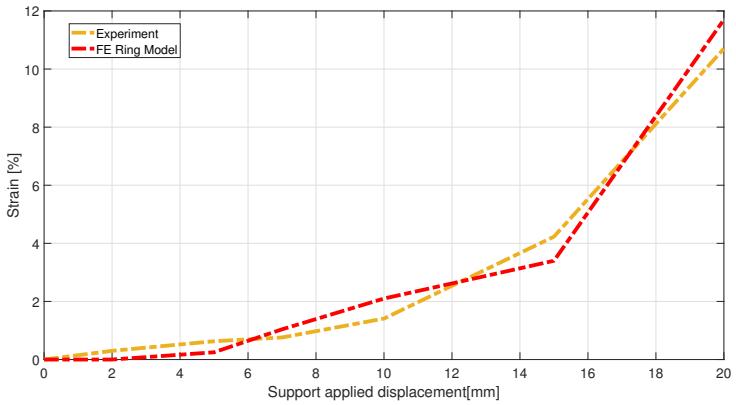

Figure 4.10: Point/node measurement comparison plot

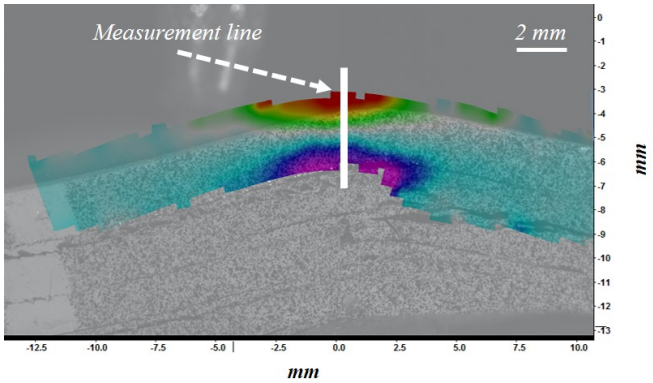

Figure 4.11: Line measurement on metal ring

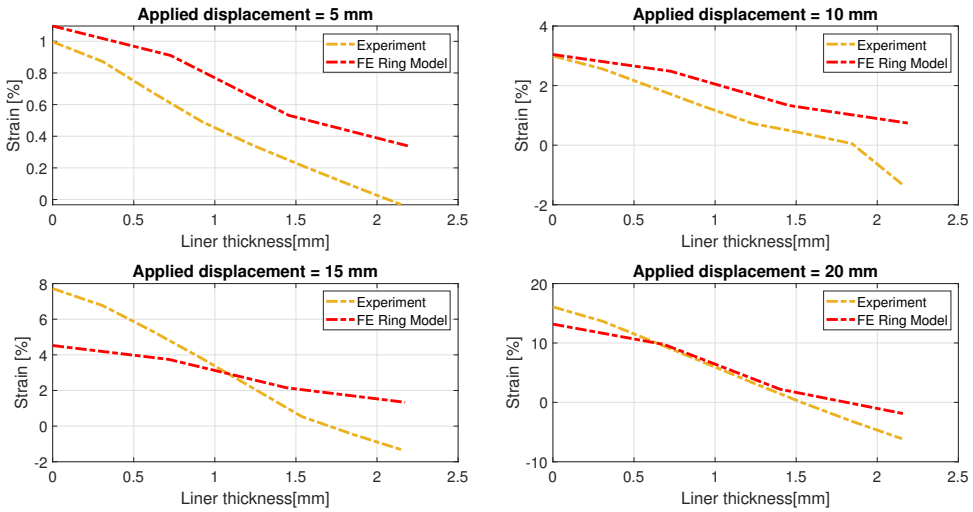

Figure 4.12: Line measurements performed at different load application on the ring specimen

Finally, area strain measurements were performed. To achieve this, strain values were taken from two different sized areas of the DIC (Figure 4.13) FoV. Area A is 5.22 mm x 1.53 mm and area B is 15.2 mm x 1.53 mm. The tensile strain values were averaged and registered every load increment during the loading step. A similar procedure was performed using the FE model. Figure 4.14 shows the resulting plots after comparing the FE and DIC averaged strains during the loading step. It can be observed a good level of agreement is achieved between both sets of results.

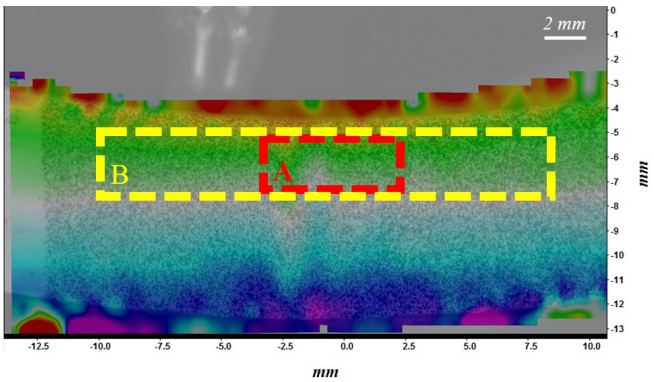

Figure 4.13: Areas for strain average measurement on metal ring

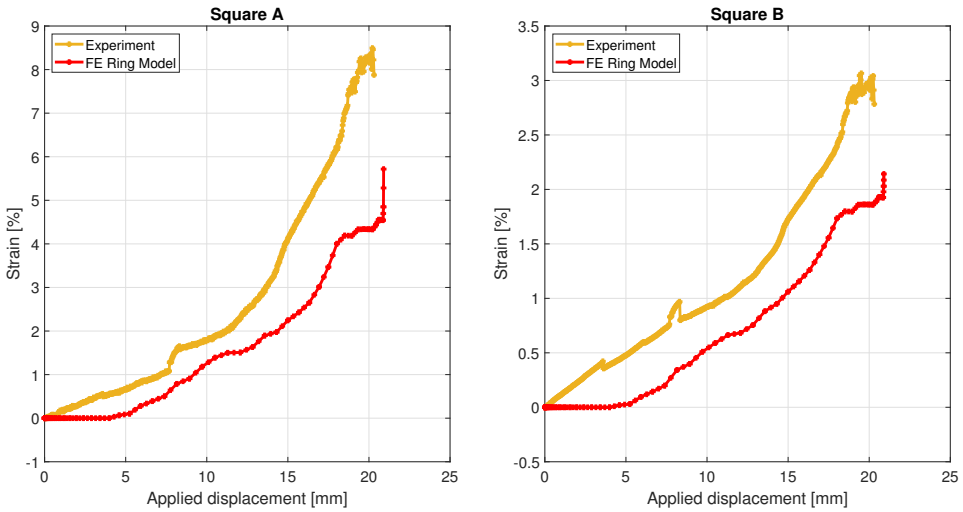

Figure 4.14: Strain average measurement comparison: DIC vs FEA

4.4 Discussion

Damage propagation during compression of a hybrid composite ring has been investigated and modelled. Previous approaches on damage investigation of COPV have focused on the use of CT scans and contributed to the assessment of post impact damage. The information collected and presented in Figure 4.3 shows the sequence in which damage occurs. The damage sequence starts with major two delaminations within the CFRP layers which produce a load drop in both cases. However after each load drop the structure still shows some stiffness recovery. The third main damage event is the metal-composite interface delamination after which the overall stiffness remains relatively low (Figure 4.4c). Additionally, it was observed that the highest metal deformation occurs after the metal-composite delamination. This suggests that the toughness of this interface may indeed be important in controlling the development of the residual dent on the metal ring. The described damage sequence occurs mainly during the increase in applied displacement, although some additional delamination was observed during the unloading phase. This suggests that the delamination mechanism is mainly driven by mode II delamination rather than mode I, which was previously suggested in [2].

The sequence obtained from the experimental test was used to validate the FE results. Despite simplifications made (*e.g.* no fibre or intralaminar) and type of solution (explicit solver) the overall predictions exhibit an acceptable behaviour. When both experimental and virtual F-d curves are compared there is a good degree of overall similarity, with some differences, that might be addressed by subsequent more refined models. The first load drop from the virtual F-d curve corresponds to damage occurring in the composite material, although it occurs during at a point of rapid progression. Following this mechanism, the major damage observed in the FE curve is due to the metal-composite delamination and associated yielding of the metal layer. Finally, the point at which the curves return to zero is similar to that in the experimental curve. The damage propagation sequence shown by the FE model is similar to that observed in the experimental test, however, differences are noticeable due to the high level of oscillations in the model and the *rapid* delamination simulated. Despite the differences and, giving the level of damaged occurred on the ring specimen, the model exhibits a good level of structural behaviour (shown in the F-d comparison) and the residual indentation (Figure 4.7).

The FE ring model is also used to estimate the properties of the metal-composite interface of the structure. The model was *calibrated* using a range of interface fracture values. The results shown in Figure 4.5 suggest that, regarding the overall structural behaviour described by the F-d curves, the model is relatively insensitive to the precise toughness value within a reasonable broad range. Given that the metal dent characteristics are known to be a strong indicator of remaining fatigue life, and hence damage tolerance, particular care should be taken if this is key parameter of interest.

4.5 Summary and conclusions

In this chapter a FE model of a hybrid metal-composite structure was presented and validated through experimental work. Metal-composite interface properties were estimated by comparing force-displacement structural behaviour and strain measurements obtained from experiments and FE modelling. The FE ring model predicts structural behaviour with a good level of agreement to the experimental

observations. Residual indentation prediction was validated through mechanical visualisation, chronological comparison and strain measurements.

Strain measurements exhibited strong agreement between the experimental and FE results. Validation activities are presented in relation to strain measurements on the ring specimen using DIC, which are compared to those obtained from the FE model. Only tensile strains are compared directly to the FE model as experimental compressive strain measurements were affected by delamination within the carbon fibre layers. Single point/node comparison exhibited a good correlation of strain measures through increasing load application. The result is consistent throughout the increment in applied displacement. Strain measurements over a line along the metal thickness during the loading phase show that, as the applied displacement increases and reaches 20 mm the agreement between DIC and FE measurements increases as well. In addition, different areas were taken to average strain measurements and compare to FE. Results exhibit noticeable differences which are presumed to be due to the lack of a matrix failure mode within the FE model. However, despite these differences, results show good overall agreement. The key overall conclusion of this chapter is that the use of embedded cohesive zone elements, together with appropriate constitutive laws for the materials, represents an effective approach for modelling the global and local structural response of metal-composite hybrid structures. This has particular significance for the prediction of damage tolerance and damage resistance of such structures. Furthermore, results suggest that the detailed model-experiment comparison, include global and local measurements of deformation and damage is the key to ensuring effective model validation and calibration.

Chapter 5

Full Type III cylinder cohesive element implementation

5.1 Introduction

Chapter 4 introduced a methodology to develop and validate a FE model of a hybrid metal-composite ring specimen subjected to a 2D line indentation. Qualitative comparison between model and experimental behaviour suggested good agreement, as the model described analogous damage mechanisms to those observed in the experiment. Quantitative validation using force-displacement curves and strain measurements at different ring locations was also presented. Results from such validation activities indicated that the model replicates the structural behaviour and residual strains of the deformed liner with good fidelity. Cohesive elements were selected to model the metal-composite and CFRP delamination mechanisms as cohesive zone layers. This model was used to calibrate such cohesive layers by identifying the traction-separation law parameters which best describe the structural behaviour of the ring exhibited experimentally.

This chapter presents a methodology to use the cohesive parameters selected from the ring model investigation and implement them into a full Type III cylinder model. Four different cylinder models were considered to implement the cohesive element methodology and compared to experimental force-displacement curves. The objective of this model is to investigate the development of the residual indentation on the aluminium liner observed after a quasi-static loading

reported in [2]. Results are discussed in relation to geometric boundary conditions, mesh size, simulation parameters and assumptions.

5.2 Geometry and boundary conditions

Type III cylinders modelled in this chapter are similar in geometry and construction to those as presented in [2]. Specimen dimensions and number of cohesive layers used for each FE model are described in Table 5.1. Each of these cylinders was manufactured by Luxfer specifically for research purposes only, *i.e.* they were not intended for commercial use. Boundary conditions on the FE model are analogous to those described in Section 2.5.

Table 5.1: Type III cylinder models dimensions

Name	Length [mm]	Outside diameter [mm]	Liner thickness [mm]	CFRP thickness [mm]	Cohesive layers
Model A	295	85	1.8	2.0	3
Model B	443	114	2.3	2.8	4
Model C	525	159	2.2	4.6	6
Model D	556	173	3.1	4.2	4

The information reported in [2] regarding the indentation damage developed on cylinder Model C, was used as the basis for the first Type III full cylinder model and to investigate the validity of the numerical assumptions. Material properties for the metal and the composite rings are the same as those used for the ring model described in Section 4.2.1, *i.e.* Aluminium 6061 and T700s respectively. Several assumptions were taken to select the appropriate boundary conditions and reduce computational simulation time. Some authors have reported the complexity of dome region modelling and the effect that the fibre alignment in this region has on the impact response directly to the dome [88, 90]. However, this project investigates the damage response of the barrel section of the cylinder and, hence, it was assumed that the indentation is sufficiently far from the dome region so that it does not have a significant effect on the residual

deformation prediction. Consequently, the dome region was not modelled in detail as reported, reducing the number of elements and interactions included in the simulation. Nonetheless, it was observed that removing a significant part of the geometry had an effect on the initial elastic response of the overall structure behaviour. Simulations were conducted to investigate such effects and a steel plate with equivalent stiffness properties was included in the model instead to match the initial structural stiffness. Effects of the end plate simplification instead of using a detailed model for the end dome are discussed in the results section.

Only 1/4 of the cylinder geometry was used along with symmetric boundary conditions to reduce computational time. The indenter is a 8 mm radius hemisphere, which is modelled as a rigid body due to the low level of deformation observed during the experiments in this component. The support is the same as used for the ring specimen described in Section 4.2.2, however, to be consistent with the rest of the boundary conditions, for this model only 1/4 of the support's geometry is modelled. In contrast to the ring model, the support is static and the enforced displacement was directly applied to the hemispherical indenter. As for the ring model, the simulation is performed through loading and unloading steps. The total displacement used on each step for Model C is 8.5 mm to be consistent with the analogous experiment. Figure 5.1 shows a summary of the full cylinder FE model.

Regarding meshing parameters, the model was divided in two main regions, one which intends to be used as a geometrical boundary condition without any delamination and another which is expected to show delamination based on experimental observations. The former contains an average element size of 6 mm and the latter has a 0.6 mm element size. The finer mesh size was selected in such way so as to ensure that there are enough cohesive elements in the cohesive zone region, based on the process described in Section 3.2.4. The length of the finer section of the ring was initially selected as 30 mm, which is $\approx$ 20% of the geometry's total length. The effect of the length of the cohesive region within this model is discussed in further sections. The model contains 133165 elements with 247944 nodes. It was run using the University of Southampton's Iridis super computer using 4 nodes in parallel with 8 CPU each. With this computing configuration total running time for this model was $\approx$27 hours.

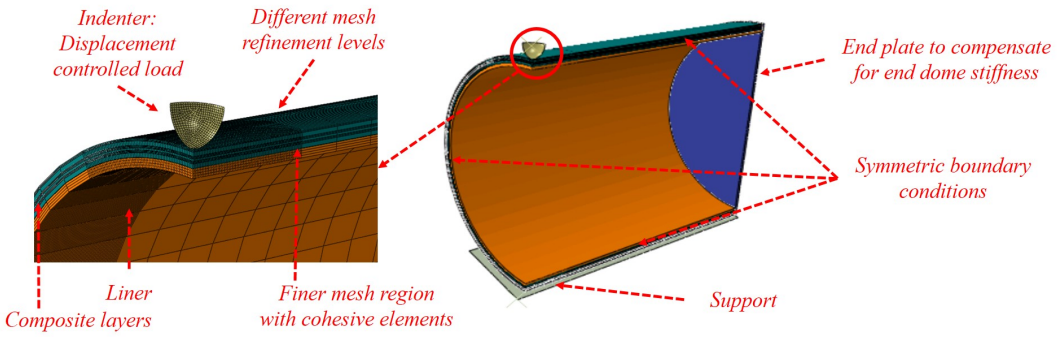

Figure 5.1: Full cylinder FE model geometry, mesh and boundary conditions

5.3 Results and discussion

5.3.1 End plate validation

A separate study was performed to assess the validity of the end plate assumption. To achieve this, modified versions of Model A and Model C cylinders were developed. The purpose of this activity was to investigate the initial stiffness reduction of the full cylinder model as a result of the dome region removal. For this reason, the modified versions of the full cylinder models contains only one layer of cohesive elements in the metal-composite interface, i.e. no delamination effect was included in the perfectly elastic composite layers. The extent of delamination or the amount of damage was not assessed nor the residual indentation. For these simulations, only F-d curves were compared as initial stiffness is investigated here in relation to the simplification of the dome geometry. The steel plate added at the end of the cylinder has already been described in Section 5.2 and shown in Figure 5.1.

Figure 5.2 shows the experimental F-d curves of Model A and Model C cylinders compared to their modified FE version. For each cylinder model, two FE versions were developed, one with and one without the end plate. In both cases, it is very clear that there is a better initial stiffness correlation with the added end plate. Model A shows a good agreement between the experimental and the virtual results for the loading step of the analysis. However, the added plate makes the initial stiffness and the final reaction force predictions closer to the experimental result. Similarly, Model C shows a better agreement to the

experimental curve using the steel plate. In both cases, the steel plate has the same 2 mm thickness, so no modifications were made to have a better fit between different cylinder models, suggesting that the end plate assumption is valid for both cases.

An additional observation during this step of the investigation is the effect of the lack of composite damage included in this simulation. Giving the low level of composite damage observed on Model A, the loading curve does not exhibits a significant difference to the experimental behaviour. However, this is not the case for the unloading step, in which the FE model prediction shows a quasi-linear recovery, which is not consistent with the very non-linear experimentally observed response, and the much larger residual displacement at zero load. Correspondingly, Model C shows differences which presumably are due to the lack of composite damage modelling. However, in this case the difference is exhibited in both loading and unloading steps. On the F-d curve, the FE model does not indicates the development of the liner yielding. Instead of this behaviour, the FE model results indicate a constant increase of loading (i.e. no load drop) during the loading step and a quasi-linear recovery of the structure, which may result in a higher error in the residual dent prediction. This quasi-elastic response of the FE cylinder structure suggests that the composite damage has a significant effect on the structural behaviour and the development of the residual indentation on the liner. Therefore adding some level of composite damage (such as delamination) to the model is key for a better residual dent prediction, particularly for cases such as Model C where the composite layers are twice as thick as the aluminium layer.

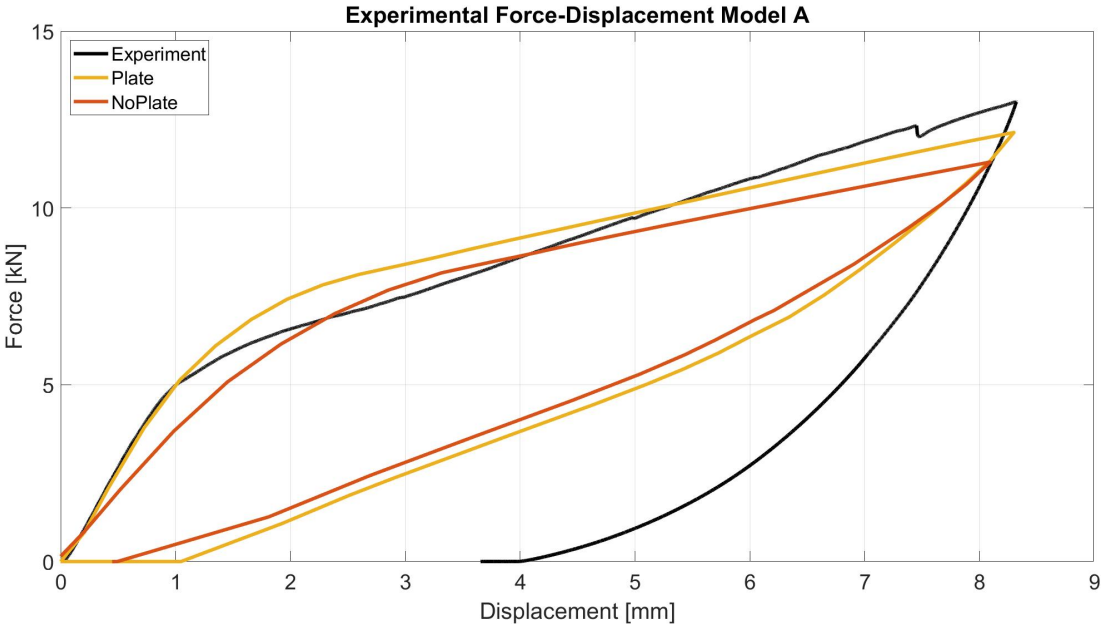

(a)

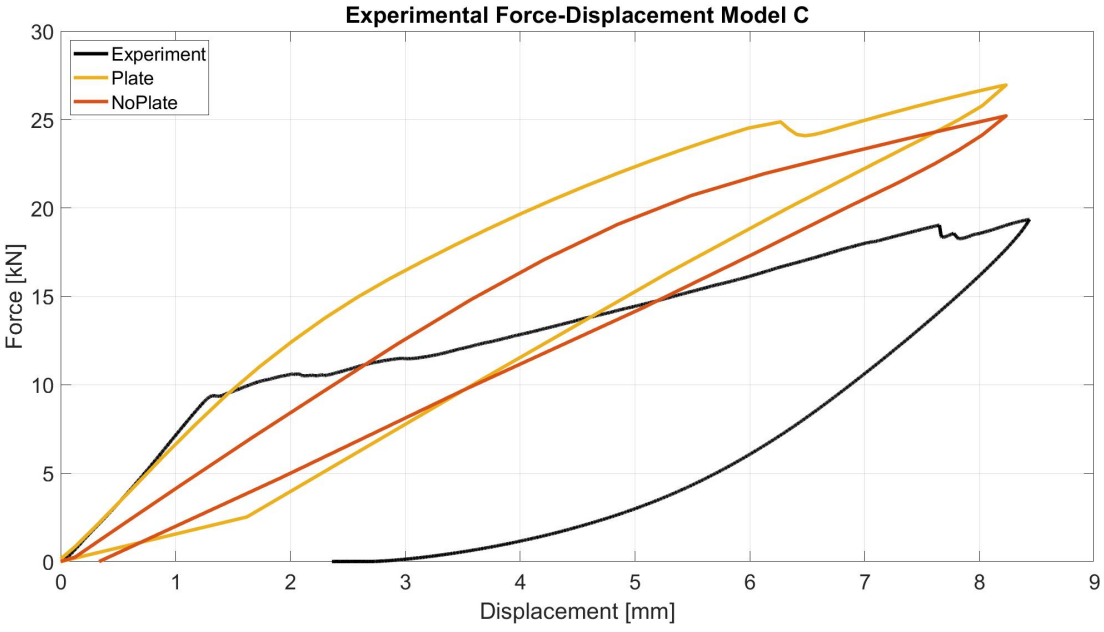

(b)

Figure 5.2: Force-displacement curves comparison of a Type III cylinder barrel with a 2-mm thick steel end plate vs cylinder with no end plate; a) Model A, b) Model C

5.3.2 Full cylinder model vs. experimental comparison

Compared to Section 5.3.1 the results presented in this section contain the full development of the Type III cylinder, *i.e.* the model includes the six layers of cohesive elements on both metal-composite and CFRP interfaces to predict delamination. Figure 5.3 shows the comparison of the experimental Model C cylinder behaviour and the FE result. It is observed that the FE model correlates well to the experimental curve as it predicts the main features of the F-d behaviour. The initial elastic response is well correlated although there are some differences that can be attributed to noise, as no delamination was observed at the indenter's displacement of 1 mm. The first slope change, related to the metal yielding, is also well predicted by the FE model. This behaviour was not exhibited by the model described in Section 5.3.1, which confirms the hypothesis that the composite delamination has a significant effect on the overall structural behaviour and the metal deformation. Moreover, the curve shows a good correlation with the predicted peak force having a 6.2% difference to the experimental value. Similar to the elastic response, noise is noticeable in this region of the curve, however this can be attributed to the delamination occurring at different interfaces of the model. Thus, for this particular section of the curve, the model is not only predicting the structural behaviour but the damage occurring in the composite, which was also reported in the experimental results. The unloading behaviour is also well captured by the FE model. It can be observed that both curves show a similar response. This result also confirms the significant difference exhibited by adding composite damage modelling, in contrast to the results shown in Section 5.3.1 in which the unloading behaviour was closer to a linear response.

Using this model it is also possible to observe permanent deformation progression in the metal liner as well as damage propagation in the different interfaces. Figure 5.4 shows the development of the residual dent in the aluminium liner compared to specific points of the F-d curve. Point A shows the onset of metal yielding with a 3.1% plastic deformation of the liner. Point B shows an intermediate point between the initial loading and maximum indentation. It is possible to observe that the plastic deformation of the liner has increased up to 7.8% along with some delamination. The plastic strain exhibited at point C is similar to that shown at the end of the load application (point D) which is 13.2%

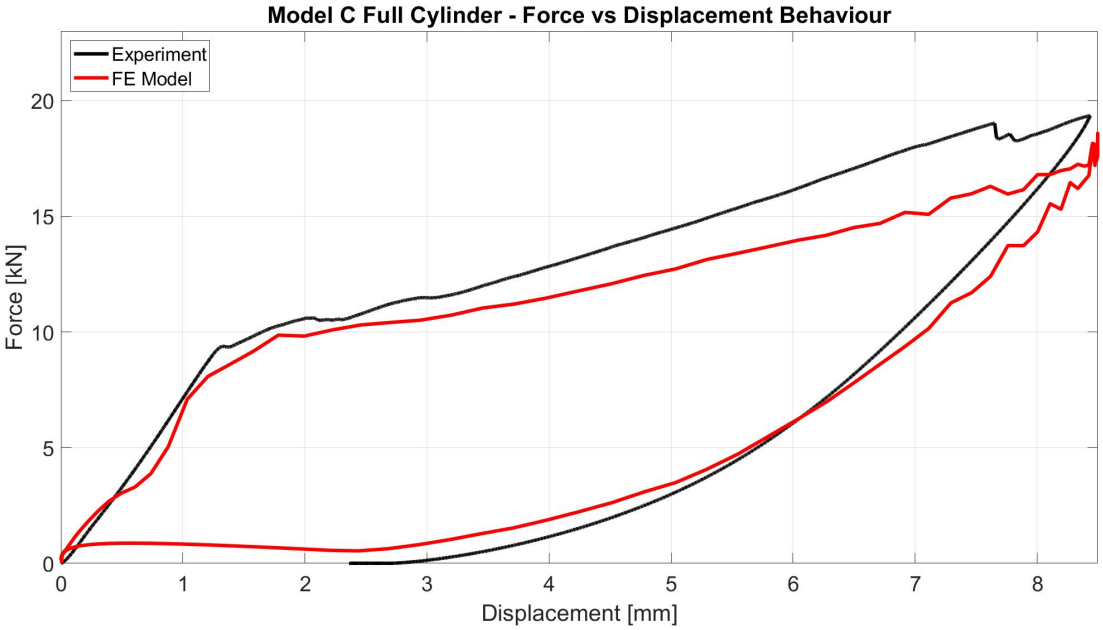

Figure 5.3: Model C force-displacement curve, experimental vs FE model results

and 13.1% respectively. This results suggests that for Model C construction, once the maximum load has been applied, the deformation of the metal liner has reached its maximum extent. This could be considered for robust design purposes focusing on reducing the maximum displacement allowed by the liner under maximum load application.

Along with dent development, damage propagation in the individual interfaces can be explored using the FE model. Figure 5.5 shows different levels of damage observed in the delamination region where the cohesive elements were defined. Similar to the indentation analysis, each level of delamination is related to a specific section of the F-d curve. Each image shows the outermost layer and the innermost layer, where the former is the top cohesive interface layer of the CFRP material and the latter is the metal-composite cohesive interface. Point A shows no delamination during the onset of aluminium yielding, thus, being in the elastic response region suggests no significant damage to the structure. The intermediate Point B shows some level of delamination in the top and the metal-composite interface. From the bottom view, it is observed different levels of delamination at different layers, where the metal-composite cohesive layer delamination is the highest. In contrast to the plastic strain development in the liner, Points C and

D on Figure 5.5 exhibit a significant difference in the results. Delamination levels between those points are different despite having a similar deformation in the liner. The main difference between these two points is the region that has been damaged. Point C corresponds to the maximum compression being applied to the structure, as such, it is suggested that the observed damage here was developed under mode II delamination. Moreover, Point D damage corresponds to complete load removal on the cylinder and residual dent being fully developed. At this regions of the curve, it can be observed that cohesive elements on the centre, (*i.e* elements directly under the indenter) have been also removed, which suggests that delamination occurred in mode I. Results reported in [2] suggested that metal-composite decohesion would occur during the unloading stage of the experiment under mode I as a consequence of the elastic recovery of the composite whilst the liner has been permanently deformed. Results shown by the FE model suggest that this is true for some regions of the indentation area, however there is also extensive damage occurring in mode II delamination during the loading stage. This delamination behaviour is consistent with the results exhibited by the ring model.

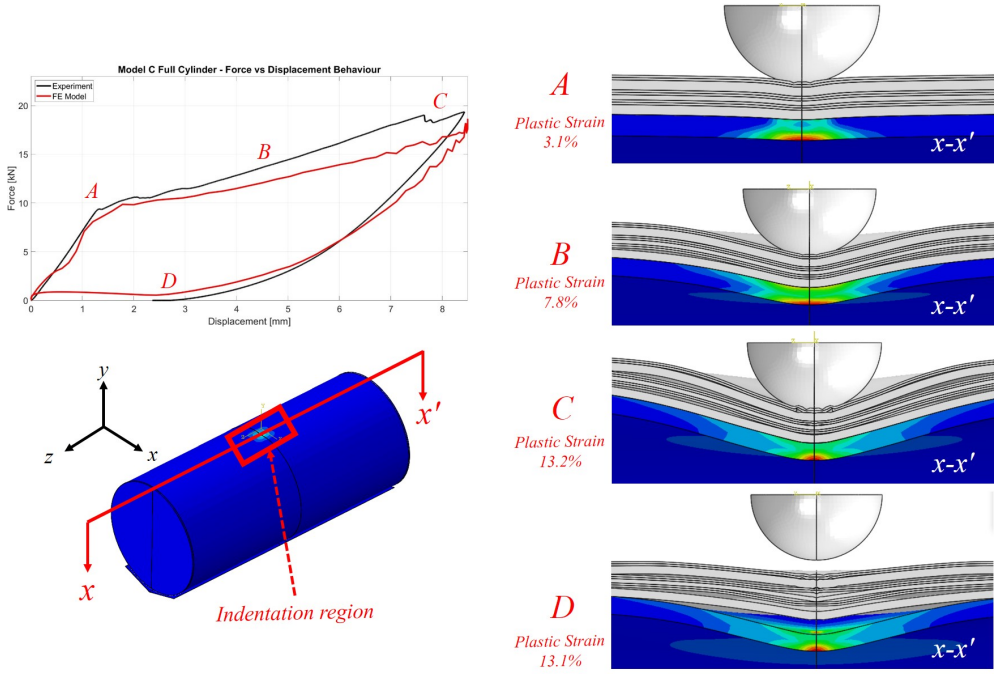

Figure 5.4: Residual dent development on the metal liner of Model C Type III cylinder

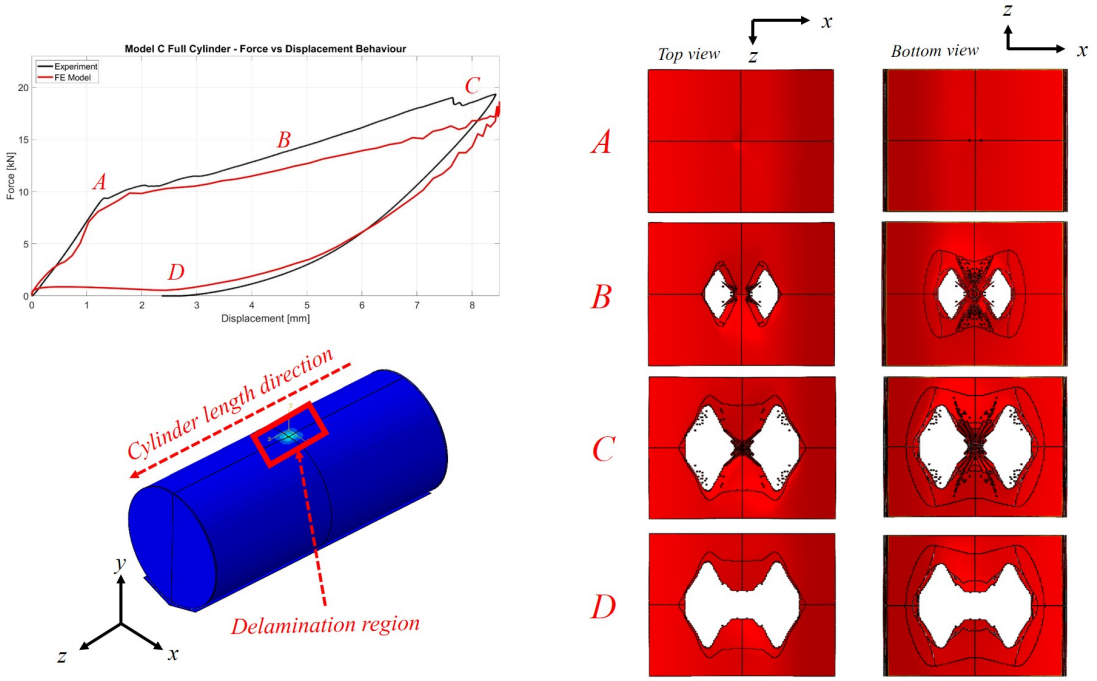

Figure 5.5: Damage propagation of metal-composite and CFRP layers of Model C Type III cylinder

Following quantitative validation of the full cylinder model, measurement of residual indentation was performed. Figure 5.6a shows the residual indentation depth predicted by the FE model, which is 5.09 mm. The value reported in [2] is ≈ 4.3 mm, which would make the FE estimate have an error of 15.5%. This value is acceptable considering the level of damage occurring in this simulation and the assumptions taken to reduce computational time. A more direct qualitative comparison between the CT scan and the FE resulting residual dents is shown in Figures 5.6b and 5.6c. This comparison suggests good correlation of the model with the residual indentation, but also some features such as the dent and delamination of the CFRP layers.

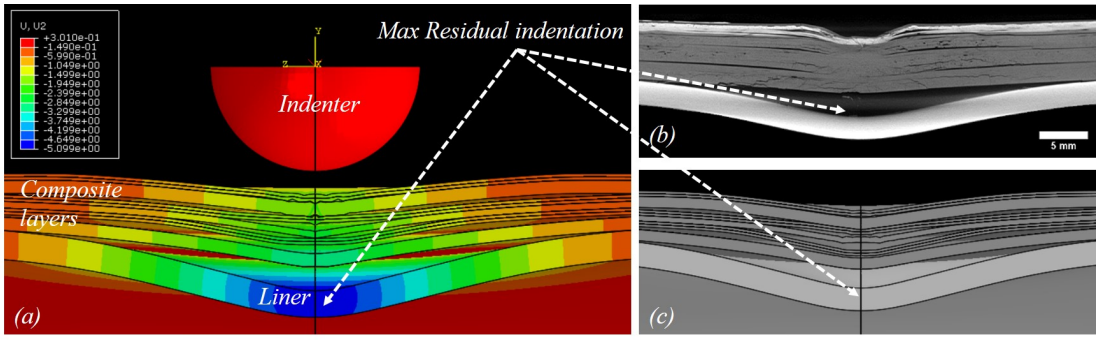

Figure 5.6: Residual dent in Model C cylinder after load removal; a)FE dent depth result, b) CT scan indentation [2], c) FE indentation

Damage area measurements were also reported in [2]. The value for a Model C cylinder is 2500 mm2 at a ≈ 20 kN peak force. Although this is approximate, this measurement offers an idea of the delamination extension, which can be then compared to the FE model predictions. For a clearer reference to the reader, each layer on the model has been named as describe in Figure 5.7. Figure 5.7a shows a view of the model's solid element layers in which each material is indicated. Figure 5.7b shows the cohesive element layers which are within, layer L1 corresponds to the metal-composite interface layer, and layers L2-L5 correspond to the composite interface layers. Figure 5.8 shows that delamination occurred on every interface layer of Model C, although the extent of delamination is different for each layer. Based on the limit set by each layer, delamination is shown at different levels by observing the projected area associated with layers from the outside and the inside of the cylinder (5.8a & 5.8b). For instance, it

is observed that L5 shows a delamination extent (Figure 5.8a) which is different than that observed in layers L2 to L4. In contrast, Figure 5.8b shows that the metal-composite interface developed the largest delamination. These differences in the delamination between each layer are the result of the different fibre direction of the plies, and is consistent with delamination observed in composite plates [132]. In both cases, an estimation of the projected area was performed to compare versus the experimental values. The projected area considered has an elliptic geometry and each area considered is described in Figure 5.8. For the outermost layer, the calculated area is 1508 mm^2 and for the innermost area (metal-composite interface) the estimated value is 2073 mm^2.

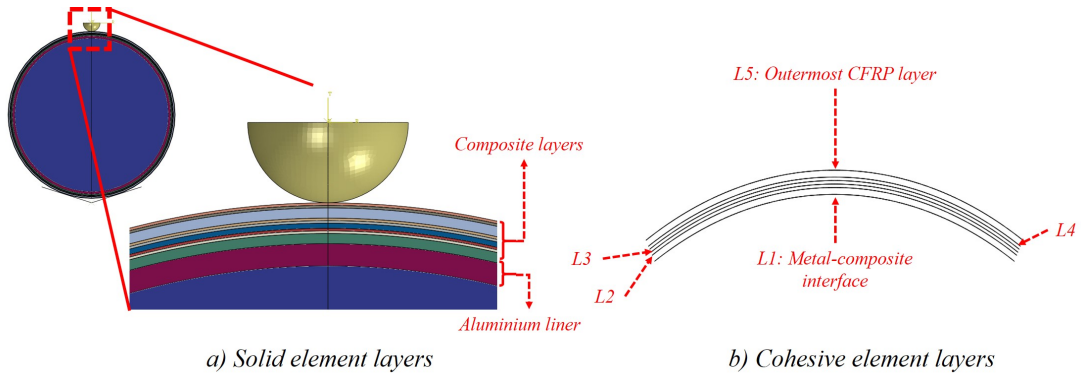

Figure 5.7: Cohesive element interface layers within the Type III cylinder model

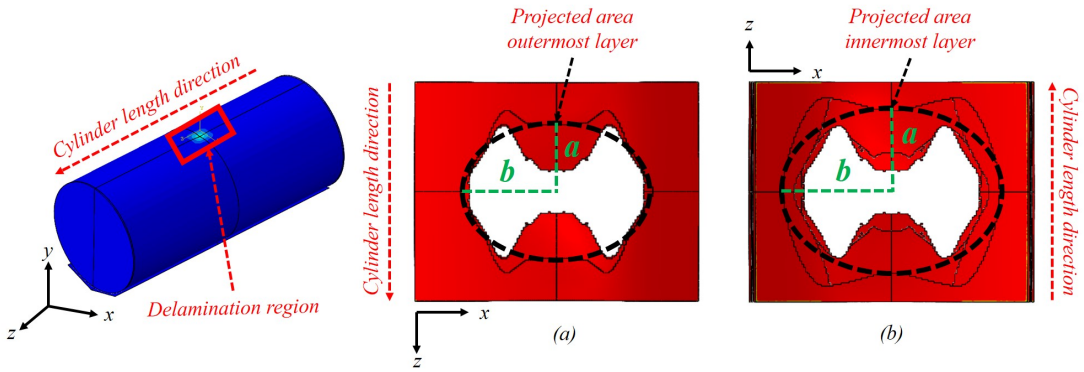

Figure 5.8: Model C delamination after quasi-static loading; a) Outermost CFRP layer, b) Metal-composite interface

5.3.3 Cohesive implementation on several Type III geometries

The current model aims to be used for design exploration purposes and, as such, the model must be proven to be reliable under boundary condition changes, *i.e.* different geometry, materials or constructions can be explored with the model using the same cohesive parameters for the metal-composite interface. To test the reliability of the model to geometric changes, more simulations were performed using the Type III cylinder models described in Section 5.2. A python script was created to automate the pre-processing activities related to model generation such as creating the geometry, materials and boundary conditions[1]. For instance the script is able to create an almost full Type III cylinder FE geometry automatically, and only geometric parameters are needed to be specified. Cohesive elements still need to be created manually as they depend on the mesh and automated numeration created by the software. Despite this process being performed manually, full model generation was reduced from 1 full working day to $\approx$ 20 minutes, depending on the experience of the operator. In this section, the script is used to validate the cohesive model under different geometric conditions, however it is also used for parametric investigation activities in Chapter 6. For Model A, Model B and Model D cylinders no liner dent depth was reported in [2], thus FE results are compared only to experimental F-d curves. Figure 5.9 shows the FE to experimental comparison for these cylinder types. All cylinders have the same end plate thickness (2 mm). Regarding the cohesive element region (finer mesh area), each cylinder has also 20% of the total length populated with cohesive elements, except for Model D which had to be extended to 30%. Details about the effect of the extent of the cohesive elements are discussed in further sections. These models were run similarly to Model C, on Iridis supercomputer using 32 CPUs. Details of number of elements and simulation time are described on Table 5.2.

Model A shows a similar behaviour to the one exhibited by Model C with acceptable correlation between the FE and experimental F-d curve. The total error regarding the peak force is 7%. In contrast, models B and D show an over

[1]Full script can be access upon request via University of Southampton repository https://doi.org/10.5258/SOTON/D1635

Table 5.2: Type III cylinder models running time @32 CPUs

Model	Nodes	Elements	Solution time
Model A	78803	42214	20 hrs
Model B	139165	78130	23 hrs
Model D	435695	239843	+35 hrs

prediction of peak force towards the end of the loading stage. The error is 20% and 28% respectively. As suggested in Section 5.3.1, as the thickness of the CFRP layers increases the effect of the damage on these is higher, that is why Model A showed a good correlation to the experimental values on the loading part of the curve without having composite delamination included in the model. The results presented in this section show a similar behaviour with respect to the number of cohesive layers contained in the cylinders. For instance, the overestimation of stiffness exhibited on the F-d curves from Model B and D corresponds to the reduced number of cohesive layers (4) modelled compared to Model A (6). The lack of delamination in the composite implies less energy dissipation through composite damage, hence, resulting in a stiffer structure. This effect could be reduced if more cohesive layers or matrix/fibre damage were included in future models.

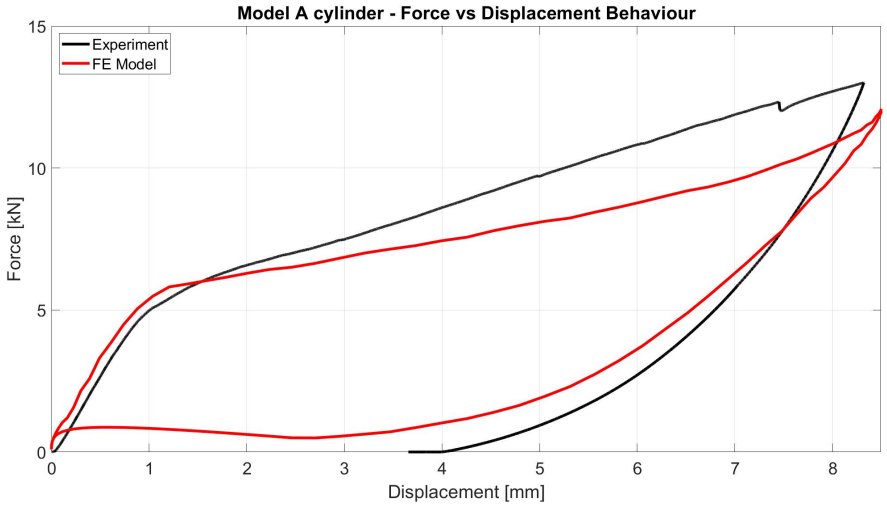

(a)

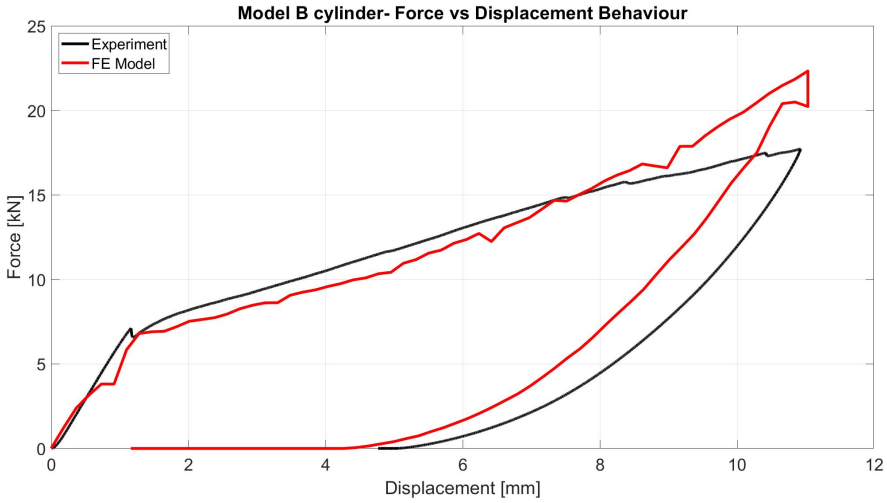

(b)

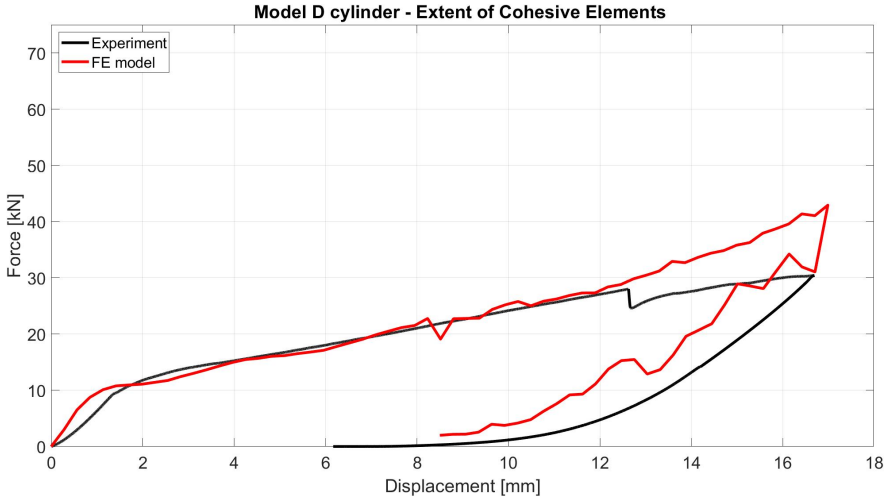

(c)

Figure 5.9: Comparison of experimental and FE force-displacement curves of different Type III cylinders

5.3.4 Extent of cohesive element layers

Simulation results showed that there is an effect of adding or removing cohesive element layers to the model for CFRP delamination. For instance, having a low number of composite layers results in an over-prediction of the peak load as there is less energy release through damage and the structure appears to be stiffer. A similar effect occurs in the model when the predicted delamination area is larger than the area of cohesive elements defined in the model. Based on the indenter radius and the delamination observations on [2] it was decided that the extension length of the cohesive elements (refined region) have an equivalent of 20% of the total length of the geometry. This initial assumption worked well for the Models A, B and C, in which it was observed that the delamination is not limited by the area of the cohesive elements but by the delamination extent itself (Figure 5.8). In contrast, Model D exhibited a different behaviour under this assumption. Figure 5.10 shows that the number of cohesive elements remaining intact at the end of the simulation is low and these are mainly concentrated at the edges, which suggests that this is more an edge effect rather than the interface not undergoing delamination. A more thorough study was performed to investigate an adequate procedure to determine the required initial area of cohesive elements in the model.

Two additional Model D versions were created with extended cohesive areas to observe the effect of delamination and F-d curves. The new cohesive regions are 25% (Area A) and 30% (Area B) of the total cylinder length (Figure 5.11), additional to the original model which is 20% of the original length. Each model with a different cohesive element area produced a new level of delamination. Results shown in Figure 5.12 suggest that a larger area of cohesive elements allows a better prediction of delamination without limiting damage. Delamination shown on Figure 5.12b suggests that the cohesive element area should probably also be extended in the hoop direction as delamination appears to be limited, which can increase the apparent stiffness of the structure. In addition to the delamination observations of these models, F-d curves were compared to the experimental results to analyse the effect of each cohesive extent region. Figure 5.13 shows the F-d curves of Model D using different length of cohesive regions. This results indicate that a larger cohesive area results in a better correlation to the experimental curve. The over prediction of the model with the larger cohesive

element area may be a consequence of the limited area on the hoop direction mentioned earlier. Given the increased number of degrees of freedom of the model with the larger cohesive element area, simulation was terminated before the end of load removal due to restrictions on computational time available. Results shown in this section must be considered for optimisation and robust design purposes, specially when modelling large cylinders such as the Model D. However, it is also suggested that further model optimisation is performed so bigger cylinders can be simulated, *e.g.* the use of shell elements or modified boundary conditions that allow the reduction of degrees of freedom with the minimum loss of accuracy.

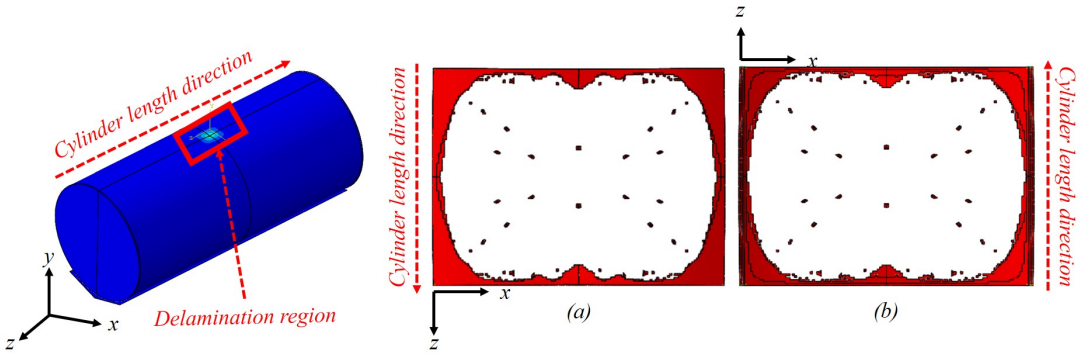

Figure 5.10: Model D delamination after quasi-static loading; a) Outermost CFRP layer, b) Metal-composite interface

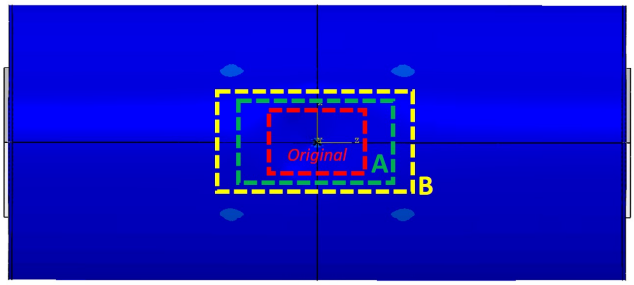

Figure 5.11: Cohesive element areas used for Model D Type III cylinder

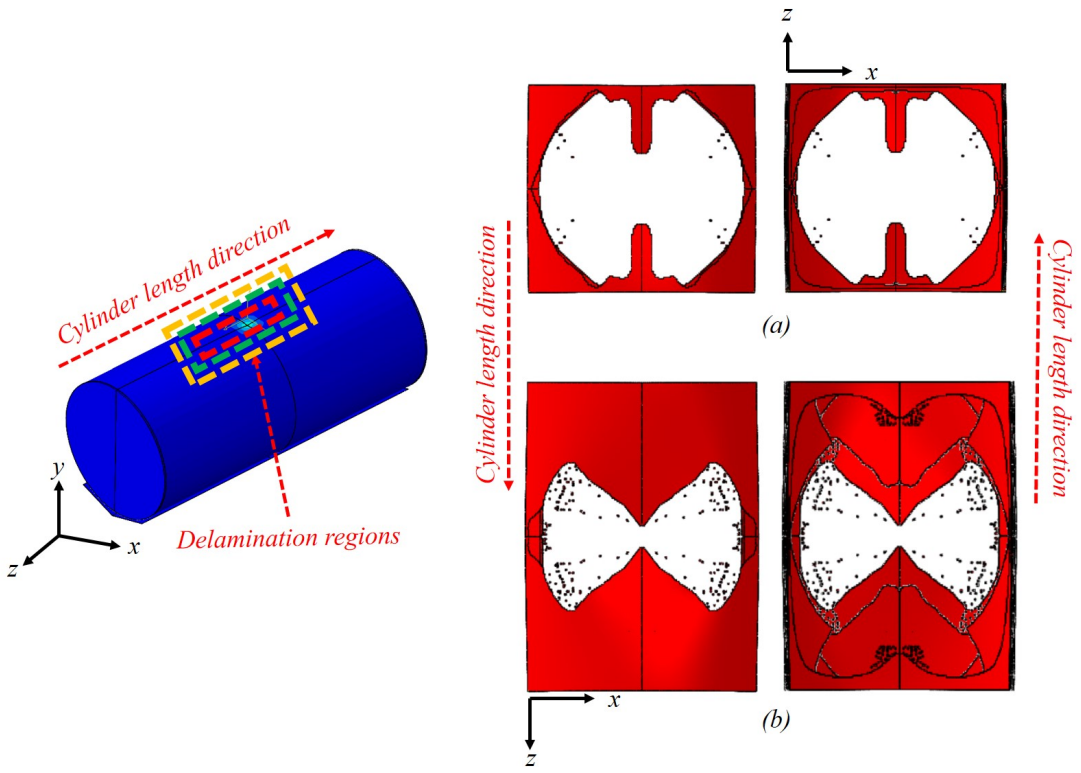

Figure 5.12: Model D delamination results using different size cohesive element areas, a) Area length 25% of cylinder length; b)Area length 30% of cylinder length

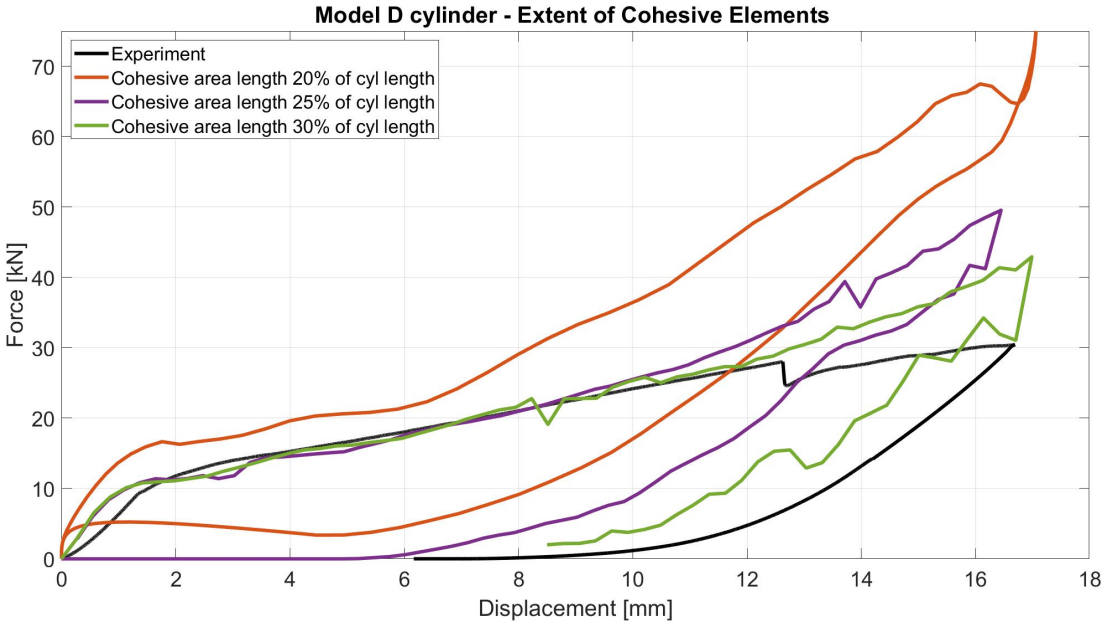

Figure 5.13: Model D F-d curves using different size cohesive element areas

5.4 Conclusions

A methodology to implement cohesive elements into a full Type III cylinder has been described in this chapter. Moreover, this numerical model has been applied to a range of cylinder designs with different geometries and good correlation between simulation and experimental results has been demonstrated. As part of the modelling strategy the end domes of the cylinder were not explicitly modeled, but replaced by flat, homogeneous steel end plates with equivalent structural stiffness. It was shown that interface properties estimated through cohesive elements in Chapter 4 provide a good model-to-experiment correlation when implementing them in a full Type III cylinder. Validation of this was provided through comparison of the F-d curves, residual dent depth and delamination area measurements. All the cylinder models described and investigated in this chapter showed good correlations when compared to experimental F-d curves. In each case, prediction of the initial elastic response, material yielding (first slope change), similar peak force and non-elastic unloading response were shown. Additionally, in the case of Model C, results showed good correlation values for the residual dent measurement and the projected delamination area, which was also confirmed with

qualitative comparison between FE results and a CT scan image. Therefore, it was concluded that it is possible to use the same interface properties in various cylinder designs without any additional calibration to that described in Chapter 4. Overall, it was concluded that the methodology presented in this chapter can be used to develop FE models to explore design opportunities for Type III cylinders as the interface parameters used have been tested under different design conditions and the validity of results has been demonstrated.

Chapter 6

Parametric investigation of a Type III cylinder using a finite element approach

6.1 Introduction

In previous chapters, a full Type III cylinder FE model was developed and validated. The key feature of the model is the cohesive element methodology used to explore the influence of the toughness values of the metal-composite interface within the hybrid pressure vessels investigated in this project. In this chapter, the model is used to perform parametric investigations for Type III cylinder design optimisation. Finite element modelling is widely used for informing design decisions in many industries (e.g. automotive, aerospace, ship) as part of the engineering process to investigate possible designs with a reduced number of built prototypes, hence, reducing costs [133–135].

Parametric investigation presented in this chapter is divided into four sections to test a range of design possibilities and their effect on cylinder behaviour and residual dent development. First, different constituent materials were selected and added to the FE model as an alternative to the current Al-6061 for the liner and the T700s for the composite wrap. Furthermore, the metal-composite interface estimated in Chapter 4 was modified in the full cylinder model in order to determine the effect of this interface on the residual dent development. Two more

models with modified liner and wrap thickness were proposed and are presented in this chapter. A theoretical burst pressure of each proposal was calculated to provide a better context for the design requirements of a cylinder. Finally, quasi-static loading simulations of Type III cylinders under internal pressures are also presented. FE models of COPV combining quasi-static or LVI loads have been reported to predict burst strength after impact or to investigate damage propagation in the composite layers due to burst pressure loads [136–138]. Results presented in this project focus on the residual dent development as a key indicator for post-damage fatigue performance, including internal pressure and post-impact re-pressurisation, which, to the author's knowledge, has not been widely reported. Overall, results are discussed in relation to how these parametric variations affect the F-d curves and the residual dent depth.

6.2 Methodology

Liner and wrap materials, layer thicknesses ratio and metal-composite interface properties are design parameters to be modified using the FE model. These parameters were selected based on the current model capabilities and the industrial interest to understand the liner's behaviour subject to potential design variations. In each case, results are analysed comparing F-d curves, delamination extent and residual dent depth. In addition, the effect of internal pressure on residual dent depth development is investigated.

6.2.1 Material modification investigation

6.2.1.1 Cylinder liner material

Materials proposed for this investigation are Al7075 and Ti6Al4V, both offering higher strength compared to the current Al-6061. Material properties are described in Table 6.1. Titanium alloys are unlikely to be seriously considered for these cylinders, but is included as a means of illustrating the capability to explore potential design considerations. Similarly, a comparison of the materials' stress-strain curves is shown in Figure 6.1. Material modification was performed directly into the model, it was not necessary to build a new model as the new

material can be specified directly in the model code, while preserving the original.

Table 6.1: Material properties for different liner materials [139]

Material	E [GPa]	Yield [MPa]	UTS [MPa]	el [%]	K_{ic} [MPa-$m^{1/2}$]
Al-6061 T6	69	272	310	17	29
Al-7075 T6	71	495	572	11	29
Ti6Al4V Grade 5	114	920	950	14	74.6

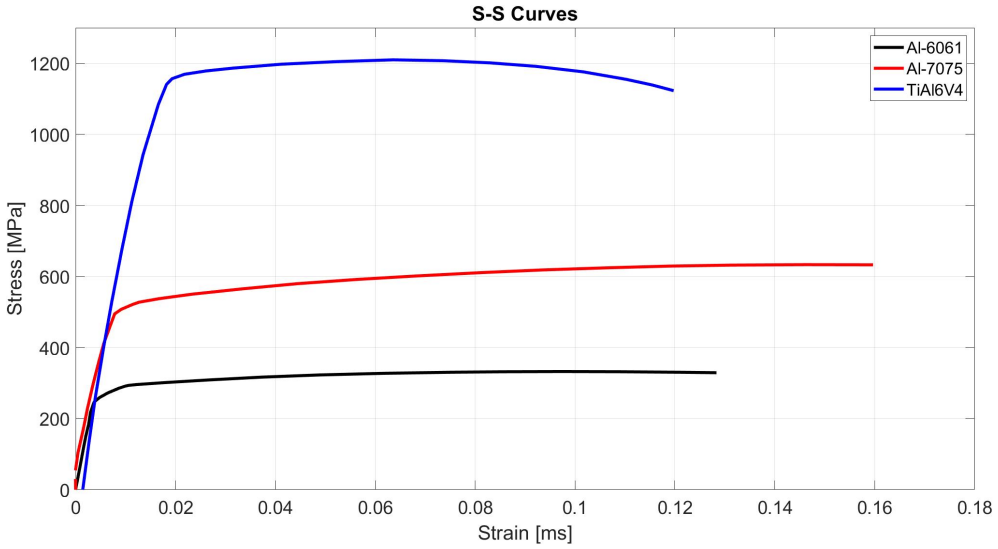

Figure 6.1: Liner material options stress-strain curves [139]

6.2.1.2 Cylinder wrap material

Following investigation of representative material parameters, materials were selected to investigate the influence of a stiffer fibre on the wrap of the cylinder. Consequently, a Toray T1000 and high modulus fibre M60J materials were proposed for the FE model. Ply level properties were calculated based on the rule of mixtures used by Scott [3]. Calculations were performed assuming a fibre volume fraction of 60% [140–142]. Properties of each material are described in Table 6.2. Similar to Section 6.2.1.1, the material was specified directly into the model's code, *i.e.* Abaqus' GUI was not used.

Table 6.2: Material properties for different cylinder wrap materials

Property	T700	T1000	M60J
E_{11} [GPa]	139	177	360
E_{22} [GPa]	6.63	10.1	10.4
G_{12} [GPa]	3.78	3.78	3.78
ν_{12}	0.26	0.26	0.26

6.2.2 Metal-composite interface parametric investigation

Chapter 4 presented a calibration of the metal-composite interface within a hybrid metal-composite ring structure, representative of that found on Type III cylinders. As such, a range of values were suggested according to the results exhibited in the chapter. In this section, further values are proposed to simulate a higher and a lower interface toughness within a Type III cylinder, to analyse the contribution such change would make to the residual dent development. Design advantages are discussed in relation to F-d curves, indentation dent depth and delamination. The proposed interface parameters are described in Table 6.3. The objective is to investigate damage development due to an interface which is half as tough and another which is twice as tough as the baseline case used in Chapter 5.

Table 6.3: Metal-composite interface properties for virtual parametric investigation of a Type III cylinder

Interface	$G_{ic}[J/m^2]$	$G_{iic} = G_{iiic}[J/m^2]$
Baseline	1500	3000
Twice baseline	3000	6000
Half baseline	750	1500

6.2.3 Materials thickness ratio investigation

In this section, two FE models with similar total thickness but different liner and CFRP thickness ratios are proposed for comparison to the baseline specimen de-

sign. Additionally, cylinder weight and theoretical burst pressure of each proposal is calculated because these parameters are highly important to the cylinder's design requirements. The FE models presented in this section have similar geometric characteristics to the model presented in Chapter 5, thus, only the cylinder's barrel geometry is considered to calculate both burst pressure and weight.

Type III cylinder material thickness ratios used for these models are shown in Table 6.4. First, the current specimen's design is specified for reference. Then two different models are shown, the former shows a thin liner with a thick CFRP wrap, and the latter model is a thick liner with a thin layer of CFRP material. Model A configuration is expected to be more dent tolerant due to the thin liner being more compliant, whereas model B configuration is presumed to be more dent resistant due to the thick liner.

Table 6.4: Proposed FE model for thickness parametric investigation on Type III cylinders

Model	Metal Thickness [mm]	CFRP Thickness [mm]	Weight (Barrel) [kg]	Theoretical Burst Pressure [MPa]
Baseline	2.2	4.6	1.22	314
Model A	1.0	5.25	1.06	353
Model B	5.24	1.51	1.47	117

Burst pressure and cylinder weight were calculated considering only the cylinder's barrel. Calculations were performed using thin shell theory considering the sum of the pressure carried by each material as described in equation 6.1 [143].

$$P_b = P_l + P_c \tag{6.1}$$

where P_l is the pressure carried by the liner and P_c is the pressure carried by the composite wrap, given by:

$$P_l = \sigma_l \frac{2t_l}{R_l} \tag{6.2}$$

$$P_c = \sigma_c \frac{2t_c}{R_c} \tag{6.3}$$

where σ_l and σ_c are the ultimate tensile stresses of each material, R_l and R_c are the internal radius of each cylinder section and t is the thickness.

6.2.4 Effects of internal pressure on dent depth development

The effect of quasi-static indentation on pressurised cylinders is investigated in this section. The significance of this study is that cylinder drop or impact tests are usually specified, for safety reasons, to be carried out on un-pressurised cylinders. The question arises as to what extent this is representative of the service environment and whether it is a conservative requirement for damage resistance and damage tolerance considerations. Thus, the aim is to measure the effect of internal pressure on the development of the residual dent on the liner. Two models were developed throughout this section: pre-indentation and post-indentation pressurisation models. Pre-indentation pressurisation models refer to investigating liner deformation whilst internal pressure has been applied to the cylinder, which will be referred to as a *pressurisation-loading-unloading* cycle. Pressures applied before quasi-static indentation were 10, 15, 20, 30 and 45 MPa. The last two pressure values correspond to Model A's approximate design pressure and burst pressure respectively.

In contrast, post-indentation models refer to the internal pressure applied after the quasi-static indentation has been performed. Two different post-indentation cycles were created: *loading-unloading-pressurisation* and a similar cycle which includes pressure release at the end. The former gradually applies 6 MPa pressure steps up to 30 MPa, and the objective is to determine whether, and at what pressure, the dent may be "pushed back" to its original shape and "closes" the gap between the two materials. The latter applies 30 MPa pressure and then releases it to observe the residual indentation after the cylinder is emptied. Each post-indentation pressure cycle is described in Figure 6.2.

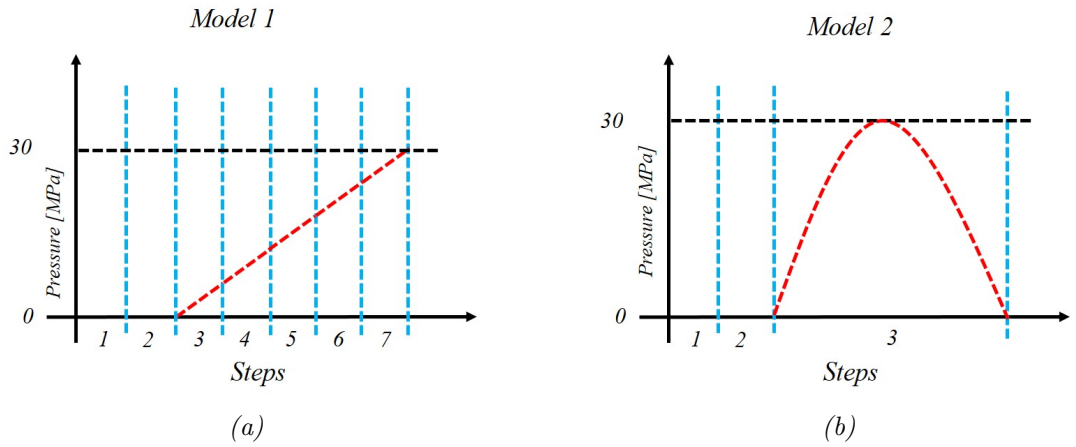

Figure 6.2: Post-indentation pressure cycles for Type III cylinder FE models; a) Pressurisation; b) Pressurisation and pressure release

6.3 Results and discussion

6.3.1 Materials investigation for liner and composite wrap

Figure 6.3 shows the F-d curve comparison between different liner materials along with the predicted residual dent depth. Results suggest that the model with Al-7075 liner shows least sensitivity to this material change, where it can be observed that the initial elastic response, the slope change and the peak force prediction are similar compared to the Al-6061 model. Regarding the dent depth estimation, the Al-7075 model showed a reduction of $\approx$ 13% in comparison to the Al-6061 model. In contrast, the Ti6Al4V model shows a more significant change when compared to the Al-6061 model. Simulation results suggest that with Ti6Al4V the overall stiffness of the cylinder increases, which may contribute to an increase of the damage resistance properties of the structure. Moreover, the residual dent prediction indicates a reduction of $\approx$ 30%. Based on the observations reported in [2] this reduction could contribute to a better post-impact performance of the cylinder. Although this information should be confirmed via experimental testing, the results give some information that could be used to make decisions in early product design stages. It is important to note that titanium is probably not a practical material, due to cost considerations and its lower formability compared

to aluminium alloys, but the comparison is nonetheless instructive.

Figure 6.4 shows the FE residual indentation result of the Type III cylinder with different liner materials (see Table 6.5). Delamination areas are presented in the same form as in Chapter 5, in which it is possible to observe the outermost and the innermost (metal-composite interface) cohesive layers. In agreement with the F-d and residual dent results, delamination on the outermost CFRP layer areas between Al-6061 and Al-7071 models exhibit no significant difference. This is not the case when comparing the baseline model in Figure 6.4a to the Ti6Al4V model in Figure 6.4c, where there are significant differences in the outermost and the innermost cohesive layers. In regard to the former, there is a noticeable reduction of the delamination extent in the CFRP material, however, it appears that the metal-composite interface in Figure 6.4c has delaminated more than in the equivalent model shown in Figure 6.4a. This indicates that, although there is a reduction in the residual depth dent, the extent of the damage is larger, which may be a consequence of the titanium's higher yield stress. Although there is no evidence that relates delamination areas to the cylinder's damage tolerance, special care should be taken when exploring different materials as results suggest an improvement in residual dent depth but more extensive delamination, that could also adversely affect the cylinder's performance.

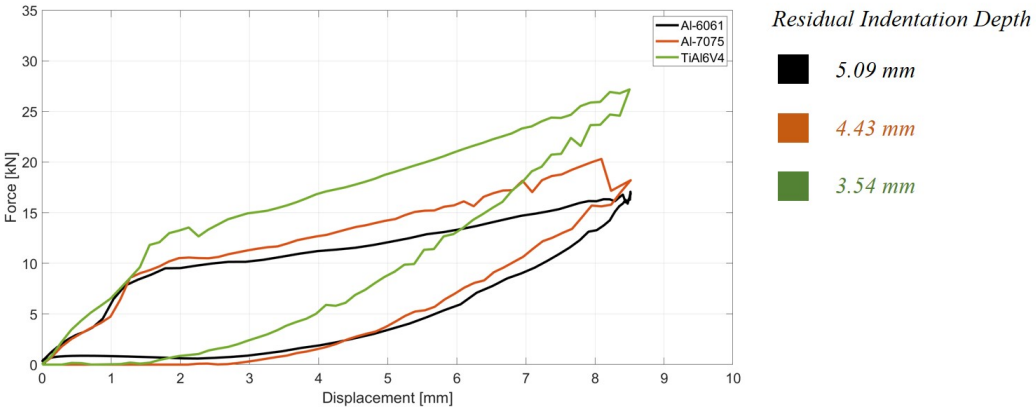

Figure 6.3: Virtual comparison of F-d curves of a Type III cylinder with different liner materials

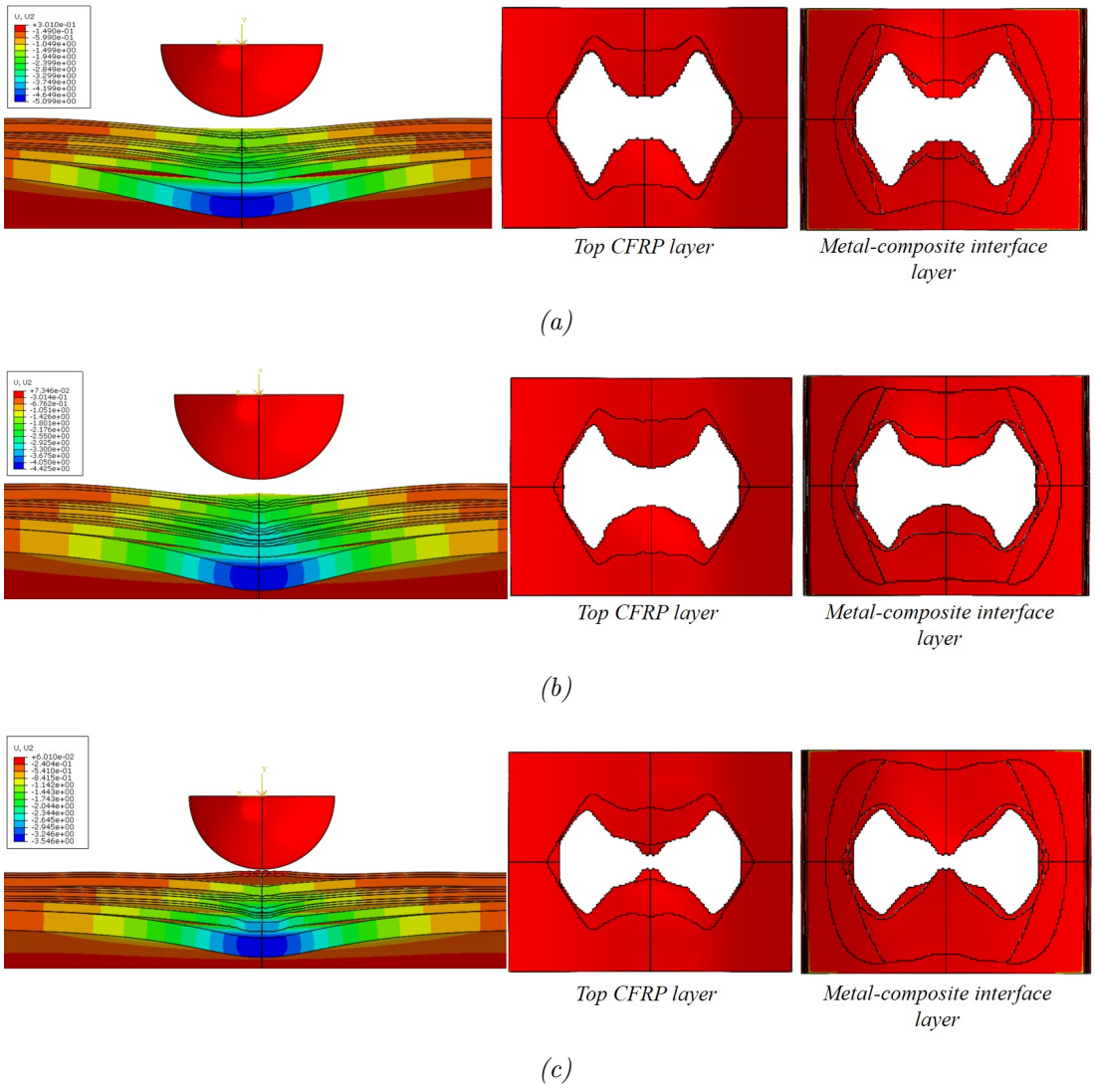

Figure 6.4: FE residual indentation and delamination in a Type III cylinder with two different liner materials; a) Al-6061 b) Al-7075, c)Ti6Al4V

The cylinder sensitivity to changing the wrap material is presented in Figure 6.5 showing the F-d curves comparison for different fibre materials. These curves are similar to the previous material comparison shown in Figure 6.3. A noticeable difference is seen in the initial response shown by the M60J, which is stiffer than the rest of the materials. However, with respect to residual dent depth, the FE results show that there is little improvement achieved by changing the fibre material. This material change can enhance the damage resistant properties of

Table 6.5: Delamination area comparison of a Type III cylinder with different liner materials

Material	CFRP			Metal-composite		
	a	b	Area $[mm^2]$	a	b	Area $[mm^2]$
Al-6061	26.1	18.4	1508.7	29.6	22.3	2073.7
Al-7075	26.7	18.4	1543.4	31.1	25.7	2510.9
Ti6Al4V	28.3	15.4	1369.2	32.1	24.8	2500.9

the structure but will not have an important effect on the damage tolerance as the dent depth is not reduced. However, in a qualitative comparison of the residual dent and delamination, these results show that the M60J fibre wrap induces more extensive delamination, especially in the metal-composite interface (Figure 6.6). Although a higher structural stiffness is achieved overall, this could lead to a reduction in damage resistance as the extent of composite delamination is larger (see Table 6.6). Similar behaviour to that shown by the liner material change is exhibited by this result. When comparing Figure 6.6b and 6.6c (T1000 and M60J respectively) it is possible to observe that the outermost layer suffered more extensive delamination, however it is also noticeable that some of the intermediate layers did not delaminate completely from the centre. To sum up, the results showed in this section suggest that no significant dent depth reduction is achieved when modifying the elastic properties of the composite wrap material of the Type III cylinder, however it can have a considerable effect on the extent of delamination damage. It is important to note that the delamination toughness of the composite was not varied as part of this investigation, and was kept at the baseline values.

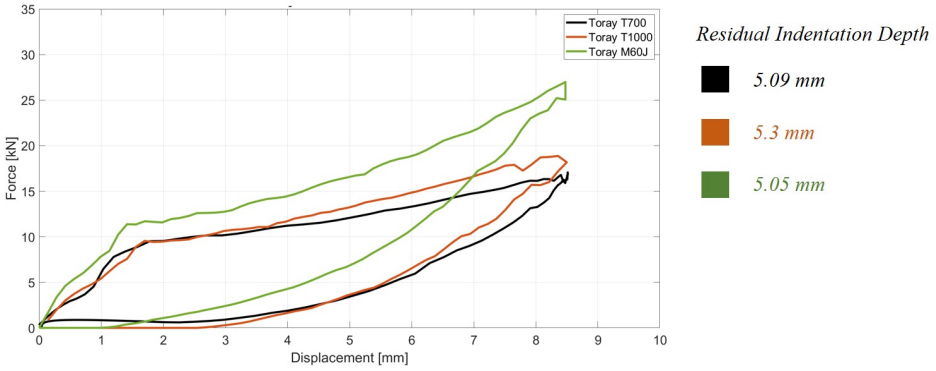

Figure 6.5: Virtual comparison of F-d curves of Type III cylinder with different composite wrap materials

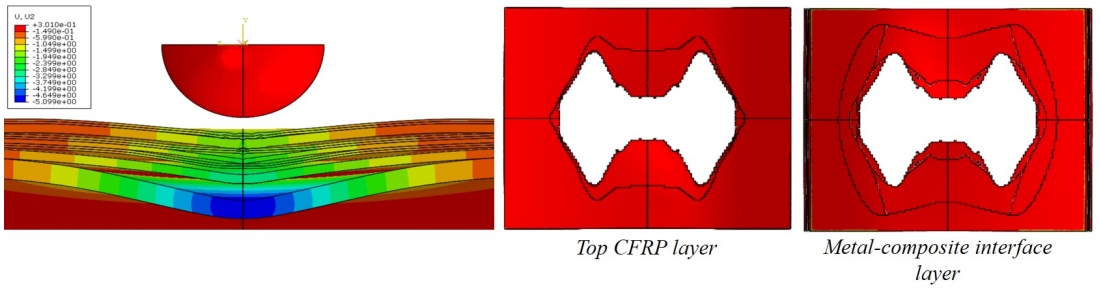

(a)

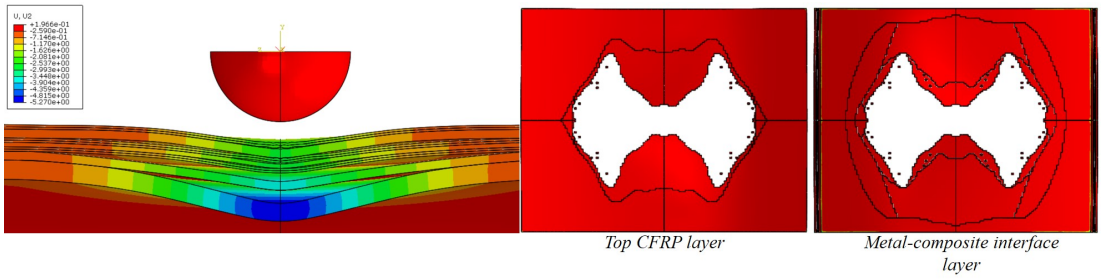

(b)

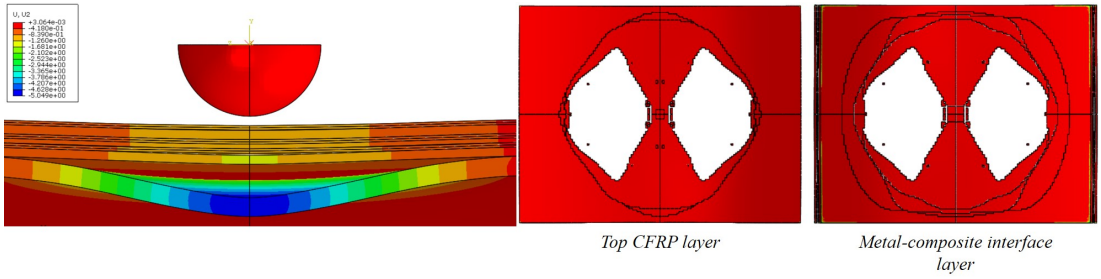

(c)

Figure 6.6: FE residual indentation and delamination in a Type III cylinder with two different composite fibre materials; a) T700s, b) T1000, c) M60J

Table 6.6: Delamination area comparison of a Type III cylinder with different composite wrap materials

Material	CFRP			Metal-composite		
	a	b	Area $[mm^2]$	a	b	Area $[mm^2]$
T700	26.1	18.4	1508.7	29.6	22.3	2073.7
T1000	27.7	18.4	1601.2	30.1	28.3	2676.1
M60J	27.7	28.2	2454.1	31.1	28.2	2755.2

Overall, results show that material modification in the liner or in the composite wrap does not result in an enhancement for the cylinder design under the loading conditions described. However, it can be noted that the loading applied is displacement controlled. This would represent a worst case condition as the displacement will be directly transferred to the liner. In the case of a LVI event, the loading would be force or energy controlled and the resultant depth dent would vary with different material configurations. Thus, simulating an impact event in which boundary conditions include the dynamics of the geometry is recommended.

6.3.2 Metal-composite interface parametric investigation results

Figure 6.7 shows the F-d curves model with different metal-composite interface properties. Similar to previous results, indentation depth predictions are also shown. From the F-d curve and indentation depth prediction, there is no significant improvement achieved due to modifying these parameters. However, indentation contour and delamination results suggest more apparent differences (see Figure 6.8). The model with a higher interface toughness (Figure 6.8b) shows a reduced delamination extent which is similar in all the cylinder's layers, including the metal-composite interface. In contrast, the lower interface toughness model (Figure 6.8c) shows a smaller delamination in the outer CFRP layers but a larger delamination area in the metal-composite interface. Hence, increasing the interface toughness to have some reduction in delamination at the indentation area does not result in a reduced dent depth. This is confirmed when comparing the

delamination area of the metal-composite interface for different models as shown in Table 6.7. Considering the reduction in the delamination area, it is suggested that the damage tolerance properties of the cylinder would not be highly improved as a consequence of this change, nonetheless, other cylinder properties are enhanced, such as damage resistance and residual burst pressure [137].

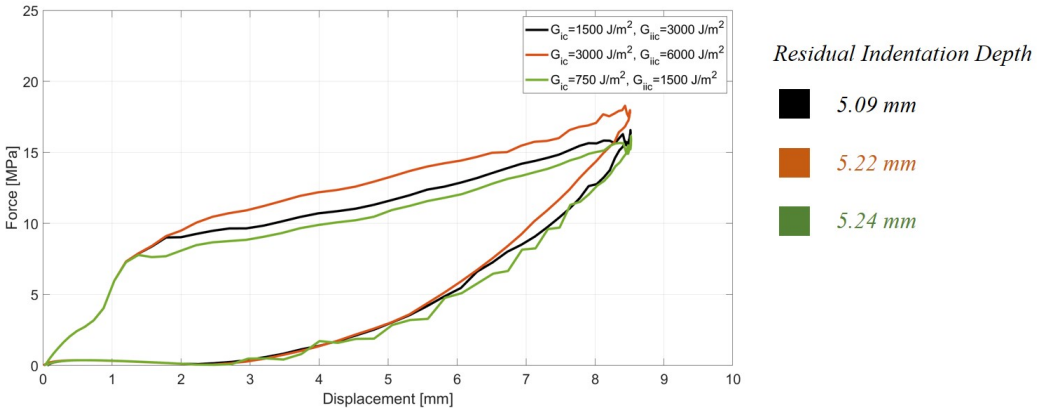

Figure 6.7: FE force-displacement behaviour of a Type III cylinder with different metal-composite interface properties

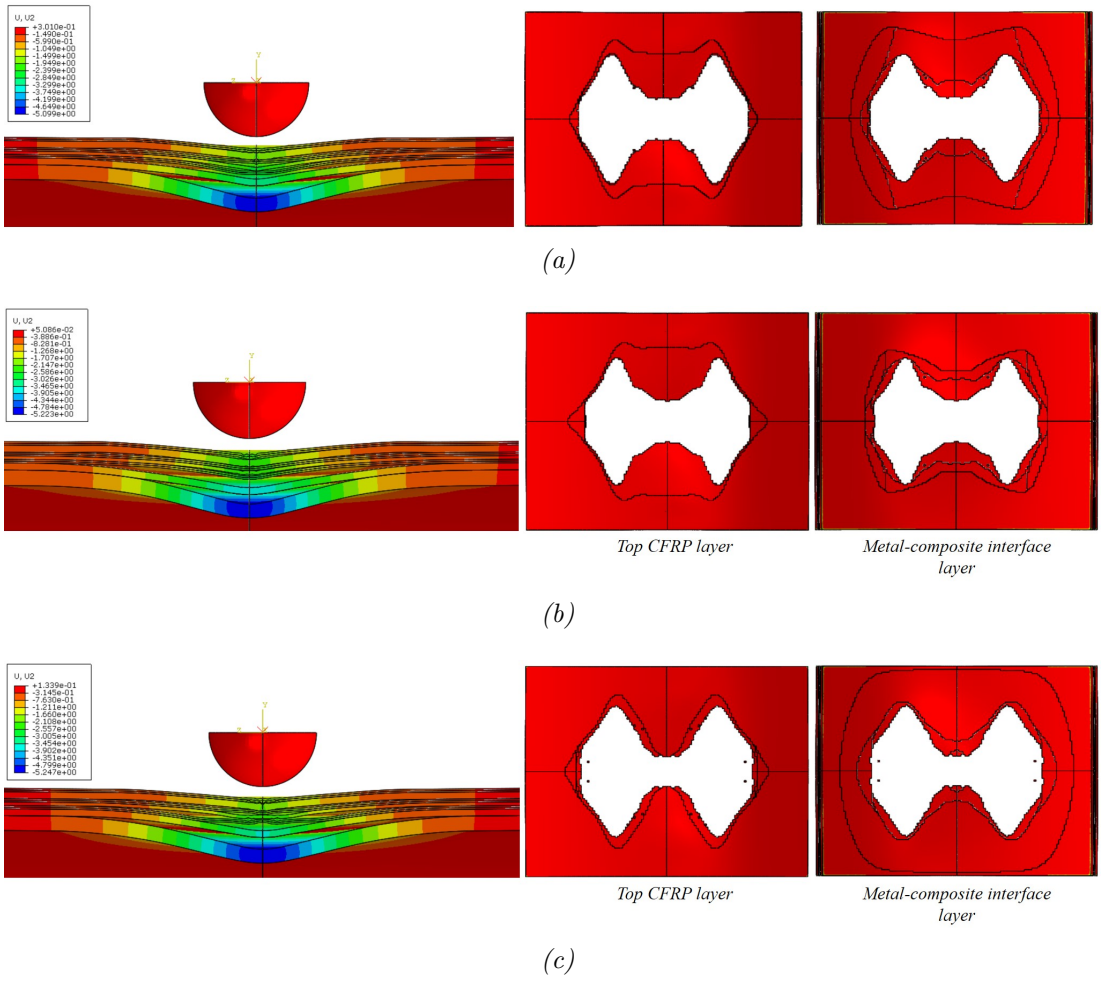

Figure 6.8: FE residual dent and delamination contours of a Type III cylinder with different metal-composite interface properties; a) Baseline interface; b) Higher interface toughness c) Lower interface toughness

Table 6.7: Delamination area comparison of a Type III cylinder with different interface toughness parameters

Model	Metal-composite interface		
	a	b	Area $[mm^2]$
Baseline	29.6	22.3	2073.7
Higher interface toughness	24.9	14.1	1102.9
Lower interface toughness	32.1	29.4	2964.8

6.3.3 Material thickness ratio investigation results

Figure 6.9 shows the F-d comparison of the two different design proposals: one with thick liner/thin composite wrap and one with a thick liner/thin composite wrap. The former was denoted as dent tolerant and the latter as dent resistant. Based on the results, it is not obvious that there is a damage tolerance design advantage from modifying the baseline specimen design as it can only be observed that there is an increase of stiffness in the thick-liner cylinder which would increase damage resistance, however the dent depth measurement shows no significant differences between each design. Having a thick-liner cylinder would generate higher surface strains and, hence, lower expected fatigue life. However, the thick liner also might increase fatigue life as it may not have large deflection under pressurisation. Thus, stress distribution on the indentation region and residual plastic strains are also analysed for these designs to investigate the liner's behaviour in each case.

Figure 6.10 shows the residual plastic strain in the aluminium liner for both designs (thin and thick liner). The results indicate a more localised indentation and that higher levels of plastic strain are found in the thicker liner whereas the thin liner model shows a larger deformation area. Moreover, Figure 6.11 shows hoop and longitudinal strains in the liner as well as the damage incurred in the composite layers of each design. It is also possible to observe a more localised indentation in the thicker liner with higher composite damage. Conversely, the thin liner shows a lower level of plastic strain around the indentation but the extent of delamination is larger. Giving that the thin liner shows lower levels of residual plastic strain after one pressure cycle, it is thought that this design proposal could be more suitable for damage tolerance purposes. Figure 6.12 shows the Von Misses, hoop and longitudinal stress distributions on the liner. These stress distribution will be modified during a fatigue life cycle, thus, it is not possible to assess post-impact fatigue life based on them. However, the stress distribution may have an effect on the damage resistance of the structure and this result offers the possibility to evaluate, at basic level, this information.

It is clear that the design of an actual commercial cylinder responds to a collection of performance and manufacturing considerations. As such, simulations performed here do not aim to propose a novel design for Type III cylinders

but to show the analysis capabilities that can be achieved using the FE model developed in previous chapters. For instance, it is clear that the thick cylinder proposal would not represent an efficient design for total weight and burst pressure, as shown in Section 6.2.3. However, with this model it was possible to observe the extent of damage resulting from having different materials and different thicknesses ratios. Results in this section show different possibilities to analyse the indentation development on a Type III cylinder, such as strain and stress distributions, which are not possible to observe from an experimental test. Hence, the model could be used to explore a wide range of ideas as part of the engineering design process.

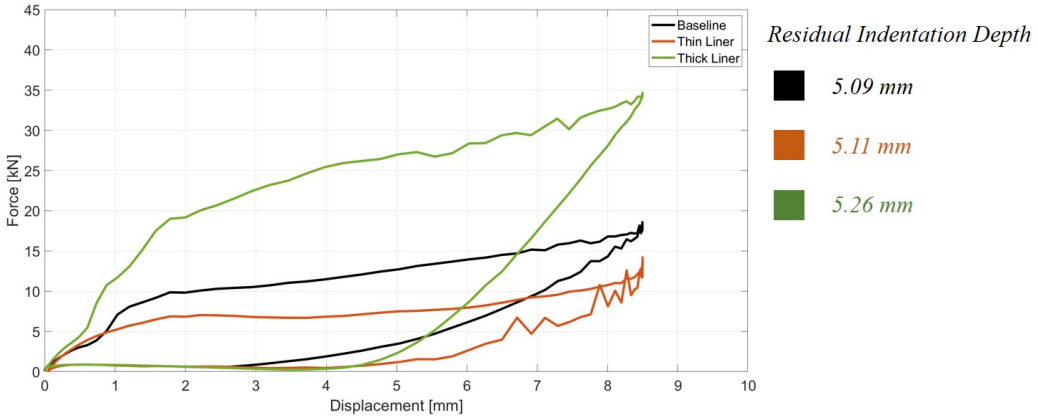

Figure 6.9: FE force-displacement behaviour of a Type III cylinder with different thickness ratio of materials

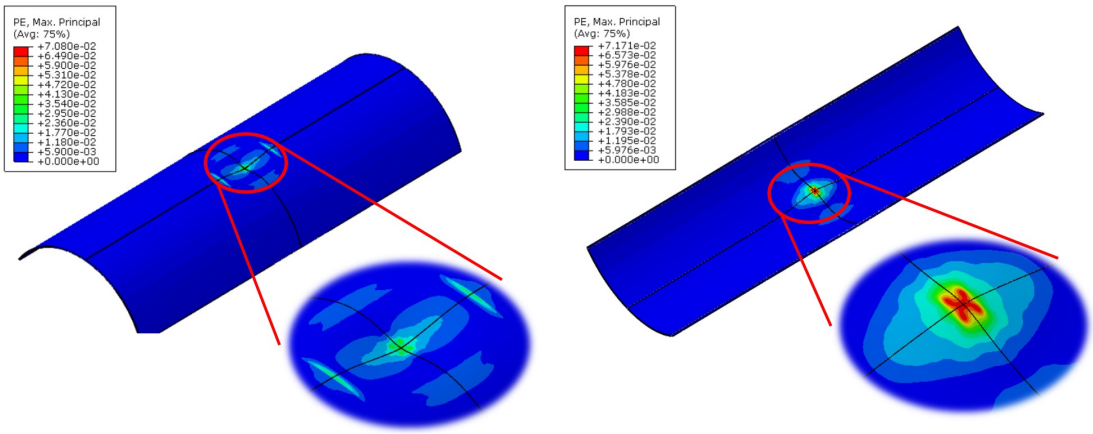

(a)

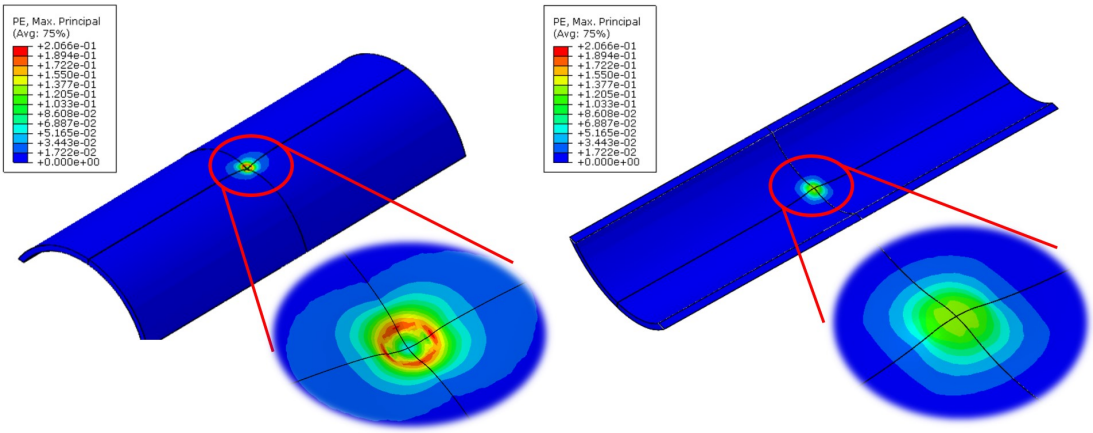

(b)

Figure 6.10: FE residual strain distribution on different-thickness liner of Type III cylinder; a) thin liner, b) thick liner

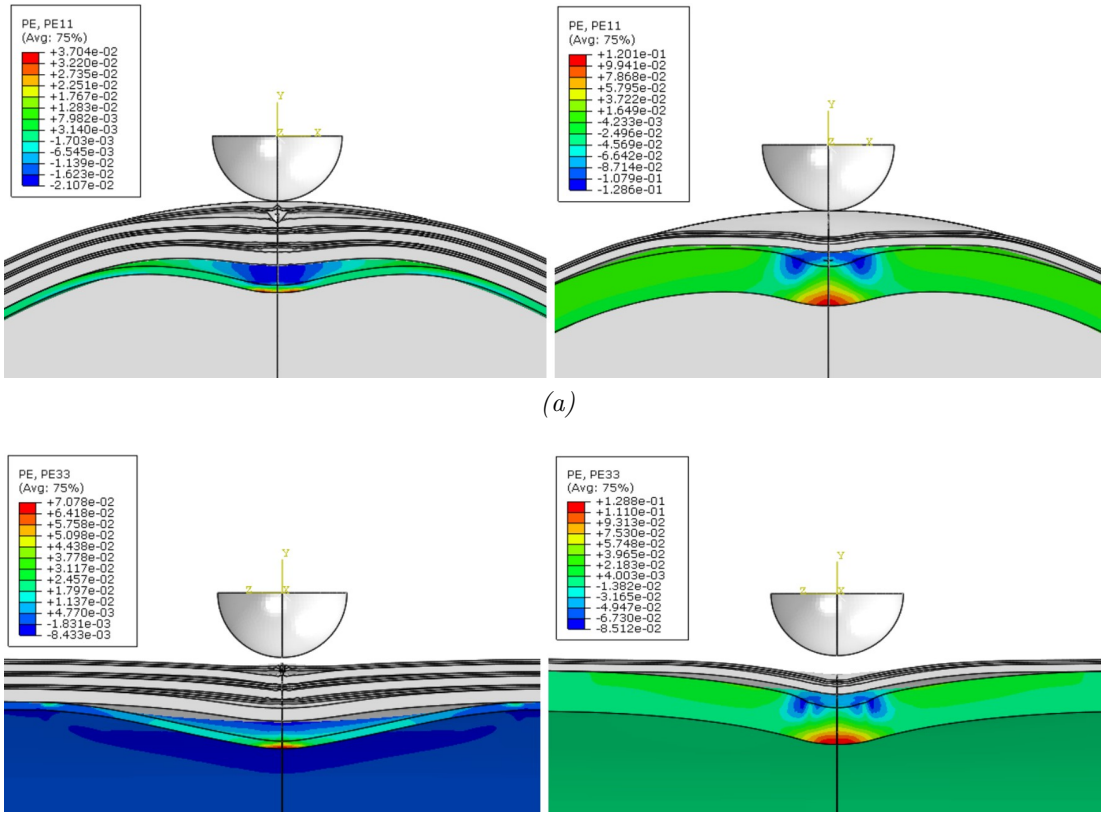

Figure 6.11: FE residual plastic strain distribution on different-thickness liner of Type III cylinder; a) hoop strains, b) longitudinal strains

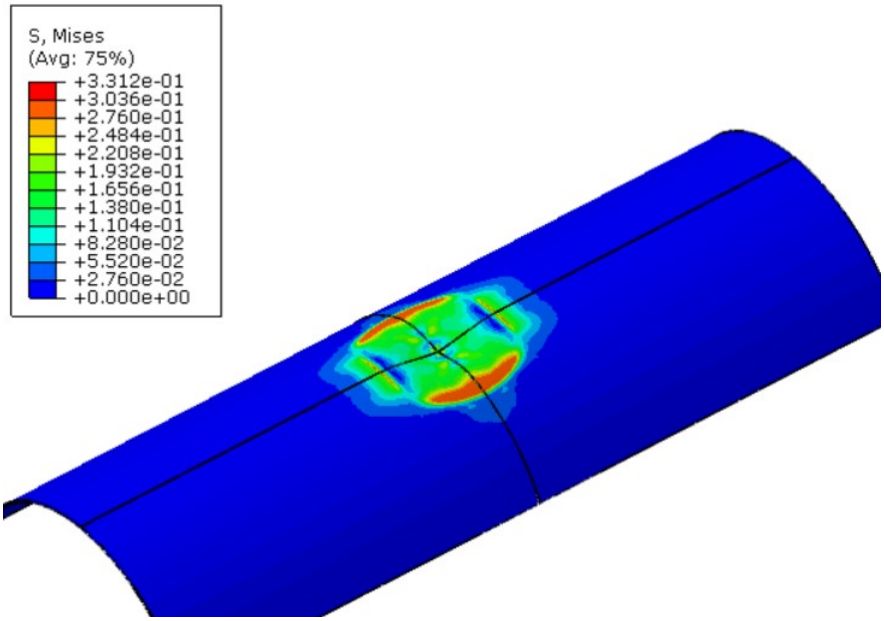

(a)

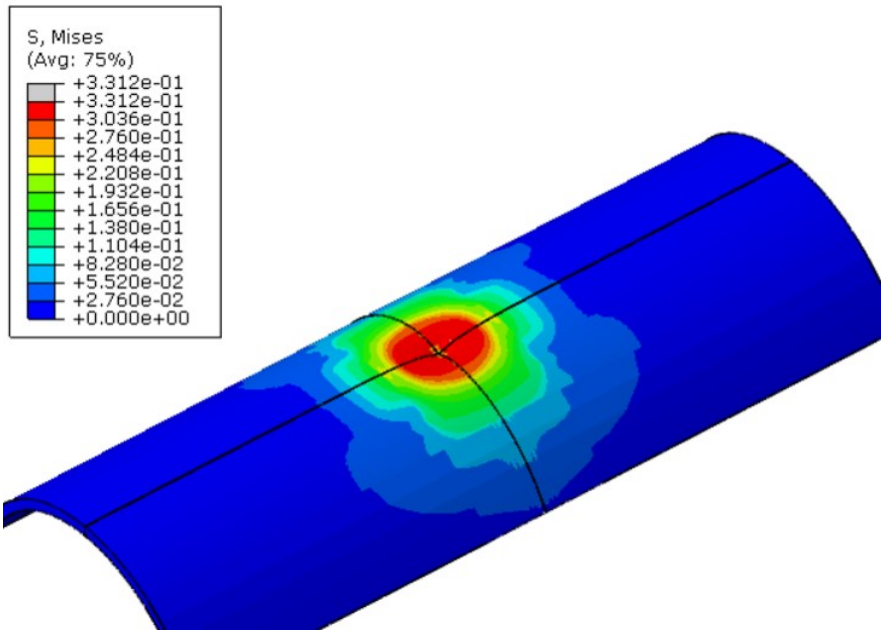

(b)

Figure 6.12: FE residual Von Mises stress distribution on different-thickness liner of Type III cylinder; a) thin liner, b) thick liner

6.3.4 Effects of internal pressure on dent depth development results

6.3.4.1 Pre-indentation pressurisation

Figure 6.13 shows the comparison of F-d curves of a Type III cylinder indented under different internal pressurisation levels. The figure indicates that at higher levels of pressurisation the overall stiffness of the structure and the peak force increases. Furthermore, it is also observed that higher levels of internal pressurisation contribute to a reduced indentation residual depth. This result suggests that an empty cylinder is more prone to larger deformation of the metal liner than a cylinder at service pressure.

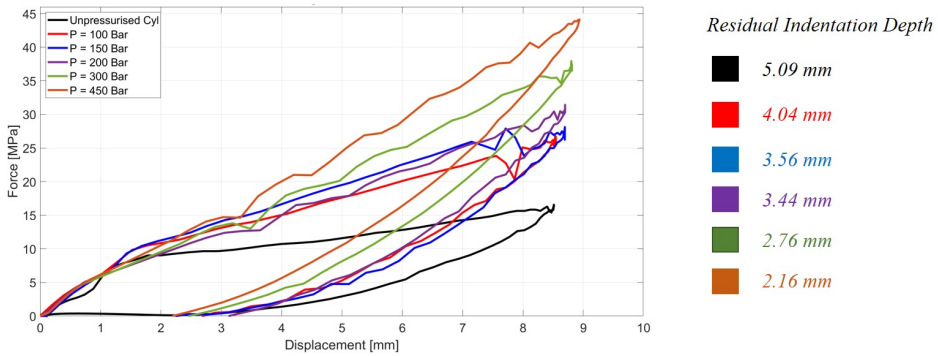

Figure 6.13: FE force-displacement behaviour of a Type III cylinder under quasi-static indentation with different internal pressure values

The effect of the internal pressure on delamination propagation at the metal-composite interface was also investigated. Figure 6.14 shows a top view of the cohesive element region used to simulate the metal-composite interface of the cylinder under different internal pressure values. According to this result, it is noticeable that the area of delamination is reduced with increased internal pressure. The most significant difference in delamination area is observed at 30 MPa, which is approximately the service pressure of a cylinder similar to Model A. Thus, results suggest that a Type III cylinder subjected to LVI might be significantly less damaged at service pressure compared to an empty cylinder. This result should be interpreted cautiously, as there is also the possibility that other failure mechanisms might become active, including fibre failure.

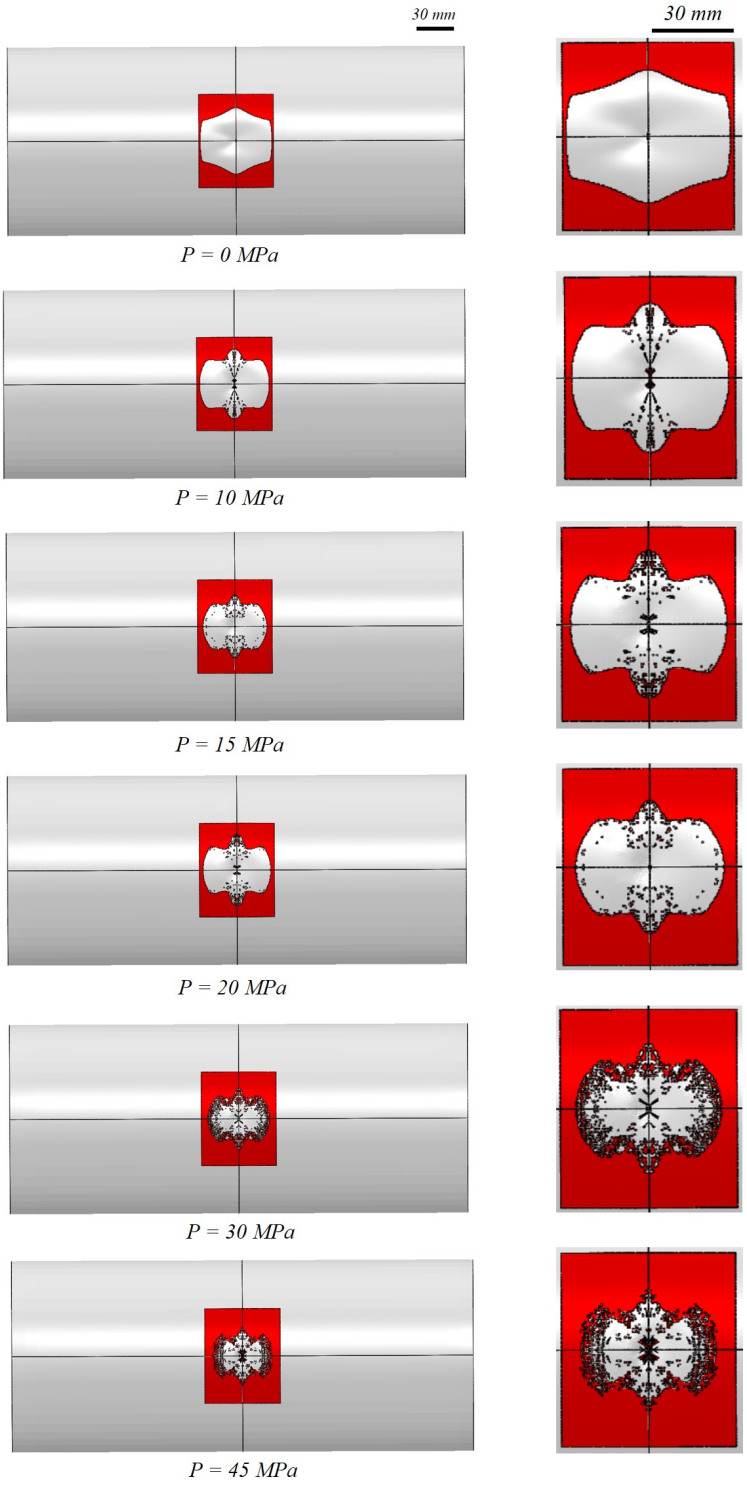

Figure 6.14: FE metal-composite delamination of a Type III cylinder under quasi-static indentation at different internal pressure values

6.3.4.2 Post-indentation pressurisation cycles

As described in Section 6.2.4 post-indentation pressurisation simulations were performed to investigate the effect of metal deformation after indentation under internal pressure load. No F-d curves figures are presented in this section as the pressure is applied after indentation. Previous experimental testing and CT examination presented in [2] showed that post-impact pressurisation in the cylinder induced a reduction of the residual dent depth. Two different post-indentation pressurisation cycles were created. The first cycle aimed to identify the pressure at which the dent deforms plastically back towards the CFRP and closes the gap between both materials. Figure 6.15 shows the deformation progress of the dent during internal pressure application. The maximum displacement is reported at the inner surface of the liner. From 0 to 6 MPa there is a reduction of the dent depth of $\approx 32\%$ which is a considerable reduction given the low pressure, however at this pressure there is still a noticeable separation between the materials. At 12 MPa the dent depth reduces by up to $\approx 60\%$ and the dent is still noticeable. From 18 to 24 MPa the maximum dent depth reduction increases to $\approx 78\%$. Finally, at 30 MPa the dent depth is 0.77 mm which makes the dent more difficult to notice, although it is observed that it is not fully closed.

In the second pressure cycle, the aim was to observe the residual dent behaviour after pressure release. Figure 6.16 shows the residual dent and the plastic strain distribution in the liner in three different stages: after quasi-static loading, after pressure application (30 MPa) and after pressure release. This result also shows that at 30 MPa the gap between the two materials is not completely closed as the liner recovers its original shape only partially. However, after pressure release it is observed that there is some metal springback and the residual dent depth is 2.54 mm, which is $\approx 50\%$ less than predicted residual dent before pressurisation. This behaviour is consistent with that reported in [2] in which CT imaging was used to measure the dent depth before and after pressurisation. Furthermore, Figure 6.16 shows the strain fields at the dent development. Considering that Type III cylinders perform under a low cycle fatigue regime, strain values at the dent are of particular interest as they are the driving mechanism for fatigue behaviour in that regime. As such, the difference in plastic strain, between the state of maximum pressurisation (6.16b) and the state of pressure

release (6.16a), could be used for further fatigue life analysis.

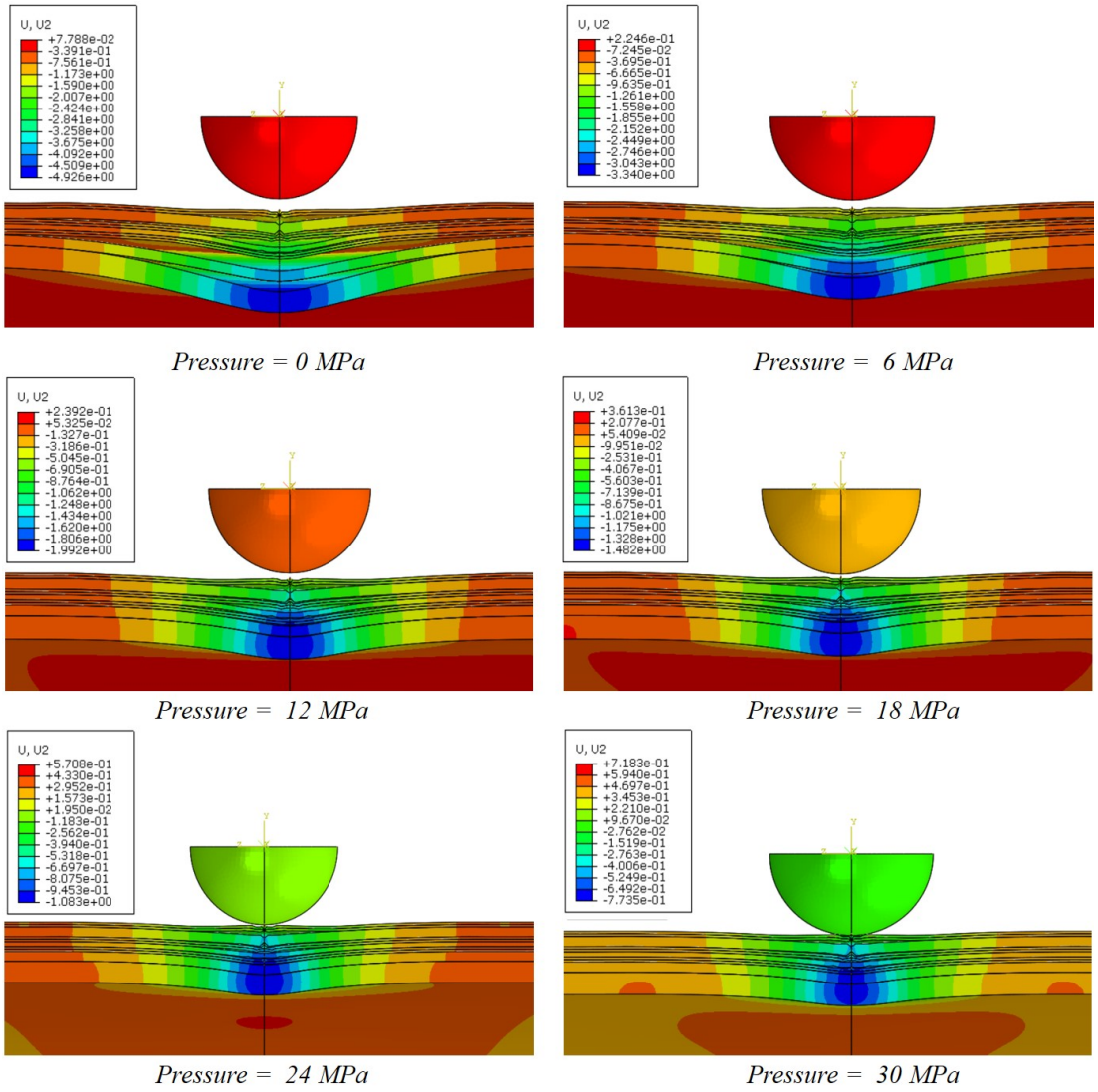

Figure 6.15: Dent deformation prediction under internal pressurisation

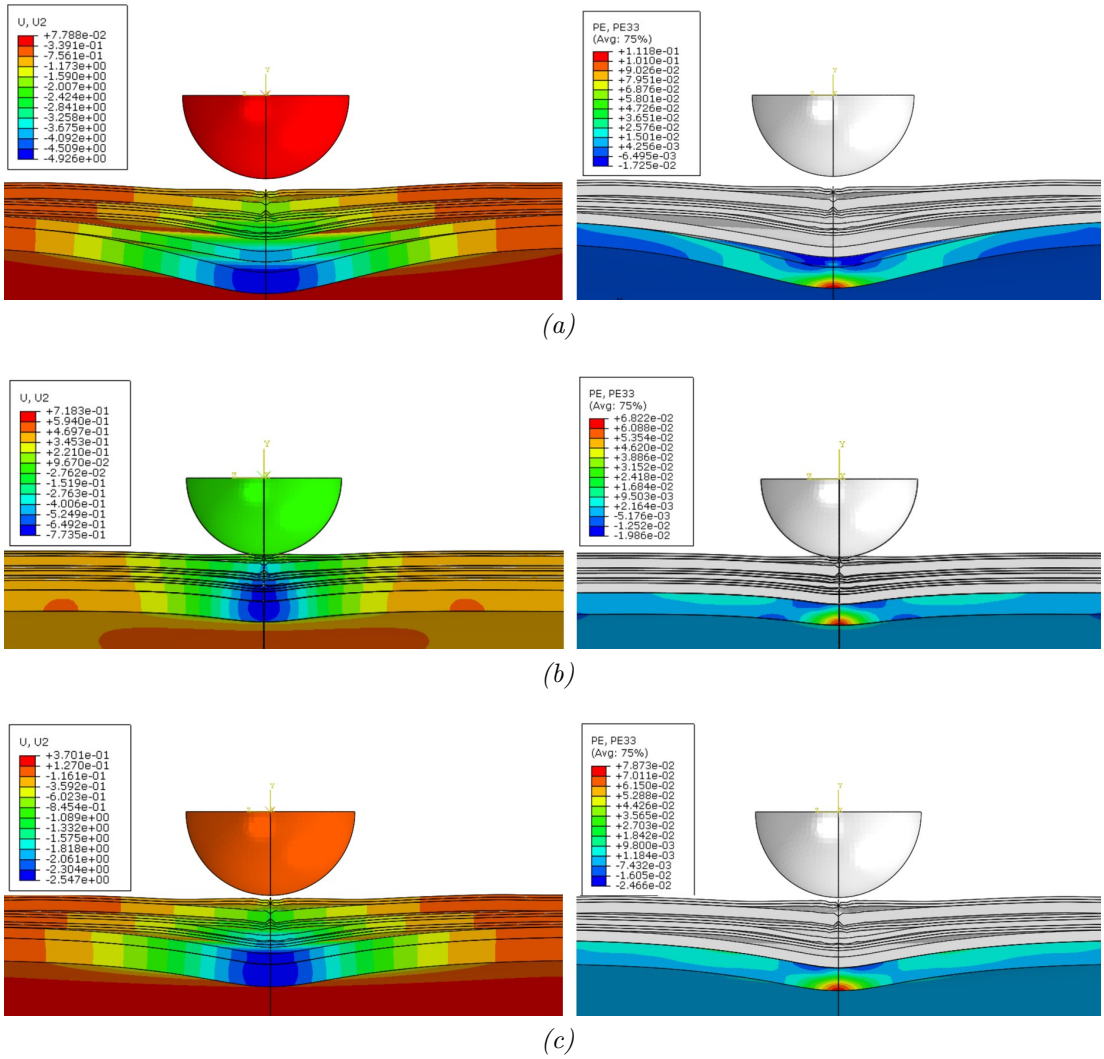

Figure 6.16: FE residual dent depth and plastic strain distribution at different loading stages; a) after quasi-static load removal, b) after 300 bar internal pressure application, c) after pressure internal removal

6.4 Summary and conclusions

This chapter presented a 3D FE model which was used for parametric investigation. Different design modifications were made to the cylinder to observe the effect of each of them on the residual dent depth after quasi-static loading. The model was proved to have advantages for design enhancement investigation comparing to pure experimental investigation. For instance, the effect of changing liner and composite wrap materials was investigated. Results showed that, there are significant differences in the peak force result when performing material changes, however this is not the case for residual dent depth. Thus, despite the overall structural stiffness increment, the residual dent depth remains similar. Furthermore, delamination results suggest that there is no significant change achieved when using different materials on each part of the cylinder. Overall, it was concluded that modifying materials are unlikely to result in a significantly better damage tolerance behaviour for the cylinder, although, it may increase or reduce other characteristics such as damage resistance. However, it was noticed that this behaviour is only applicable for displacement controlled conditions and that more significant differences may be observed when the loading is force or energy controlled instead. Similarly, regarding the metal-composite interface change, it was concluded that no significant change in the F-d response and residual dent depth can be achieved through interface property modification. However delamination areas are significantly reduced when the interface properties increased. Therefore, it is suggested that increasing the metal-composite interface properties could lead to an increase in damage resistance of the cylinder.

Regarding the proposed theoretical thin liner (dent tolerant) vs thick liner (dent resistant) cylinder models conclusions have been also achieved. Firstly, a thicker metal liner does not necessarily imply enhanced behaviour as the dent depth has been shown to be similar to the baseline and thin liner cylinder models. However, stress and strain distribution at the vicinity of the indentation exhibited obvious differences between both models. With this result, it was shown that the model capabilities to analyse the dent not only through its depth, but also by interpreting the stress and strain contours, which offers important information for design decision making. For instance, a higher, more concentrated residual

stress distribution around the indentation could lead to a more significant cyclic plastic strain and, as a result, fatigue cracking.

Finally, the model was used to investigate dent behaviour under internal pressure loading before and after quasi-static indentation. Results showed that performing quasi-static indentation whilst adding internal pressure to the cylinder leads to dent depth and delamination reduction. Hence, it is suggested that a Type III cylinder subjected to a LVI with internal pressure might suffer considerably less damage than an unpressurised cylinder. Similarly, re-pressurisation after quasi-static indentation results suggested that at ≈12 MPa the aluminium starts exhibiting a significant reduction of the dent depth.

Overall, this chapter demonstrated through a series of design modification activities, that the use of the FE model developed as the major contribution to this thesis project provides an interactive tool for cylinder design as many different results can be obtained from one single simulation that can be compared to several simulation values. The results from this model could readily be incorporated in overall design optimisation work, in combination with assessments of manufacturing, cost, burst pressure and required life. One possible difficulty presented by this model is the computational time required to solve each model iteration, which is ≈27 hrs using 32 CPU. Therefore, degree of freedom reduction in the model is suggested, *e.g.* using continuum shell elements, shell elements or geometry reduction ($1/8^{th}$ of the cylinder). Moreover, the design options proposed in this chapter have been explored without considering manufacturing costs, which in practice should be considered as part of the product design cycle. Additionally, it is also recommended to perform simulations according to the requirements described in Chapter 2, *i.e.* cylinder dropping, considering an explicit dynamic impact model.

Chapter 7

Conclusions and future work

7.1 General conclusions

A unique full 3D FE model of a Type III cylinder has been developed, validated and presented in this thesis. The aim of this model was to predict the residual indentation developed in the liner after quasi-static load application, as this had previously been shown to correlate strongly with the post impact fatigue. Furthermore, this model was used to investigate this damage mechanism under different loading conditions (*e.g.* the effect of internal pressure), which has not been developed hitherto. It was demonstrated that the model exhibits good agreement to experimental results and it maintains reliability under geometric, material and boundary condition modifications, which makes it applicable for optimisation purposes. The findings obtained as a result of the development of this model are presented in this section.

- Model validation was performed using a calibration methodology based on experimental-model comparison of a 2D line indentation of a hybrid metal-composite structure known as a ring specimen. The specimen was intended as an intermediate building block to allow improved understanding and design of Type III cylinders. Forced-displacement curves showed good prediction of the initial elastic response of the structure compared to the experimental response. Furthermore, based on local strain measurmeents, it was shown that the model can predict the residual indentation on the ring spec-

imen with a difference of 6%. Therefore, based on force-displacement and local strain distribution comparison, it was demonstrated that the methodology to develop the ring specimen FE model was acceptable.

- Cohesive elements embedded in the ring model were used to investigate the parameters governing the metal-composite interface within a Type III cylinder, between the aluminium liner and the CFRP wrap. Using the traction-separation law that determines the cohesive element behaviour, an estimation of the interface parameters was developed through parametric calibration. Model-experimental comparison suggested that the estimated values for the metal-composite interface are in good agreement with experimental results.

- It was demonstrated that the interface parameters estimated through the ring specimen activities were transferable to full Type III cylinder model without any further calibration required.

- It was reported that modelling delamination on the CFRP layers of the cylinder has a significant effect on the residual indentation results, specially for cylinders in which of the wrap is thicker than the liner.

- It was shown that the methodology to develop the full Type III FE cylinder model was applicable for more than one pressure vessel geometry as shown by the models A, B, C and D, introduced on Chapter 5. For each model the difference between the predicted and experimental peak force was 7%, 20%, 6.2% and 28%, which are acceptable considering the level of damage occurring in the model.

- It was shown that the residual indentation results from the FE model are in good agreement to what is reported in [2], having a difference of 15.2% between the predicted and experimental residual depth. With this model, it was also possible to observe the extent of delamination within the metal-composite layers and its relation to the residual dent development.

- It was shown that optimisation can be performed using the full FE Type III cylinder model. This conclusion was obtained by developing parametric

investigation activities using the model. Results indicated that, for the quasi-static load boundary condition, modifying liner materials from an Al-6061 to Al-7075 or TiAl6V4 has no significant effect on the residual dent result. Similarly, modifying the wrap material does not contribute to a significant reduction of the residual dent, however it does reduces the level of delamination on the metal-composite interface.

- Modifying liner and composite wrap thickness ratio showed the model capabilities to investigate the stress and strain distribution in the vicinity of the indentation. It was concluded that a thicker liner does not reduces the depth of the residual dent, but induces a higher concentration of stresses at the dent, which can lead to other damage mechanisms such as fatigue cracking.

- Using the full cylinder model, the residual dent and delamination extent were investigated under internal pressure loads. Results indicated that increasing the level of internal pressure during the indentation contributes to a reduction of the liner dent. Similarly, post-loading pressurisation simulations showed the pressure at which the residual dent starts to reduce and close the gap between the liner and the composite wrap. Results also showed that there is an increment of the residual stresses in the indentation region.

Overall the research conducted in this project and presented in this thesis has achieved the primary goals stated at the outset. A capable modelling for the quasi-static transverse indentation response of type III gas cylinders has been developed and validated.

7.2 Future work

Given the successful development of the modelling capability described in this thesis, there are clear future directions that could be productively explored. Thus, further activities are recommended using the full cylinder model, focusing on product optimisation and considering different factors such as post-impact fatigue

behaviour, burst pressure and weight reduction. Moreover, as mentioned in the expected outcomes of this research, an EngD project requires an industrial benefit additional to the academic contribution. Thus, some of the recommendations given in this section focus on the implementation of the cylinder model within an industrial product design process.

- Develop further modelling activities to use the FE model to perform impact analyses. This would include drop weight impact on cylinders as well as whole cylinder drop tests. It has been reported that the use of cohesive elements under impact simulations requires a rate-dependant behaviour [144–146]. Thus, further research and validation may be required to implement such effects in the current full cylinder model to use an impact load instead of a quasi-static load.

- Reduce full cylinder model computational time. Optimisation activities often require a single model to perform several iterations to find the optimum design (based on specified requirements *e.g.* minimum weight). Hence, it is recommended to explore further reduction of the model's degrees of freedom. For instance, the use of shell elements to reduce computational time could be a potential solution to obtain good and faster results that allows more efficient optimisation simulations.

- Extend design possibilities to be simulated using the full cylinder model for optimisation purposes. Chapter 6 presented different modifications to the current pressure vessel design to demonstrate optimisation capabilities. Nonetheless, it is suggested to extend the modelling with more design possibilities, for instance larger cylinders are of considerable interest, different combinations of fibres and/or different cylinder structures that delay the composite damage propagation in order to reduce the liner residual dent (e.g. composite sandwich-like structures or internal honeycomb structures [147]).

- Extend the methodology used to develop the current model to other cylinder types, such as Type IV cylinders. Type IV cylinders are also being investigated for use in similar applications as Type III, hence using FE

modelling to investigate the interface existing between the polymer liner and the composite wrap could be beneficial for such designs.

Appendix A

The following images were used to perform point measurements through the loading and unloading steps of the ring specimen compression test. Additionally, the images show damage development during the experiment. Images were processed using Matlab.

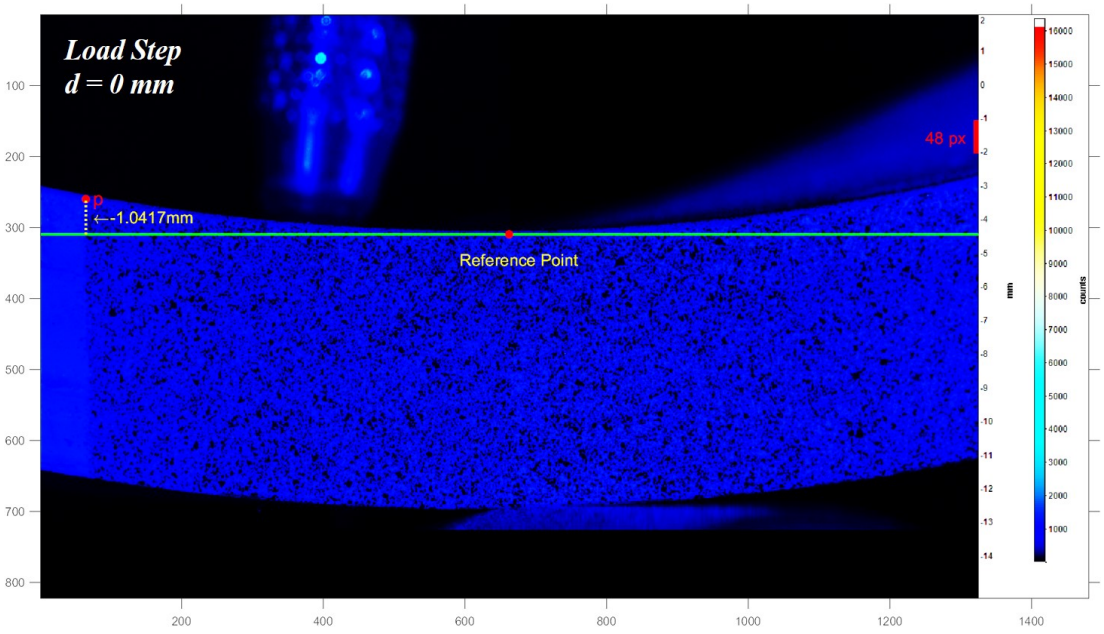

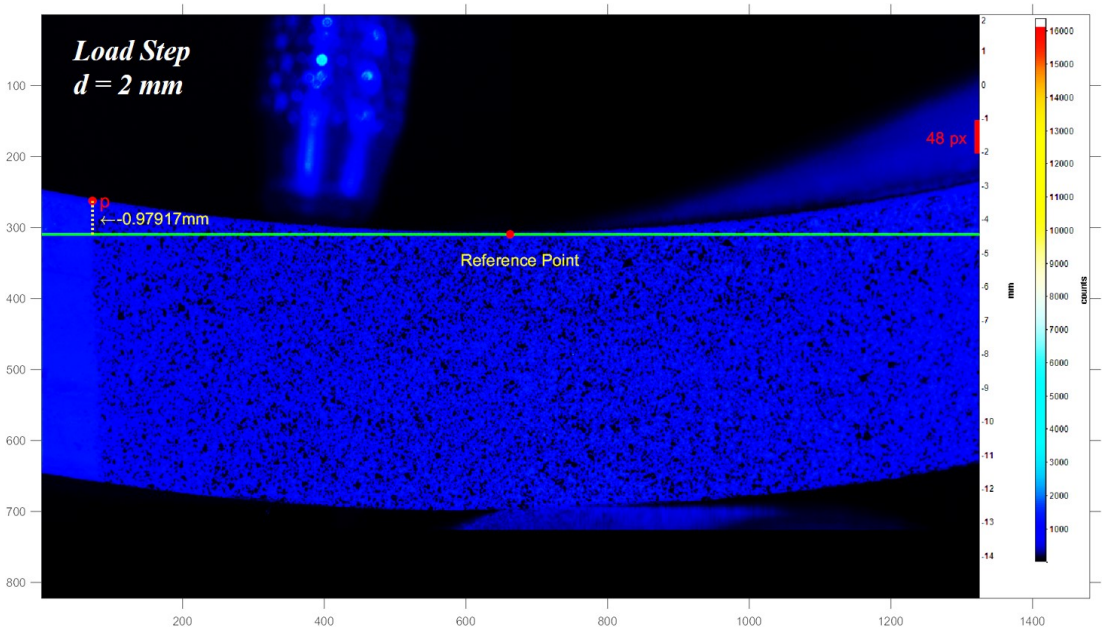
Load Step
d = 2 mm
48 px
p
←-0.97917mm
Reference Point
mm
counts

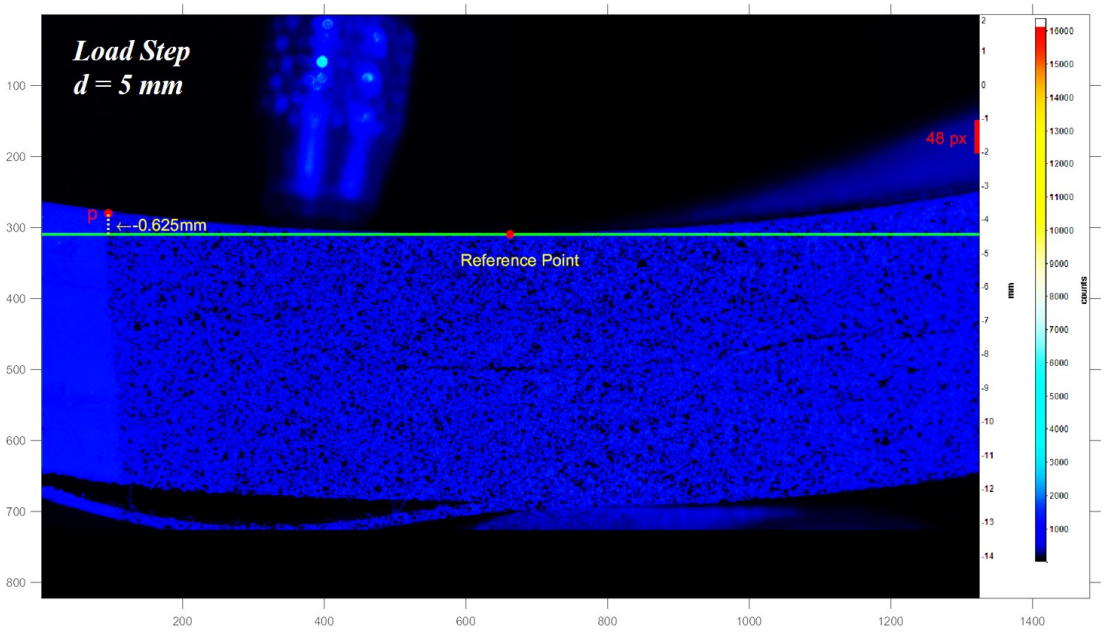
Load Step
d = 5 mm
48 px
p
←-0.625mm
Reference Point
mm
counts

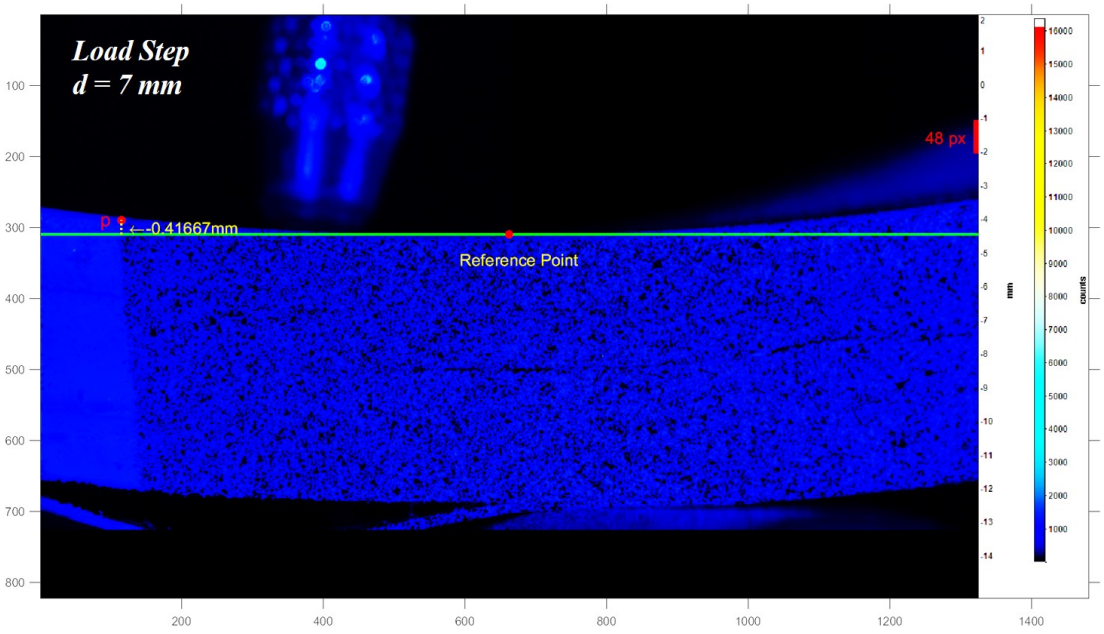
Load Step
d = 7 mm
48 px
←-0.41667mm
Reference Point
mm
counts

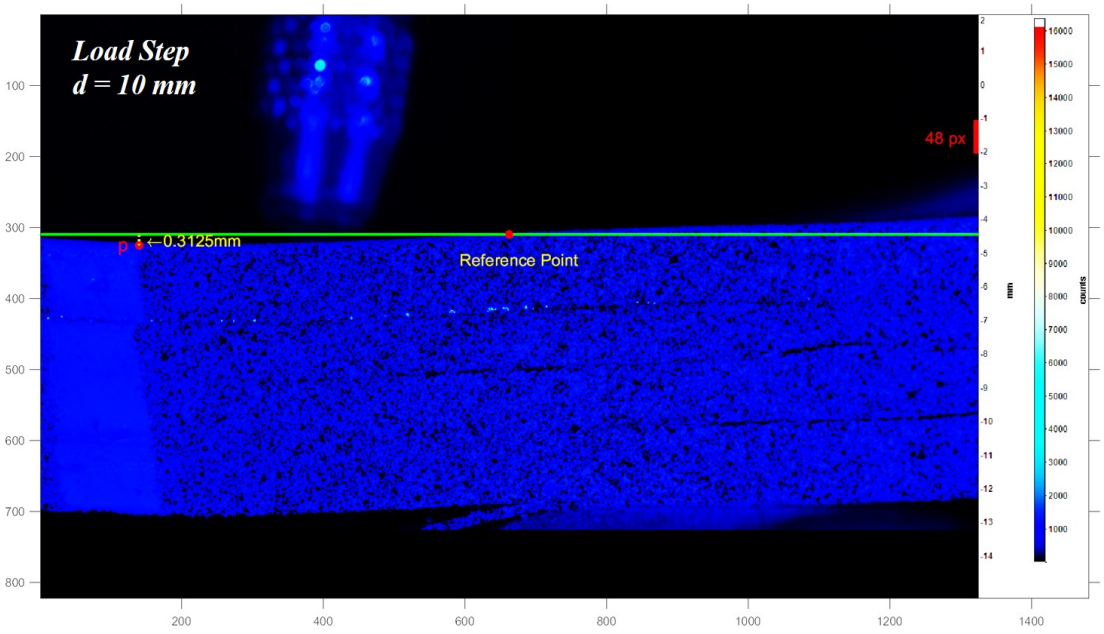
Load Step
d = 10 mm
48 px
←0.3125mm
Reference Point
mm
counts

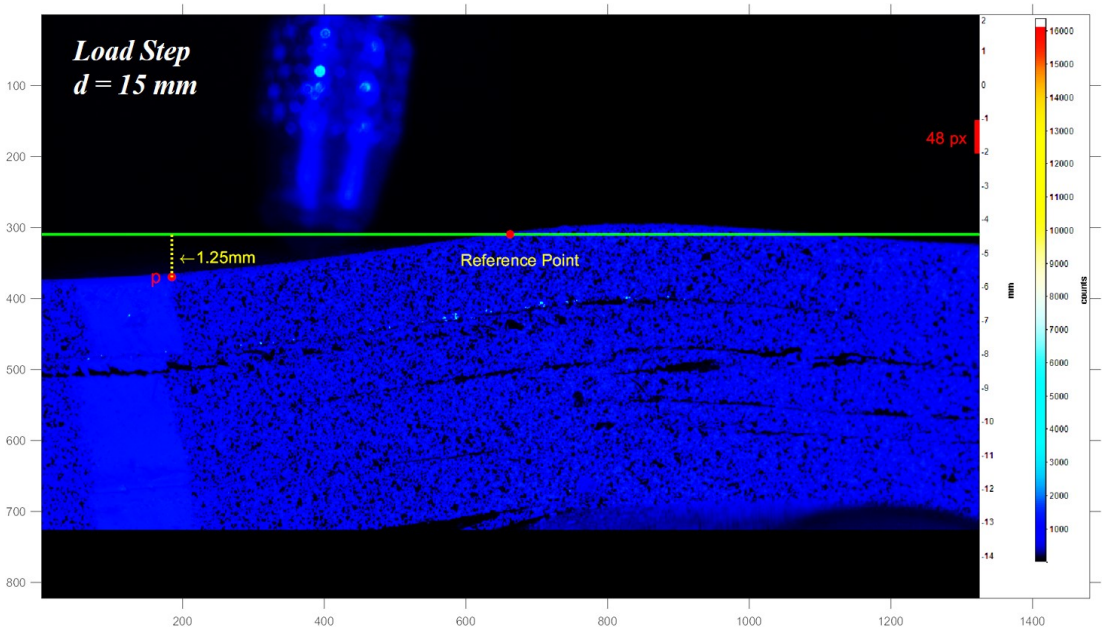
Load Step
d = 15 mm
48 px
←1.25mm
p
Reference Point
mm
counts

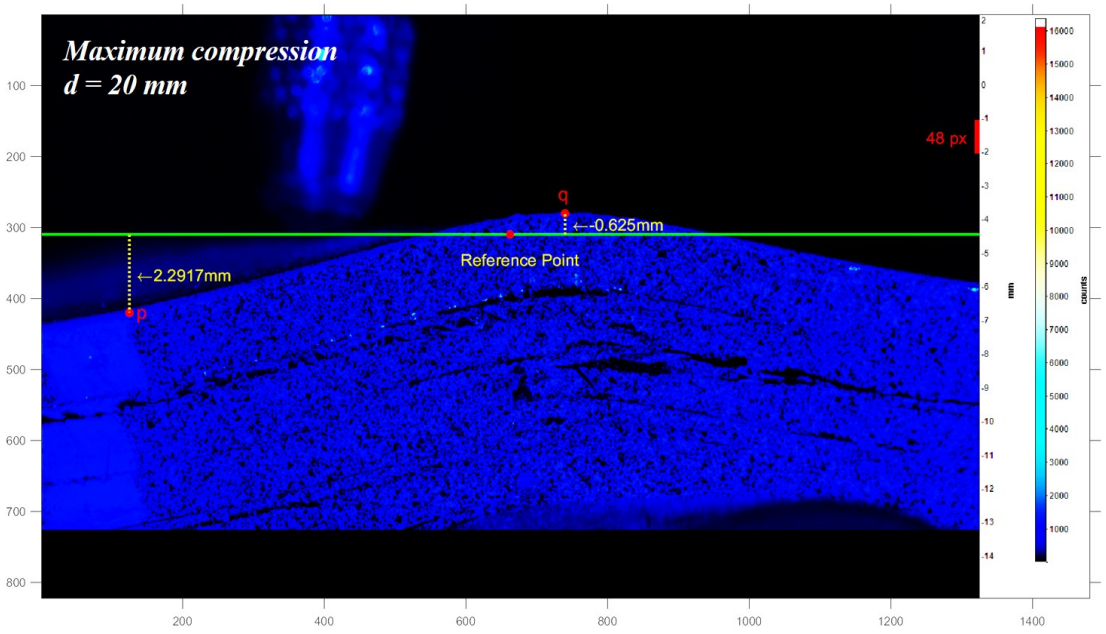
Maximum compression
d = 20 mm
48 px
q
←-0.625mm
Reference Point
←2.2917mm
p
mm
counts

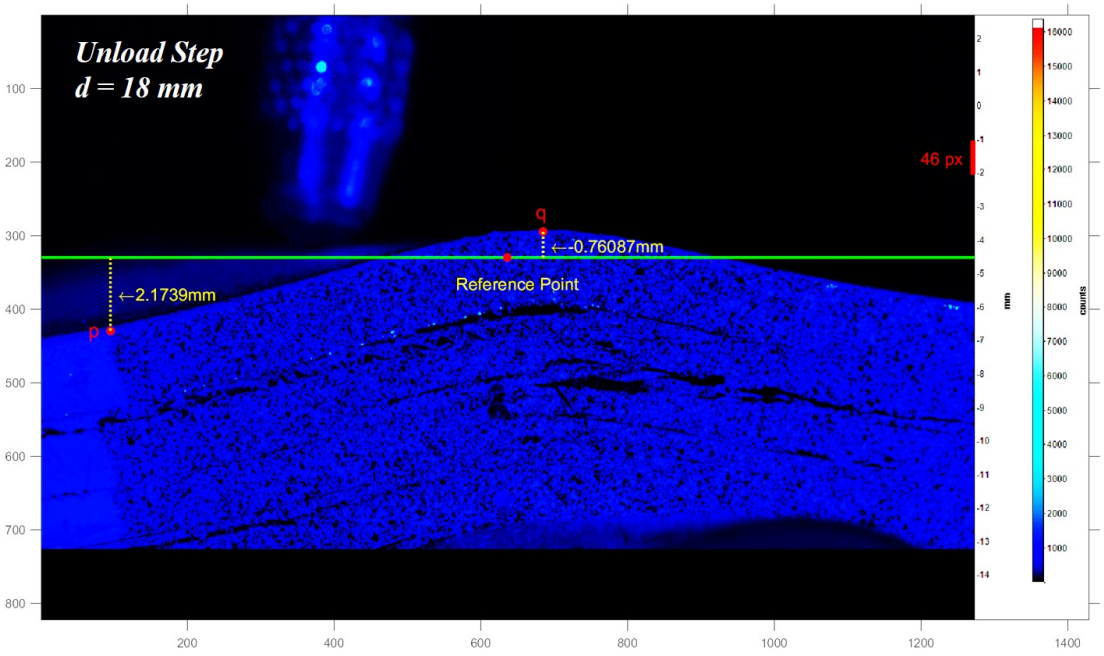
Unload Step
d = 18 mm
46 px
q
←-0.76087mm
Reference Point
←2.1739mm
p
mm
counts

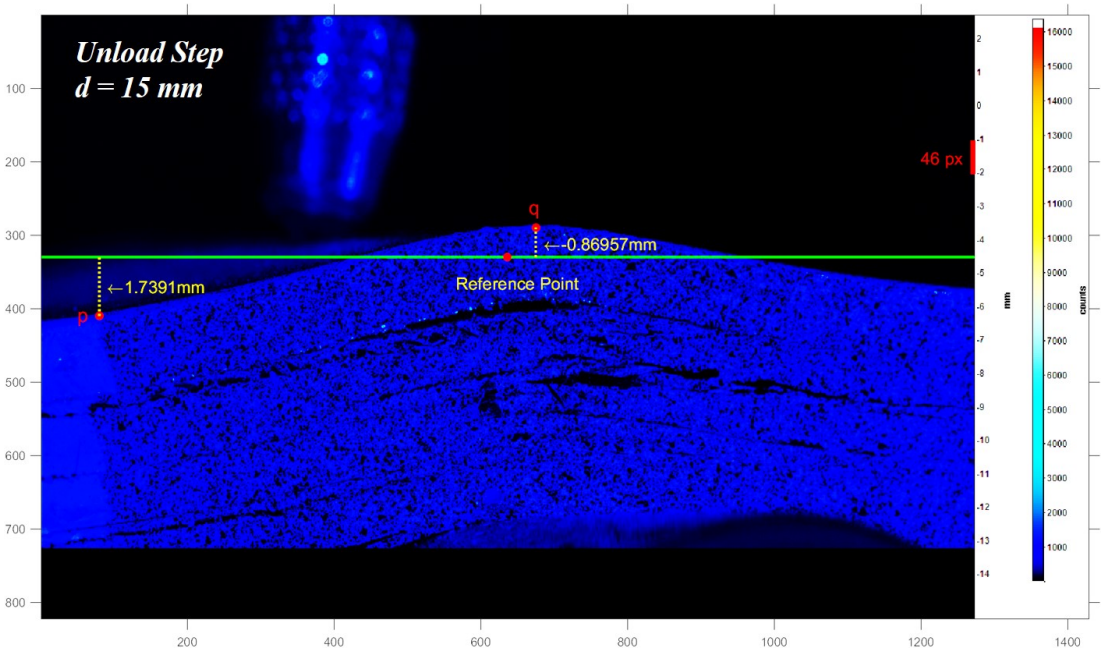
Unload Step
d = 15 mm
46 px
q
←-0.86957mm
Reference Point
←1.7391mm
p
mm
counts

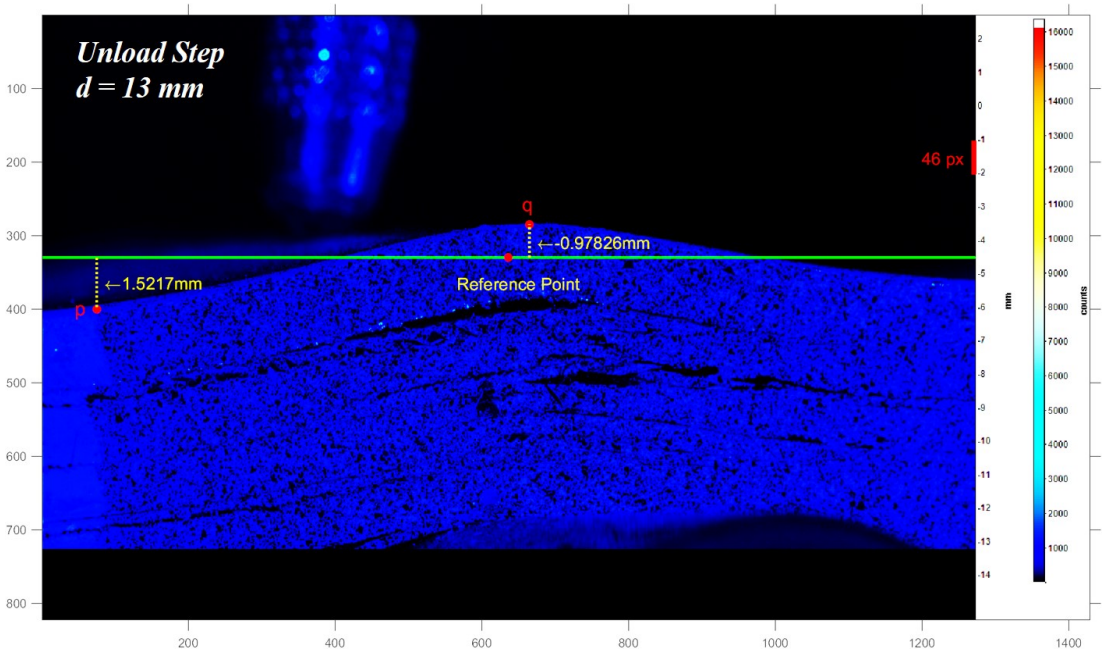
Unload Step
d = 13 mm
46 px
q
←-0.97826mm
←1.5217mm
Reference Point
p
mm
counts

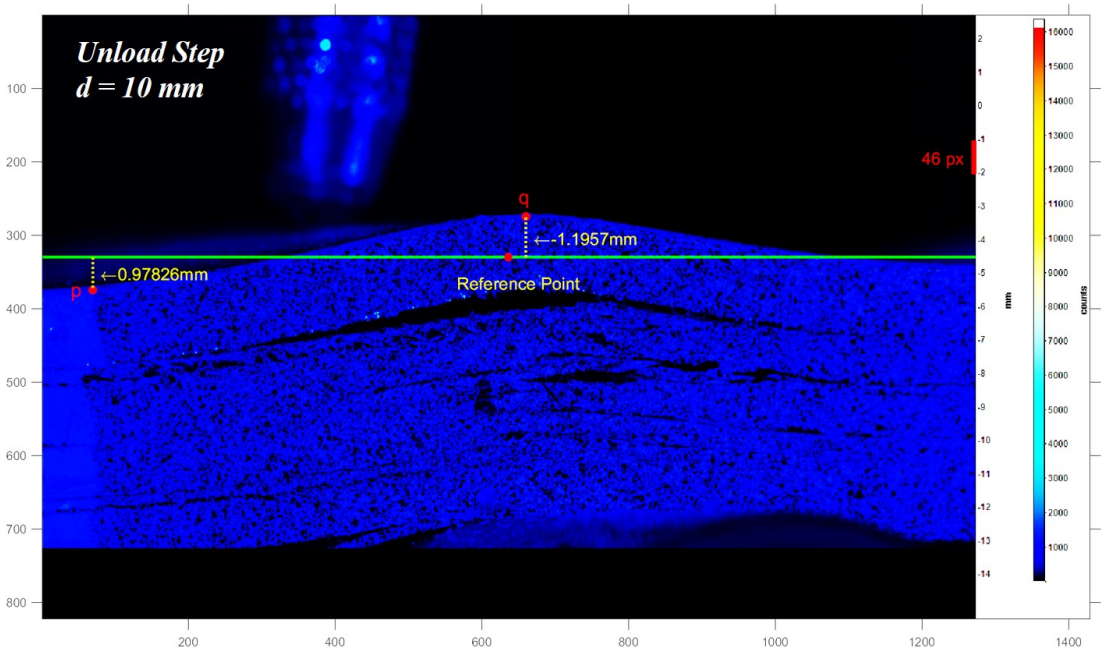
Unload Step
d = 10 mm
46 px
q
←-1.1957mm
←0.97826mm
Reference Point
p
mm
counts

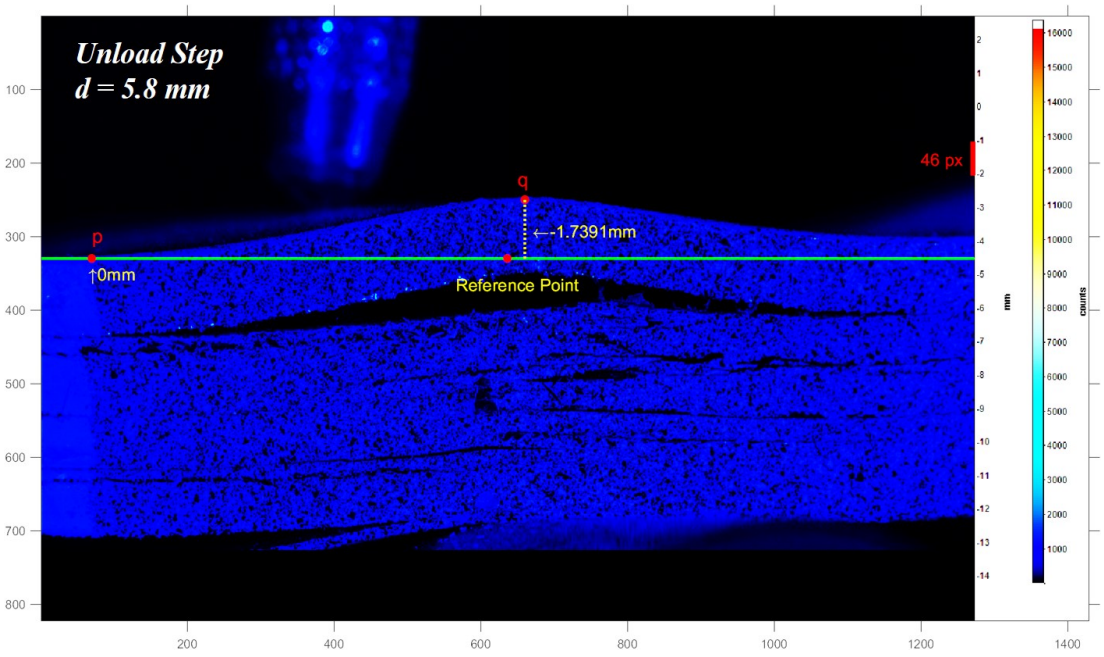
Unload Step
d = 5.8 mm
46 px
q
←-1.7391mm
p
↑0mm
Reference Point
mm
counts

Bibliography

[1] R.-M. Wang, S.-R. Zheng, and Y.-P. Zheng, "Introduction to polymer matrix composites," *Polymer Matrix Composites and Technology*, pp. 1–548, 2011. DOI: 10.1533/9780857092229.1.

[2] T. M. Allen, "Damage Development and Post-Impact Performance of Composite Overwrapped Pressure Vessels Subjected to Low Velocity Impact," Ph.D. dissertation, University of Southampton, 2017.

[3] A Scott, "Analysis of a hybrid composite pressure vessel using multi-scale computed tomography techniques," Ph.D. dissertation, University of Southampton, 2011.

[4] N. Gupta, "Polymer-matrix composites," *Advanced Materials and Processes*, vol. 137, no. 1, pp. 33–34, 94, 1990, ISSN: 08827958. DOI: 10.1007/s11837-018-2917-x. [Online]. Available: https://doi.org/10.1007/s11837-018-2917-x.

[5] H. Barthelemy, M. Weber, and F. Barbier, "Hydrogen storage: Recent improvements and industrial perspectives," *International Journal of Hydrogen Energy*, vol. 42, no. 11, pp. 7254–7262, 2017, ISSN: 03603199. DOI: 10.1016/j.ijhydene.2016.03.178. [Online]. Available: http://dx.doi.org/10.1016/j.ijhydene.2016.03.178.

[6] Luxfer, *Luxfer Gas Cylinders*, 2017. [Online]. Available: http://www.luxfercylinders.com/.

[7] Reportlinker, *Growth Opportunities in the Global Composite Cylinder Market 2015-2020: Trends, Forecast, and Opportunity Analysis, October 2015*, 2015. [Online]. Available: http://www.prnewswire.com/news-releases/growth-opportunities-in-the-global-composite-cylinder-market-

2015-2020-trends-forecast-and-opportunity-analysis-october-2015-300197054.html.

[8] M. Legault, *Pressure vessel tank types*, 2012. [Online]. Available: https://www.compositesworld.com/articles/pressure-vessel-tank-types.

[9] DoT, "Basic Requirements for CFRP Aluminium Lined Cylinders (DOT-CFFC)," no. June 1998, 2007.

[10] ISO, *Gas Cylinders - Refillable composite gas cylinders and tubes - Design, construction and testing - Part 2: Fully-wrapped fibre reinforced composite gas cylinder and tubes up to 450l with loadingsharing metal liners.* [Online]. Available: https://www.iso.org/standard/75816.html.

[11] T. Allen, S. Ahmed, W. Hepples, P. A. Reed, I. Sinclair, and M. Spearing, "A comparison of quasi-static indentation and low-velocity impact on composite overwrapped pressure vessels," *Journal of Composite Materials*, vol. 52, no. 29, pp. 4051–4060, 2018, ISSN: 1530793X. DOI: 10.1177/0021998318774401.

[12] Luxfer Gas Cylinders, *Luxfer LCX User Manual*, 2011.

[13] F. C. Shen, "A filament-wound structure technology overview," *Materials Chemistry & Physics*, vol. 42, no. 2, pp. 96–100, 1995, ISSN: 02540584. DOI: 10.1016/0254-0584(95)01554-X.

[14] Catalina Composites, *Type III cylinders manufacturing*, 2019. [Online]. Available: https://www.catalinacomposites.com/.

[15] R. J. Paul, "The Development of Lightweight Composite Cylinders for use in Demanding Structural Applications," 2011.

[16] Poliya, *Filament Winding*, 2020. [Online]. Available: https://www.poliya.com/en/filament-winding.

[17] J. Hu and K. Chandrashekhara, "Fracture analysis of hydrogen storage composite cylinders with liner crack accounting for autofrettage effect," *International Journal of Hydrogen Energy*, vol. 34, no. 8, pp. 3425–3435, 2009, ISSN: 03603199. DOI: 10.1016/j.ijhydene.2009.01.094. [Online]. Available: http://dx.doi.org/10.1016/j.ijhydene.2009.01.094.

[18] P. B. McLaughlan, S. C. Forth, and L. R. Grimes-Ledesma, "NASA/SP-2011-573 Composite overwrapped pressure vessels, a primer," no. March, 2011.

[19] A. Hocine, D. Chapelle, M. L. Boubakar, A. Benamar, and A. Bezazi, "Experimental and analytical investigation of the cylindrical part of a metallic vessel reinforced by filament winding while submitted to internal pressure," *International Journal of Pressure Vessels and Piping*, vol. 86, no. 10, pp. 649–655, 2009, ISSN: 03080161. DOI: 10.1016/j.ijpvp.2009.06.002. [Online]. Available: http://dx.doi.org/10.1016/j.ijpvp.2009.06.002.

[20] R. Shufen and U. S. Dixit, "An analysis of thermal autofrettage process with heat treatment," *International Journal of Mechanical Sciences*, vol. 144, no. May, pp. 134–145, 2018, ISSN: 00207403. DOI: 10.1016/j.ijmecsci.2018.05.053. [Online]. Available: https://doi.org/10.1016/j.ijmecsci.2018.05.053.

[21] C. P. Fowler, A. C. Orifici, and C. H. Wang, "A review of toroidal composite pressure vessel optimisation and damage tolerant design for high pressure gaseous fuel storage," *International Journal of Hydrogen Energy*, vol. 41, no. 47, pp. 22 067–22 089, 2016, ISSN: 03603199. DOI: 10.1016/j.ijhydene.2016.10.039. [Online]. Available: http://dx.doi.org/10.1016/j.ijhydene.2016.10.039.

[22] International Organization for Standardization, *ISO*. [Online]. Available: https://www.iso.org/home.html.

[23] American National Standards Institute (ANSI), *No Title*. [Online]. Available: https://webstore.ansi.org/standards/csa/csaansingv2019.

[24] W. J. Cantwell and J Morton, "The significance of damage and defects and their detection in composite materials: a review," *Journal of stress analysis*, vol. 27, no. 1, pp. 29–42, 1992. DOI: 10.1243/03093247V271029.

[25] J. M. Berthelot and J. F. Le Corre, "Modelling the transverse cracking in cross-ply laminates: Application to fatigue," *Composites Part B: Engineering*, vol. 30, no. 6, pp. 569–577, 1999, ISSN: 13598368. DOI: 10.1016/S1359-8368(99)00023-2.

[26] M. Naebe, M. M. Abolhasani, H. Khayyam, A. Amini, and B. Fox, "Crack damage in polymers and composites: A review," *Polymer Reviews*, vol. 56, no. 1, pp. 31–69, 2016, ISSN: 15583716. DOI: 10.1080/15583724.2015.1078352.

[27] M De Moura, "Interaction of matrix cracking and delamination," in *Delamination Behaviour of Composites*, 2008. DOI: 10.1201/9781439832677.ch11.

[28] S. L. Ogin, P. Brøndsted, and J. Zangenberg, *Composite materials: Constituents, architecture, and generic damage*. Elsevier, 2016, pp. 3–23, ISBN: 9781782422860. DOI: 10.1016/B978-1-78242-286-0.00001-7. [Online]. Available: http://dx.doi.org/10.1016/B978-1-78242-286-0.00001-7.

[29] V. V. Bolotin, "Delaminations in composite structures: Its origin, buckling, growth and stability," *Composites Part B: Engineering*, vol. 27, no. 2 PART B, pp. 129–145, 1996, ISSN: 13598368. DOI: 10.1016/1359-8368(95)00035-6.

[30] K. Senthil, A. Arockiarajan, R. Palaninathan, B. Santhosh, and K. M. Usha, "Defects in composite structures: Its effects and prediction methods - A comprehensive review," *Composite Structures*, vol. 106, pp. 139–149, 2013, ISSN: 02638223. DOI: 10.1016/j.compstruct.2013.06.008. [Online]. Available: http://dx.doi.org/10.1016/j.compstruct.2013.06.008.

[31] S. Nur Azrie Bt Safri, M. T. Sultan, and M. Jawaid, "Damage analysis of glass fiber reinforced composites," in *Durability and Life Prediction in Biocomposites, Fibre-Reinforced Composites and Hybrid Composites*, 2018, pp. 133–147, ISBN: 9780081022900. DOI: 10.1016/B978-0-08-102290-0.00007-6.

[32] A. C. Garg, "Delamination-a damage mode in composite structures," *Engineering Fracture Mechanics*, vol. 29, no. 5, pp. 557–584, 1988, ISSN: 00137944. DOI: 10.1016/0013-7944(88)90181-6.

[33] A. International, "D5528-01 Standard Test Method for Mode I Interlaminar Fracture Toughness of Unidirectional Fiber-Reinforced Polymer Matrix Composites," *American Society for Testing and Materials*, vol. 01, no. Reapproved, pp. 1–12, 2007.

[34] T. Tay, "Characterization and analysis of delamination fracture in composites: An overview of developments from 1990 to 2001," *Applied Mechanics Reviews*, vol. 56, no. 1, p. 1, 2003, ISSN: 00036900. DOI: 10.1115/1.1504848.

[35] A. Tabiei and W. Zhang, "Composite Laminate Delamination Simulation and Experiment: A Review of Recent Development," *Applied Mechanics Reviews*, vol. 70, no. 3, p. 030 801, 2018, ISSN: 0003-6900. DOI: 10.1115/1.4040448.

[36] S. M. Bishop, "The significance of defects on the failure of fibre composites," Royal Aircraft Establishment, Materials Department, Tech. Rep., 1981.

[37] M. Richardson and M. Wisheart, "Review of low-velocity impact properties of composite materials," *Composites Part A: Applied Science and Manufacturing*, vol. 27, no. 12, pp. 1123–1131, 1996, ISSN: 1359835X. DOI: 10.1016/1359-835X(96)00074-7. [Online]. Available: http://linkinghub.elsevier.com/retrieve/pii/1359835X96000747.

[38] P. Kumar and B. Rai, "Delaminations of barely visible impact damage in CFRP laminates," *Composite Structures*, vol. 23, no. 4, pp. 313–318, 1993, ISSN: 02638223. DOI: 10.1016/0263-8223(93)90231-E.

[39] C. Bouvet and S. Rivallant, *Damage tolerance of composite structures under low-velocity impact*. Elsevier, 2016, pp. 7–33, ISBN: 9780081008706. DOI: 10.1016/b978-0-08-100080-9.00002-6. [Online]. Available: http://dx.doi.org/10.1016/B978-0-08-100080-9.00002-6.

[40] Y. Shi, T. Swait, and C. Soutis, "Modelling damage evolution in composite laminates subjected to low velocity impact," *Composite Structures*, vol. 94, no. 9, pp. 2902–2913, 2012, ISSN: 02638223. DOI: 10.1016/j.compstruct.2012.03.039. [Online]. Available: http://dx.doi.org/10.1016/j.compstruct.2012.03.039.

[41] W. J. Cantwell and J. Morton, "Geometrical effects in the low velocity impact response of CFRP," *Composite Structures*, vol. 12, no. 1, pp. 39–59, 1989, ISSN: 02638223. DOI: 10.1016/0263-8223(89)90043-3.

[42] C. Breen, F. Guild, and M. Pavier, "Impact of thick CFRP laminates: The effect of impact velocity," *Composites Part A: Applied Science and Manufacturing*, vol. 36, no. 2 SPEC. ISS. Pp. 205–211, 2005, ISSN: 1359835X. DOI: 10.1016/j.compositesa.2004.06.005.

[43] W. J. Cantwell and J. Morton, "The impact resistance of composite materials - a review," *Composites*, vol. 22, no. 5, pp. 347–362, 1991, ISSN: 00104361. DOI: 10.1016/0010-4361(91)90549-V.

[44] D. Liu, "Impact-Induced Delamination - A View of Bending Stiffness Mismatching," vol. 22, no. July, pp. 674–692, 1988.

[45] P. Robinson and G. A. O. Davies, "Impactor mass and specimen geometry effects in low velocity impact of laminated composites," *International Journal of Impact Engineering*, vol. 12, no. 2, pp. 189–207, 1992, ISSN: 0734743X. DOI: 10.1016/0734-743X(92)90408-L.

[46] T. Yuanjian and D. H. Isaac, "Combined impact and fatigue of glass fiber reinforced composites," *Composites Part B: Engineering*, vol. 39, no. 3, pp. 505–512, 2008, ISSN: 13598368. DOI: 10.1016/j.compositesb.2007.03.005.

[47] G. P. Horn, T. J. Mackin, P. Kurath, and I Introduction, "Impact-Damaged Composites Using," vol. 22, no. 3, 2001.

[48] S. Abrate, "Impact on Laminated Composites: Recent Advances," *Applied Mechanics Reviews*, vol. 47, no. 11, p. 517, 2009, ISSN: 00036900. DOI: 10.1115/1.3111065.

[49] N. H. Tai, M. C. Yip, and J. L. Lin, "Effects of low-energy impact on the fatigue behavior of carbon/epoxy composites," *Composites Science and Technology*, vol. 58, no. 1, pp. 1–8, 1998, ISSN: 02663538. DOI: 10.1016/S0266-3538(97)00075-4.

[50] G. B. Chai and P. Manikandan, "Low velocity impact response of fibre-metal laminates - A review," *Composite Structures*, vol. 107, pp. 363–381, 2014, ISSN: 02638223. DOI: 10.1016/j.compstruct.2013.08.003. [Online]. Available: http://dx.doi.org/10.1016/j.compstruct.2013.08.003.

[51] G. Dhaliwal and G. Newaz, "Modeling Low Velocity Impact Response of Carbon Fiber Reinforced Aluminum Laminates (CARALL)," *Journal of Dynamic Behavior of Materials*, vol. 2, no. 2, pp. 181–193, 2016, ISSN: 2199-7454. DOI: 10.1007/s40870-016-0057-3. [Online]. Available: http://link.springer.com/article/10.1007/s40870-016-0057-3.

[52] F. D. Morinière, R. C. Alderliesten, M. Sadighi, and R. Benedictus, "An integrated study on the low-velocity impact response of the GLARE fibre-metal laminate," *Composite Structures*, vol. 100, pp. 89–103, 2013, ISSN: 02638223. DOI: 10.1016/j.compstruct.2012.12.016.

[53] A Vlot, "Pergamon IMPACT LOADING ON FIBRE METAL LAMINATES simplified Von K ˜ rmfin equations and also found in the work of Shivakumar et al . [5]," *Glass*, vol. 18, no. 3, pp. 291–307, 1996.

[54] J. F. Laliberté, P. V. Straznicky, C. Poon, and A. Fahr, "Applications of Fiber-Metal Laminates," *Polymer Compositess*, vol. 21, no. 4, pp. 558–567, 2000. DOI: 10.1002/pc.10211. [Online]. Available: source:http://onlinelibrary.wiley.com/doi/10.1002/pc.10211/full/{\#}.WWw4CZaE-aA.mendeley{\%}0A{\%}0A.

[55] G. H. Payeganeh, F. Ashenai Ghasemi, and K. Malekzadeh, "Dynamic response of fiber-metal laminates (FMLs) subjected to low-velocity impact," *Thin-Walled Structures*, vol. 48, no. 1, pp. 62–70, 2010, ISSN: 02638231. DOI: 10.1016/j.tws.2009.07.005. [Online]. Available: http://dx.doi.org/10.1016/j.tws.2009.07.005.

[56] G. D. Lawcock, L Ye, Y. W. Mai, and C. T. Sun, "Effects of fibre/matrix adhesion on carbon-fibre reinforced metal laminates - II Impact behaviour," vol. 3538, no. 97, 2006.

[57] J. C. Ríos, E. Chomik, J. J. Balderrama, F. Cambiasso, and E. Asta, "Determination of Fracture Toughness J on Fiber-metal Laminate Type CARALL with Sheets of Aluminium 6061," *Procedia Materials Science*, vol. 9, pp. 530–537, 2015, ISSN: 22118128. DOI: 10.1016/j.mspro.2015.05.026. [Online]. Available: http://dx.doi.org/10.1016/j.mspro.2015.05.026.

[58] P. Soltani, M. Keikhosravy, R. H. Oskouei, and C. Soutis, "Studying the tensile behaviour of GLARE laminates: A finite element modelling approach," *Applied Composite Materials*, vol. 18, no. 4, pp. 271–282, 2011, ISSN: 0929189X. DOI: 10.1007/s10443-010-9155-x.

[59] J. Bieniaś, K. Dadej, and B. Surowska, "Interlaminar fracture toughness of glass and carbon reinforced multidirectional fiber metal laminates," *Engineering Fracture Mechanics*, vol. 175, pp. 127–145, 2017, ISSN: 00137944. DOI: 10.1016/j.engfracmech.2017.02.007.

[60] M. R. Abdullah, Y. Prawoto, and W. J. Cantwell, "Interfacial fracture of the fibre-metal laminates based on fibre reinforced thermoplastics," *Materials and Design*, vol. 66, no. PB, pp. 446–452, 2015, ISSN: 18734197. DOI: 10.1016/j.matdes.2014.03.058. [Online]. Available: http://dx.doi.org/10.1016/j.matdes.2014.03.058.

[61] P. Mertiny, F. Ellyin, and A. Hothan, "An experimental investigation on the effect of multi-angle filament winding on the strength of tubular composite structures," *Composites Science and Technology*, vol. 64, no. 1, pp. 1–9, 2004, ISSN: 02663538. DOI: 10.1016/S0266-3538(03)00198-2.

[62] H. Hernández-Moreno, B. Douchin, F. Collombet, D. Choqueuse, and P. Davies, "Influence of winding pattern on the mechanical behavior of filament wound composite cylinders under external pressure," *Composites Science and Technology*, vol. 68, no. 3-4, pp. 1015–1024, 2008, ISSN: 02663538. DOI: 10.1016/j.compscitech.2007.07.020.

[63] C. P. Fowler, A. C. Orifici, and C. H. Wang, "A review of toroidal composite pressure vessel optimisation and damage tolerant design for high pressure gaseous fuel storage," *International Journal of Hydrogen Energy*, vol. 41, no. 47, pp. 22 067–22 089, 2016, ISSN: 03603199. DOI: 10.1016/j.

ijhydene.2016.10.039. [Online]. Available: http://dx.doi.org/10.1016/j.ijhydene.2016.10.039.

[64] R. Wang, W. Jiao, W. Liu, F. Yang, and X. He, "Slippage coefficient measurement for non-geodesic filament-winding process," *Composites Part A: Applied Science and Manufacturing*, vol. 42, no. 3, pp. 303–309, 2011, ISSN: 1359835X. DOI: 10.1016/j.compositesa.2010.12.002. [Online]. Available: http://dx.doi.org/10.1016/j.compositesa.2010.12.002.

[65] J. De Carvalho, M. Lossie, D. Vandepitte, and H. Van Brussel, "Optimization of filament-wound parts based on non-geodesic winding," *Composites Manufacturing*, vol. 6, no. 2, pp. 79–84, 1995, ISSN: 09567143. DOI: 10.1016/0956-7143(95)99647-B.

[66] L. Zu, S. Koussios, and A. Beukers, "Design of filament-wound circular toroidal hydrogen storage vessels based on non-geodesic fiber trajectories," *International Journal of Hydrogen Energy*, vol. 35, no. 2, pp. 660–670, 2010, ISSN: 03603199. DOI: 10.1016/j.ijhydene.2009.10.062. [Online]. Available: http://dx.doi.org/10.1016/j.ijhydene.2009.10.062.

[67] ——, "Flame-Retardancy Properties of Intumescent Ammonium Poly(Phosphate) and Mineral Filler Magnesium Hydroxide in Combination with Graphene," *Polymers and Polymer Composites*, vol. 16, no. 2, pp. 101–113, 2012, ISSN: 09673911. DOI: 10.1002/pc. arXiv: 1206.4529.

[68] F. Ellyin and M. Martens, "Biaxial fatigue behaviour of a multidirectional filament-wound glass-fiber/epoxy pipe," *Composites Science and Technology*, vol. 61, no. 4, pp. 491–502, 2001, ISSN: 02663538. DOI: 10.1016/S0266-3538(00)00215-3.

[69] J. Rousseau, D. Perreux, and N. Verdière, "The influence of winding patterns on the damage behaviour of filament-wound pipes," *Nuclear Instruments and Methods in Physics Research, Section B: Beam Interactions with Materials and Atoms*, vol. 175-177, pp. 169–175, 2001, ISSN: 0168583X. DOI: 10.1016/S0168-583X(00)00540-1.

[70] A. E. Pavan and K. S. Ahmed, "Effect of Constituent Shell," *International Journal of Scientific & Engineering Research*, vol. 9, no. 5, pp. 112–118, 2018.

[71] S. Wakayama, S. Kobayashi, T. Imai, and T. Matsumoto, "Evaluation of burst strength of FW-FRP composite pipes after impact using pitch-based low-modulus carbon fiber," *Composites Part A: Applied Science and Manufacturing*, vol. 37, no. 11, pp. 2002–2010, 2006, ISSN: 1359835X. DOI: 10.1016/j.compositesa.2005.12.010.

[72] S. Kobayashi and M. Kawahara, "Effects of stacking thickness on the damage behavior in CFRP composite cylinders subjected to out-of-plane loading," *Composites Part A: Applied Science and Manufacturing*, vol. 43, no. 1, pp. 231–237, 2012, ISSN: 1359835X. DOI: 10.1016/j.compositesa.2011.10.004. [Online]. Available: http://dx.doi.org/10.1016/j.compositesa.2011.10.004.

[73] P Blanc-Vannet, O Bardoux, N Alexandre, F Nony, M. Barcikowski, R. Rybczyński, A. Maldachowska, P Breuer, K Lasn, A Echtermeyer, F Dahmene, and S Bittendiebel, "Residual performance of composite pressure vessels submitted to mechanical impacts," *Proceedings of 7th International Conference Hydrogen Safety (ICHS 2017)*, no. September, pp. 488–495, 2017.

[74] M. Weber, C. Devilliersa, N. Guillaud, F. Dau, B. Gentilleauc, F. Nony, S. Villalonga, and D. Halm, "Damage tolerance of compressed gaseous hydrogen composites vessels," *16th European Conference on Composite Materials, ECCM 2014*, no. June, pp. 22–26, 2014.

[75] Y.-S. Kim, L.-H. Kim, and J.-S. Park, "The effect of composite damage on fatigue life of the high pressure vessel for natural gas vehicles," *Composite Structures*, vol. 93, no. 11, pp. 2963–2968, 2011, ISSN: 02638223. DOI: 10.1016/j.compstruct.2011.05.007. [Online]. Available: http://dx.doi.org/10.1016/j.compstruct.2011.05.007.

[76] S. K. Ha and J. Y. Jeong, "Effects of winding angles on through-thickness properties and residual strains of thick filament wound composite rings," *Composites Science and Technology*, vol. 65, no. 1, pp. 27–35, 2005, ISSN: 02663538. DOI: 10.1016/j.compscitech.2004.05.019.

[77] F. Eggers, J. H. S. Almeida, C. B. Azevedo, and S. C. Amico, "Mechanical response of filament wound composite rings under tension and compression," *Polymer Testing*, vol. 78, no. January, p. 105 951, 2019, ISSN:

01429418. DOI: 10.1016/j.polymertesting.2019.105951. [Online]. Available: https://doi.org/10.1016/j.polymertesting.2019.105951.

[78] R. A. Weerts, O. Cousigné, K. Kunze, M. G. Geers, and J. J. Remmers, "Assessment of contact-induced damage mechanisms in thick-walled composite cylinders," *Journal of Reinforced Plastics and Composites*, vol. 39, no. 17-18, pp. 679–699, 2020, ISSN: 15307964. DOI: 10.1177/0731684420923043.

[79] K. L. Alderson and K. E. Evans, "Low velocity transverse impact of filament-wound pipes: Part 1. Damage due to static and impact loads," *Composite Structures*, vol. 20, no. 1, pp. 37–45, 1992, ISSN: 02638223. DOI: 10.1016/0263-8223(92)90010-A.

[80] J. Curtis, M. J. Hinton, S. Li, S. R. Reid, and P. D. Soden, "Damage, deformation and residual burst strength of filament-wound composite tubes subjected to impact or quasi-static indentation," *Composites Part B: Engineering*, vol. 31, no. 5, pp. 419–433, 2000, ISSN: 13598368. DOI: 10.1016/S1359-8368(00)00014-7.

[81] D. C. Pham, N. Sridhar, X. Qian, A. J. Sobey, M. Achintha, and A. Shenoi, "A review on design, manufacture and mechanics of composite risers," *Ocean Engineering*, vol. 112, pp. 82–96, 2016, ISSN: 00298018. DOI: 10.1016/j.oceaneng.2015.12.004. [Online]. Available: http://dx.doi.org/10.1016/j.oceaneng.2015.12.004.

[82] F. Ellyin and M. Carroll, "The behavior of multidirectional filament wound fibreglass/epoxy tubulars under biaxial loading," *Composites Part A: Applied Science and Manufacturing*, vol. 28, no. 9-10, pp. 781–790, 1997, ISSN: 1359835X. DOI: 10.1016/S1359-835X(97)00021-3.

[83] B. Mustafa, S. Li, P. D. Soden, S. R. Reid, C. M. Leech, and M. J. Hinton, "Lateral indentation of filament wound GRP tubes," *International Journal of Mechanical Sciences*, vol. 34, no. 6, pp. 443–457, 1992, ISSN: 00207403. DOI: 10.1016/0020-7403(92)90011-5.

[84] Z. Changliang, R. Mingfa, Z. Wei, and C. Haoran, "Delamination prediction of composite filament wound vessel with metal liner under low velocity impact," *Composite Structures*, vol. 75, no. 1-4, pp. 387–392, 2006, ISSN: 02638223. DOI: 10.1016/j.compstruct.2006.04.012.

[85] S. Sulaiman, S. Borazjani, and S. H. Tang, "Finite element analysis of filament-wound composite pressure vessel under internal pressure," *IOP Conference Series: Materials Science and Engineering*, vol. 50, no. 1, 2013, ISSN: 17578981. DOI: 10.1088/1757-899X/50/1/012061.

[86] G. Perillo, F. Grytten, S. Sørbø, and V. Delhaye, "Numerical/experimental impact events on filament wound composite pressure vessel," *Composites Part B: Engineering*, vol. 69, pp. 406–417, 2015, ISSN: 13598368. DOI: 10.1016/j.compositesb.2014.10.030. [Online]. Available: http://dx.doi.org/10.1016/j.compositesb.2014.10.030.

[87] J. Zheng, Y. Hu, L. Ma, and Y. Du, "Delamination failure of composite containment vessels subjected to internal blast loading," *Composite Structures*, vol. 130, pp. 29–36, 2015, ISSN: 02638223. DOI: 10.1016/j.compstruct.2015.04.013.

[88] D. S. Son and S. H. Chang, "Evaluation of modeling techniques for a type III hydrogen pressure vessel (70 MPa) made of an aluminum liner and a thick carbon/epoxy composite for fuel cell vehicles," *International Journal of Hydrogen Energy*, vol. 37, no. 3, pp. 2353–2369, 2012, ISSN: 03603199. DOI: 10.1016/j.ijhydene.2011.11.001.

[89] M.-G. Han and S.-H. Chang, "Failure analysis of a Type III hydrogen pressure vessel under impact loading induced by free fall," *Composite Structures*, vol. 127, pp. 288–297, 2015, ISSN: 02638223. DOI: 10.1016/j.compstruct.2015.03.027. [Online]. Available: http://linkinghub.elsevier.com/retrieve/pii/S0263822315001993.

[90] ——, "Evaluation of structural integrity of Type-III hydrogen pressure vessel under low-velocity car-to-car collision using finite element analysis," *Composite Structures*, vol. 148, pp. 198–206, 2016, ISSN: 02638223. DOI: 10.1016/j.compstruct.2016.03.060. [Online]. Available: http://dx.doi.org/10.1016/j.compstruct.2016.03.060.

[91] S. Kobayashi, T. Imai, and S. Wakayama, "Burst strength evaluation of the FW-CFRP hybrid composite pipes considering plastic deformation of the liner," *Composites Part A: Applied Science and Manufacturing*, vol. 38, no. 5, pp. 1344–1353, 2007, ISSN: 1359835X. DOI: 10.1016/j.compositesa.2006.10.011.

[92] A. Girão-coelho, "Finite Element Guidelines for Simulation of Delamination Dominated Failures in Composite Materials Validated by Case Studies," no. February, pp. 1–26, 2016.

[93] G Alfano and M. A. Crisfield, "Finite element interface models for the delamination analysis of laminated composites : Mechanical and computational issues," *International Journal for Numerical Methods in Engineering*, no. 50, pp. 1701–1736, 2001. DOI: 10.1002/nme.93.

[94] R. Krueger, "Virtual crack closure technique: History, approach, and applications," *Applied Mechanics Reviews*, vol. 57, no. 2, p. 109, 2004, ISSN: 00036900. DOI: 10.1115/1.1595677.

[95] R. Krueger, K. N. Shivakumar, and I. S. Raju, "Fracture Mechanics Analyses for Interface Crack Problems - A Review," no. September 2015, 2013. DOI: 10.2514/6.2013-1476.

[96] A. Pirondi, G. Giuliese, F. Moroni, A. Bernasconi, and A. Jamil, "Comparative study of cohesive zone and virtual crack closure techniques for three-dimensional fatigue debonding," *Journal of Adhesion*, vol. 90, no. 5-6, pp. 457–481, 2014, ISSN: 15455823. DOI: 10.1080/00218464.2013.859616.

[97] M. F. Pernice, N. V. De Carvalho, and S. R. Hallett, "University of Bristol - Explore Bristol Research," *ACS Sustainable Chem. Eng.*, vol. 4, no. September 2016, pp. 6200–6207, 2016. DOI: 10.1021/acssuschemeng.6b02020.

[98] D. Dudgale, "Yielding of steel sheets containing slits," *Journal of the Mechanics and Physics of Solids*, vol. 8, no. 2, pp. 100–104, 1960, ISSN: 00225096. DOI: 10.1016/0022-5096(60)90013-2. arXiv: 0021-8928(59)90157-1 [10.1016]. [Online]. Available: http://linkinghub.elsevier.com/retrieve/pii/0022509660900132.

[99] A. Hillerborg, M. Modéer, and P. E. Petersson, "Analysis of crack formation and crack growth in concrete by means of fracture mechanics and finite elements," *Cement and Concrete Research*, vol. 6, no. 6, pp. 773–781, 1976, ISSN: 00088846. DOI: 10.1016/0008-8846(76)90007-7.

[100] M. A. Crisfield, Y. Mi, and G. A. O. Davies, *Progressive Delamination using Interface Elements*.

[101] Y. Wei and J. W. Hutchinson, "Interface strength, work of adhesion and plasticity in the peel test," *International Journal of Fracture*, vol. 93, no. 1-4, pp. 315–333, 1998, ISSN: 03769429. DOI: 10.1007/978-94-017-2854-6_16.

[102] A. Turon, P. P. Camanho, J. Costa, and C. G. Dávila, "A damage model for the simulation of delamination in advanced composites under variable-mode loading," *Mechanics of Materials*, vol. 38, no. 11, pp. 1072–1089, 2006, ISSN: 01676636. DOI: 10.1016/j.mechmat.2005.10.003.

[103] S. R. Hallett and P. W. Harper, "Modelling delamination with cohesive interface elements," *Numerical Modelling of Failure in Advanced Composite Materials*, pp. 55–72, 2015. DOI: 10.1016/B978-0-08-100332-9.00002-5.

[104] P. W. Harper and S. R. Hallett, "Cohesive zone length in numerical simulations of composite delamination," *Engineering Fracture Mechanics*, vol. 75, no. 16, pp. 4774–4792, 2008, ISSN: 00137944. DOI: 10.1016/j.engfracmech.2008.06.004.

[105] C. G. Dávila, P. P. Camanho, and A. Turon, "Effective Simulation of Delamination in Aeronautical Structures Using Shells and Cohesive Elements," *Journal of Aircraft*, vol. 45, no. 2, pp. 663–672, 2008, ISSN: 0021-8669. DOI: 10.2514/1.32832. [Online]. Available: http://arc.aiaa.org/doi/10.2514/1.32832.

[106] A. Turon, C. G. Dávila, P. P. Camanho, and J. Costa, "An engineering solution for mesh size effects in the simulation of delamination using cohesive zone models," *Engineering Fracture Mechanics*, vol. 74, no. 10, pp. 1665–1682, 2007, ISSN: 00137944. DOI: 10.1016/j.engfracmech.2006.08.025.

[107] P. P. Camanho, C. G. Dávila, and M. F. de Moura, "Mixed-Mode Decohesion Finite Elements in for the Simulation Composite of Delamination Materials," *Journal of Composite Materials*, vol. 37, no. 16, pp. 1415–1438, 2003, ISSN: 00219983. DOI: 10.1177/0021998303034505.

[108] P. W. Harper, L. Sun, and S. R. Hallett, "A study on the influence of cohesive zone interface element strength parameters on mixed mode behaviour," *Composites Part A: Applied Science and Manufacturing*, vol. 43, no. 4, pp. 722–734, 2012, ISSN: 1359835X. DOI: 10.1016/j.compositesa.2011.12.016. [Online]. Available: http://dx.doi.org/10.1016/j.compositesa.2011.12.016.

[109] D. S. Son, J. H. Hong, and S. H. Chang, "Determination of the autofrettage pressure and estimation of material failures of a Type III hydrogen pressure vessel by using finite element analysis," *International Journal of Hydrogen Energy*, vol. 37, no. 17, pp. 12 771–12 781, 2012, ISSN: 03603199. DOI: 10.1016/j.ijhydene.2012.06.044. [Online]. Available: http://dx.doi.org/10.1016/j.ijhydene.2012.06.044.

[110] E. V. González, P. Maimí, A. Turon, P. P. Camanho, and J. Renart, "Simulation of delamination by means of cohesive elements using an explicit finite element code," *Computers, Materials and Continua*, vol. 9, no. 1, pp. 51–92, 2009, ISSN: 15462218. DOI: 10.3970/CMC.2009.009.051.

[111] E. Jones and M. Idacola, "A Good Practices Guide for Digital Image Correlation," 2018. DOI: 10.32720/idics/gpg.ed1. [Online]. Available: http://idics.org/guide/.

[112] P. Reu, "Introduction to digital image correlation: Best practices and applications. In "The Art and Application of DIC" article series.," *Experimental Techniques*, vol. 36, no. 1, pp. 3–4, 2012, ISSN: 07328818. DOI: 10.1111/j.1747-1567.2011.00798.x.

[113] LaVision, *Digital Image Correlation (DIC)*. [Online]. Available: https://www.lavision.de/en/techniques/dic-dvc/.

[114] Z. Zou, S. R. Reid, S. Li, and P. D. Soden, "Application of a delamination model to laminated composite structures," *Composite Structures*, vol. 56, no. 4, pp. 375–389, 2002, ISSN: 02638223. DOI: 10.1016/S0263-8223(02)00021-1.

[115] A. Turon, C. G. Dávila, P. P. Camanho, and J. Costa, "An Engineering Solution for using Coarse Meshes in the Simulation of Delamination With Cohesive Zone Models," *Nasa/Tm-2005-213547*, no. March, pp. 1–26, 2005.

[116] M. Soroush, K. Malekzadeh Fard, and M. Shahravi, "Finite element simulation of interlaminar and intralaminar damage in laminated composite plates subjected to impact," *Latin American Journal of Solids and Structures*, vol. 15, no. 6, 2018, ISSN: 16797825. DOI: 10.1590/1679-78254609.

[117] Dassault Systemes, "32.5.6 Defining the constitutive response of cohesive elements using a traction-separation description," Tech. Rep. mode mix, 2014, pp. 1–22.

[118] A. Turon, P. P. Camanho, J. Costa, and J. Renart, "Accurate simulation of delamination growth under mixed-mode loading using cohesive elements: Definition of interlaminar strengths and elastic stiffness," *Composite Structures*, vol. 92, no. 8, pp. 1857–1864, 2010, ISSN: 02638223. DOI: 10.1016/j.compstruct.2010.01.012. [Online]. Available: http://dx.doi.org/10.1016/j.compstruct.2010.01.012.

[119] G. Barenblatt, "The mathematical theory of equilibrium cracks formed in brittle fracture," *Advances in applied mechanics*, 1962.

[120] C. Y. Hui, A. Jagota, S. J. Bennison, and J. D. Londono, "Crack blunting and the strength of soft elastic solids," *Proceedings of the Royal Society A: Mathematical, Physical and Engineering Sciences*, vol. 459, no. 2034, pp. 1489–1516, 2003, ISSN: 14712946. DOI: 10.1098/rspa.2002.1057.

[121] M. L. Falk and J. R. Rice, "A critical evaluation of cohesive zone models of dynamic fracture," vol. 120, pp. 61–68, 2004. DOI: 10.1051/jp4.

[122] G. Perillo, R. Vacher, F. Grytten, S. Sørbø, and V. Delhaye, "Material characterisation and failure envelope evaluation of filament wound GFRP and CFRP composite tubes," *Polymer Testing*, vol. 40, pp. 54–62, 2014, ISSN: 01429418. DOI: 10.1016/j.polymertesting.2014.08.009. [Online]. Available: http://dx.doi.org/10.1016/j.polymertesting.2014.08.009.

[123] "11.6.1 Mass scaling Products: Abaqus/Explicit Abaqus/CAE," pp. 1–11, 2018.

[124] S. T. Pinho, L. Iannucci, and P. Robinson, "Formulation and implementation of decohesion elements in an explicit finite element code," *Composites Part A: Applied Science and Manufacturing*, vol. 37, no. 5, pp. 778–789, 2006, ISSN: 1359835X. DOI: 10.1016/j.compositesa.2005.06.007.

[125] V. Mollón, J. Bonhomme, A. M. Elmarakbi, A. Argüelles, and J. Viña, "Finite element modelling of mode i delamination specimens by means of implicit and explicit solvers," *Polymer Testing*, vol. 31, no. 3, pp. 404–410, 2012, ISSN: 01429418. DOI: 10.1016/j.polymertesting.2011.12.008. [Online]. Available: http://dx.doi.org/10.1016/j.polymertesting.2011.12.008.

[126] K. Song, C. Dávila, and C. Rose, "Guidelines and parameter selection for the simulation of progressive delamination," *2008 ABAQUS User's Conference*, pp. 1–15, 2008. [Online]. Available: http://www.simulia.com/forms/world/pdf2008/SONG-AUC2008.pdf.

[127] P. Camanho and C. Davila, "Mixed-Mode Decohesion Finite Elements in for the Simulation Composite of Delamination Materials," *Nasa*, vol. TM-2002-21, no. June, pp. 1–37, 2002, ISSN: 00219983. DOI: 10.1177/002199803034505.

[128] V. Alfred Franklin and T. Christopher, "Fracture energy estimation of DCB specimens made of glass/epoxy: An experimental study," *Advances in Materials Science and Engineering*, vol. 2013, 2013, ISSN: 16878434. DOI: 10.1155/2013/412601.

[129] M. F. S. F. de Moura, R. D. S. G. Campilho, and J. P. M. Gonçalves, "Pure mode II fracture characterization of composite bonded joints," *International Journal of Solids and Structures*, vol. 46, no. 6, pp. 1589–1595, 2009, ISSN: 00207683. DOI: 10.1016/j.ijsolstr.2008.12.001. [Online]. Available: http://dx.doi.org/10.1016/j.ijsolstr.2008.12.001.

[130] M. M. Shokrieh, M. Heidari-Rarani, and S. Rahimi, "Influence of curved delamination front on toughness of multidirectional DCB specimens," *Composite Structures*, vol. 94, no. 4, pp. 1359–1365, 2012, ISSN: 02638223. DOI: 10.1016/j.compstruct.2011.11.035. [Online]. Available: http://dx.doi.org/10.1016/j.compstruct.2011.11.035.

[131] R. Bigger, B. Blaysat, C. Boo, M. Grewer, J. Hu, A. Jones, M. Klein, K. Raghavan, P. Reu, T. Schmidt, T. Siebert, M. Simenson, D. Turner, A. Vieira, and T. Weikert, "A Good Practices Guide for Digital Image Correlation," *International Digital Image Correlation Society*, p. 94, 2018. DOI: 10.32720/idics/gpg.ed1. [Online]. Available: http://idics.org/guide/.

[132] D. Liu, E. Lansing, and L. E. Malvern, "Cracking in Impacted Glass / Epoxy Plates," *Journal of Composite Materials*, vol. 21, no. July 1987, pp. 594–609, 1987.

[133] M Nurhaniza, M. K. A. Ariffin, A. Ali, F Mustapha, and A. W. Noraini, "Finite element analysis of composites materials for aerospace applications," *IOP Conference Series: Materials Science and Engineering*, vol. 11, p. 012 010, 2010. DOI: 10.1088/1757-899x/11/1/012010.

[134] T. Abbey, "Structural FEA in the Automotive Industry," *Design Engineering 247*, 2014. [Online]. Available: https://www.digitalengineering247.com/article/structural-fea-in-the-automotive-industry/.

[135] S. Gu, "Application of finite element method in mechanical design of automotive parts," *IOP Conference Series: Materials Science and Engineering*, vol. 231, no. 1, 2017, ISSN: 1757899X. DOI: 10.1088/1757-899X/231/1/012180.

[136] L. Wang, C. Zheng, H. Luo, S. Wei, and Z. Wei, "Continuum damage modeling and progressive failure analysis of carbon fiber/epoxy composite pressure vessel," *Composite Structures*, vol. 134, pp. 475–482, 2015, ISSN: 02638223. DOI: 10.1016/j.compstruct.2015.08.107. [Online]. Available: http://dx.doi.org/10.1016/j.compstruct.2015.08.107.

[137] W. R. Park, N. F. Fatoni, and O. H. Kwon, "Evaluation of stress and crack behavior using the extended finite element method in the composite layer of a type III hydrogen storage vessel," *Journal of Mechanical Science and Technology*, vol. 32, no. 5, pp. 1995–2002, 2018, ISSN: 1738494X. DOI: 10.1007/s12206-018-0407-2.

[138] Q. G. Wu, X. D. Chen, Z. C. Fan, and D. F. Nie, "Stress and Damage Analyses of Composite Overwrapped Pressure Vessel," *Procedia Engineering*, vol. 130, pp. 32–40, 2015, ISSN: 18777058. DOI: 10.1016/j.proeng.2015.12.171.

[139] *Matweb*. [Online]. Available: www.matweb.com.

[140] Toray Carbon Fibers America Inc., *Torayca 700s data sheet*, Santa Ana CA.

[141] ——, *Torayca T1000G data sheet*, Santa Ana CA.

[142] ——, *Torayca M60J data sheet*, Santa Ana CA.

[143] J. C. Thesken, P. L. Murthy, S. L. Phoenix, N. Greene, J. Palko, J. Eldridge, J. Sutter, R. Saulsberry, and H. Beeson, "A theoretical investigation of composite overwrapped pressure vessel (COPV) mechanics applied to NASA full scale tests," *American Society for Composites - 21st Technical Conference of the American Society for Composites 2006*, vol. 1, no. January, pp. 219–238, 2006.

[144] G. Geißler and M. Kaliske, "Time-dependent cohesive zone modelling for discrete fracture simulation," *Engineering Fracture Mechanics*, vol. 77, no. 1, pp. 153–169, 2010, ISSN: 00137944. DOI: 10.1016/j.engfracmech.2009.09.013. [Online]. Available: http://dx.doi.org/10.1016/j.engfracmech.2009.09.013.

[145] M. Musto and G. Alfano, "A novel rate-dependent cohesive-zone model combining damage and visco-elasticity," *Computers and Structures*, vol. 118, pp. 126–133, 2013, ISSN: 00457949. DOI: 10.1016/j.compstruc.2012.12.020. [Online]. Available: http://dx.doi.org/10.1016/j.compstruc.2012.12.020.

[146] S. Salih, K. Davey, and Z. Zou, "Rate-dependent elastic and elasto-plastic cohesive zone models for dynamic crack propagation," *International Journal of Solids and Structures*, vol. 90, pp. 95–115, 2016, ISSN: 00207683. DOI: 10.1016/j.ijsolstr.2016.04.002. [Online]. Available: http://dx.doi.org/10.1016/j.ijsolstr.2016.04.002.

[147] G. L. Praveena, S Eshwari, and K. K. Kumar, "Structural Analysis of Multilayer Pressure Vessels for Different Shapes of Cross Sections by Using FEM," no. December, pp. 16 543–16 551, 2017. DOI: 10.15680/IJIRSET.2017.0608249.